



DISTRIBUTION STATEMENT A
Approved for Public Release
Distribution Unlimited



**DIMSAT, DIPARTIMENTO DI
MECCANICA, STRUTTURE
AMBIENTE E TERRITORIO
FACOLTÀ DI INGEGNERIA**

*UNIVERSITÀ DI CASSINO
VIA DI BIASIO 43, 03043
CASSINO (FR), ITALY*

RESEARCH CONTRACT

STRAIN RATE AND TEMPERATURE EFFECT IN DUCTILE FAILURE PROCESS: CHARACTERIZATION AND MODELING USING CONTINUUM DAMAGE MECHANICS

FINAL REPORT

TO: E.O.A.R.D., 223/231 MARYLEBONE RD.,
LONDON NW1 5TH – ENGLAND

AUTHORS: NICOLA BONORA, PH.D.
PROF. PIETRO PAOLO MILELLA

CONTRACT N°F61775-99-WE066

JULY, 2000

REPORT DOCUMENTATION PAGE

Form Approved OMB No. 0704-0188

Public reporting burden for this collection of information is estimated to average 1 hour per response, including the time for reviewing instructions, searching existing data sources, gathering and maintaining the data needed, and completing and reviewing the collection of information. Send comments regarding this burden estimate or any other aspect of this collection of information, including suggestions for reducing this burden to Washington Headquarters Services, Directorate for Information Operations and Reports, 1215 Jefferson Davis Highway, Suite 1204, Arlington, VA 22202-4302, and to the Office of Management and Budget, Paperwork Reduction Project (0704-0188), Washington, DC 20503.

1. AGENCY USE ONLY (Leave blank)		2. REPORT DATE 28-July-2000	3. REPORT TYPE AND DATES COVERED Final Report
4. TITLE AND SUBTITLE Strain Rate And Temperature Effect In Ductile Failure Process: Characterization And Modeling Using Continuum Damage Mechanics		5. FUNDING NUMBERS F61775-99-WE066	
6. AUTHOR(S) Dr. Nicola Bonora			
7. PERFORMING ORGANIZATION NAME(S) AND ADDRESS(ES) University of Cassino Via G. Di Biasio 43 Cassino 03043 Italy		8. PERFORMING ORGANIZATION REPORT NUMBER N/A	
9. SPONSORING/MONITORING AGENCY NAME(S) AND ADDRESS(ES) EOARD PSC 802 BOX 14 FPO 09499-0200		10. SPONSORING/MONITORING AGENCY REPORT NUMBER SPC 99-4066	
11. SUPPLEMENTARY NOTES			
12a. DISTRIBUTION/AVAILABILITY STATEMENT Approved for public release; distribution is unlimited.		12b. DISTRIBUTION CODE A	
13. ABSTRACT (Maximum 200 words) This report results from a contract tasking University of Cassino as follows: The contractor shall investigate temperature and strain rate effects on ductile damage processes performed at room and elevated temperature on alloys having aerospace applications using continuum damage mechanics. The results will be used to validate their model and characterize various alloys having U.S. Air Force interests for applications in aging aircraft and corrosion.			
14. SUBJECT TERMS EOARD, Aging Aircraft, Failure Mechanisms		15. NUMBER OF PAGES 76	
		16. PRICE CODE N/A	
17. SECURITY CLASSIFICATION OF REPORT UNCLASSIFIED	18. SECURITY CLASSIFICATION OF THIS PAGE UNCLASSIFIED	19. SECURITY CLASSIFICATION OF ABSTRACT UNCLASSIFIED	20. LIMITATION OF ABSTRACT UL

NSN 7540-01-280-5500

Standard Form 298 (Rev. 2-89)
Prescribed by ANSI Std. Z39-18
298-102



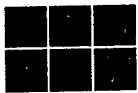
RESEARCH CONTRACT

STRAIN RATE AND TEMPERATURE
EFFECT IN DUCTILE FAILURE PROCESS:
CHARACTERIZATION AND MODELING
USING CONTINUUM DAMAGE
MECHANICS

FINAL REPORT

TO: E.O.A.R.D., 223/231 MARYLEBONE RD.,
LONDON NW1 5TH – ENGLAND

AUTHORS: NICOLA BONORA, PH.D.
PROF. PIETRO PAOLO MILELLA



DiMSAT, DIPARTIMENTO DI
MECCANICA, STRUTTURE
AMBIENTE E TERRITORIO
FACOLTÀ DI INGEGNERIA

UNIVERSITÀ DI CASSINO
VIA DI BIASIO 43, 03043
CASSINO (FR), ITALY

CONTRACT N° F61775-99-WE066

JULY, 2000

AQF-00-3743

TABLE OF CONTENTS

TABLE OF CONTENTS	1
1.0 ABSTRACT.....	2
2.0 INTRODUCTION	3
3.0 NON LINEAR CONTINUUM DAMAGE MECHANICS MODEL.....	5
3.1 BACKGROUND	5
3.2. THE DAMAGE MODEL	6
3.3 STRESS TRIAXIALITY, DAMAGE EVOLUTION AND PARAMETERS	10
3.4 QUASI-STATIC DAMAGE MEASUREMENTS	13
3.5 DYNAMIC DAMAGE MEASUREMENTS	20
3.6 TRIAXIALITY EFFECT ON MATERIAL DUCTILITY.....	27
3.7 MICROSCOPY ANALYSIS OF FRACTURE SURFACES	33
4.0 SOLID STATE EQUATION	40
4.1 BACKGROUND	40
4.2 THE EFFECT OF TEMPERATURE	41
4.3 EXPERIMENTAL RESULTS.....	46
4.4 LOW STRAIN RATE BEHAVIOR.....	48
4.5 THE MECHANICAL EQUATION OF SOLID STATE.....	52
4.6 THE DRAG-STRESS OF ATMOSPHERES ON MOVING DISLOCATIONS.....	53
4.7 EXPERIMENTAL PROGRAM.....	56
4.8 HIGH STRAIN RATE BEHAVIOR.....	64
5.0 UNIFIED MODEL.....	69
6.0 CONCLUSIONS AND RECOMMENDATION	72
REFERENCES.....	74

1.0 ABSTRACT

The research addresses the issue of ductile material behavior and fracture prediction from a local approach point of view, based on continuum damage mechanics (CDM), taking into consideration also the effect of temperature and strain rate on global material response starting from two new innovative models:

- a) a new developed constitutive damage model, based on a non-linear damage potential, independent of the material;
- b) a new developed solid state equation to describe material response to strain rate and temperature.

The final target is to couple the two models into a single equation. In this report, the two models will be described in details and verified by mean either of experimental data already available in the open literature or obtained through *ad hoc* experiments on BCC and HCP lattice metals. In this report, the entire research activity performed during the twelve months contract duration is summarized.

In accordance with Defense Federal Acquisition Regulation 252.227-7036, Declaration of Technical Data Conformity Jan 1997), the contractor, Nicola Bonora – University of Cassino, hereby declares that, to the best knowledge and belief, the technical data delivered herewith under Contract n°F61775-99-WE066 is complete, accurate and complies with all requirements of the contract.



Date: July 18th 2000

In accordance with the requirements in Federal Acquisition Regulation 52.227-13 Patent Rights- Acquisition by the U.S. Government (Jun 1999):

- a) Disclosure of all subject inventions as defined in FAR 52.227-13 have been reported in accordance with this clause
- b) I certify that there were no subject inventions to declare as defined in FAR 52.227-13, during the performance of this contract.



Date: July 18th 2000

2.0 INTRODUCTION

In recent years, the use of traditional metals and alloys in structural application has gone in the direction to assess the material capability to plastically deform in order to exploit, as much as possible, its actual potential to withstand loads beyond the elastic limit. This is particularly important in residual life assessment and life extension of warplanes, especially when exposed to combat action. Moreover, a wide plastic deformation range is expected for those structural components that have to absorb energy such as shock absorbers, containment, blast shields, and so on. In the range of large plastic deformation, the mechanism of failure is intimately connected to the material constitutive response and no reliable design criteria can be developed without incorporating the information relative to it. Situation becomes even more complicated when the deformation of solids occurs under dynamic loading, either low or high strain rate and temperature. The extreme case is that of shaped charges where the liner is deformed at a very high strain rate, that varies radially, by the propagation of the shock wave, generated by the explosive detonation.

Thus, in order to predict material behavior under these conditions, reliable damage mechanisms associated with the increase of plastic deformation and the variation of the constitutive response true stress- true plastic strain with strain rate and temperature must be carefully assessed and validated, and if possible, incorporated in a unified model. Some important requirements should also be taken into consideration, such as

- a) material independence;
- b) physically based material constant;
- c) simple and reliable identification procedure for material parameters assessment;
- d) code implementation.

Recently, Bonora (1997) proposed a continuum damage mechanics model for ductile failure, derived in the framework proposed initially by Lemaître (1985), that with respect to other similar formulations, resulted to be material independent and to be capable to predict material behavior under any general state of stress conditions. On the other side, Milella (1998), proposed a new solid state equation (SSE) for the evolution of plastic flow with strain rate and temperature, showing an additional dependence of strain rate from temperature.

In order to set the basis for a unified model, the following issues have been addressed in this study:

- a) preliminary exploration of strain rate and temperature effect on ductile damage evolution;
- b) assessment of the validity of the SSE exploring the possibilities for a unified theory for BCC, HCP and FCC lattice metals.

The present study, in particular, focuses on two different structure materials, namely BCC and HCP metals. This is because BCC and HCP metals undergo large plastic

deformation activated by two different mechanisms: dislocation movements and twinning, respectively. Within the first class materials, three carbon steels have been analyzed: A533B, A508BC13 and A537. In addition, pure iron, niobium and tantalum have also been studied for comparison. As to HPC metals, α -titanium and β -titanium alloy have been considered. Steels and titanium, in particular, are structural materials, of interest to USAF since many weapon systems and aircraft components, are made by these metals. In addition, Ti-alloy is also strategic for aircraft design. The steels considered have been largely characterized and many data are available in the literature regarding both mechanical properties and fracture behavior. On the contrary, the Ti alloy, even if its mechanical properties are well known, has not been previously studied from the ductile damage point of view.

The following main goals for the research have been achieved:

- a) damage measurements on A533B and A537 steel at room temperature and low strain rate;
- b) damage measurement on both material under strain rate controlled conditions;
- c) investigation on stress triaxiality effect on material ductility under strain rate controlled conditions at room temperature;
- d) microscopy analysis of fracture surfaces
- e) BCC and HCP materials response to temperature and low strain rates;
- f) BCC and HCP materials response to temperature and high strain rates

In sections 3, a review of the damage model is given together with a detailed description of the experimental type of tests and procedure followed to measure damage parameters. Preliminary results on the damage evolution in low alloy steel are presented. In section 4, the background of the proposed SSE is given. Preliminary results obtained on several steels are presented with particular attention to A533B low alloy steel. In section 5, preliminary conclusions and a brief description of the work that will be made in the latter part of the research contract is summarized.

3.0 NON LINEAR CONTINUUM DAMAGE MECHANICS MODEL

3.1 Background

Plasticity damage in ductile metals is mainly due to the formation and growth of microcavities that initiate either due to the debonding from the ductile matrix or fracture of brittle inclusions, such as carbides and sulfides. Microvoids initiation and growth progressively reduces the material capability to carry loads leading the material to fail. If the principal micromechanism of failure is clearly identified, a correlation between the irreversible microscopical modifications that take place in the material microstructure and the global material response can be found in order to predict ductile failure in real life components and structures.

McClintock (1968) firstly recognized the role of microvoids in ductile failure process and tried to correlate the mean radius of the nucleated cavities to the plastic strain. Rice and Tracy (1969) analytically studied the evolution of spherical voids in a elastic-perfectly plastic matrix. In these pioneering studies the interaction effects between neighbor microvoids, microvoids coalescence process and hardening effects were neglected. Failure was postulated to occur when the cavity radius would reach a critical value (namely, *critical cavity growth*).

In the last decades, two different approaches have been proposed: the Gurson's model based approach and the continuum damage mechanics (CDM). In the first case, the plasticity damage due to microvoid formation is taken into account in a modified yield condition as proposed by Gurson (1977) were a porosity term, when activated, softens the material plastic response. Later, Koplik and Needleman (1988) and Needleman and Tvergaard (1984) modified the Gurson's model in order to include the acceleration in the failure process induced by voids coalescence.

The Gurson's model, and the models derived by its modification, are limited as a result of the fact that a very large number of material constants (up to nine, Brocks and Bernauer, 1995) is required and none of them is directly measurable on the material.

Continuum damage mechanics approach to ductile failure was initially developed by Lemaitre (1985) and Chaboche (1984) starting from the initial study of Kachanov (1986). In this approach, the complete set of constitutive equations is derived making the strain equivalence hypothesis (Lemaitre 1985) and assuming the existence of damage dissipation potential similarly to plasticity. Following this approach and suggesting the use of special forms for the damage dissipation potential, many damage models have been proposed (Chandrakanth and Pandey, 1993, Tay and Yang, 1986).

Recently Bonora (1997) proposed a general non linear CDM model for ductile damage independent of the material under investigation. In this model, the material parameters have a clear physical meaning and can be directly measured on the material performing simple experimental tests without the necessity of any iterative process.

Even if the CDM models proposed in literature are obtained in a general framework, their verification is always made in simple uniaxial case, where many experimental data

are now available (LeRoy et al., 1981; Bonora et al., 1994; Tai, 1990), and from which, the postulated damage potential, is often initially deduced. Very little attention to the predicting performance of the models in presence of multiaxial state of stress is usually given. Many important issues are generally (or intentionally) neglected: for instance, are damage parameters, that appear in the models, function of the state of stress? Do triaxiality change the critical damage, D_{cr} , at which failure occurs? Triaxiality modify the microvoids shape; in which quantitative way this process affects the kinetic law of damage evolution with plasticity? It is well known that multiaxial state of stress reduce material ductility. Do the CDM damage models predict the reduction of strain to failure as a function of triaxiality?

3.2. The Damage Model

Lemaitre (1996) firstly defined the CDM framework for plasticity damage. Here, damage is one of the thermodynamics state variables that takes into account the progressive loss of load carrying capability of the material as a result of some irreversible modifications, such as microvoids formation and growth, that initiate in the materials when intense plastic deformation occurs.

Physically speaking, damage can be defined as the reduction of the nominal section area of a given reference volume element (RVE) as a result of microcavities formation and growth:

$$D_{(n)} = 1 - \frac{A_{eff}^{(n)}}{A_0^{(n)}} \quad (3.1)$$

where, for a given normal n , $A_0^{(n)}$ is the nominal section area of the RVE and $A_{eff}^{(n)}$ is the effective resisting one reduced by the presence of micro-flaws and their mutual interactions. It is clear that this definition naturally leads to a tensor formulation of the damage variable, as proposed either by Chaboche (1984) and Murakami (1987). These formulations, even though formally correct, are very difficult to be used in practical applications as a result of the impossibility to experimentally identify material constants, damage components evolution and, most of all, their mutual interactions.

Here, for sake of simplicity and effectiveness, damage is assumed to be isotropic. This assumption, in many cases, is not too far from reality as a results of the random shapes and distribution of the included particles and precipitates that trigger plasticity damage initiation and growth.

In addition, the assumption that the strain associated with a damage state, under a given applied stress, is equivalent to the strain associated with its undamaged state under the corresponding effective stress (also known as the strain equivalence hypothesis) (Lemaitre, 1985), leads to the following definition for the damage variable D , using material stiffness reduction concept:

$$D = 1 - \frac{E_{\text{eff}}}{E_0} \quad (3.2)$$

where E_0 and E_{eff} are the Young's modulus of the undamaged and damaged material, respectively.

The complete theoretical framework for plasticity damage can be defined by means of the following additional assumptions:

- A dissipation potential f_D , similarly to the one used in plasticity theory, is assumed for damage;
- Absence of any coupling between damage and plasticity dissipation potentials is assumed. It follows that the total dissipation potential is given by linear superposition of the dissipation potential associated to plastic deformation f_p (that is the function of the actual stress tensor, σ , and of the isotropic and kinematic hardening back stress, R and X , respectively) and of the damage dissipation potential, f_D , (function of the damage associated internal variable Y and of the accumulated effective plastic strain, p):

$$f = f_p(\sigma, R, X; D) + f_D(Y; p, D) \quad (3.3)$$

- Damage variable, D , is coupled with plastic strain. The relation between damage and the irreversible strain in the micro/meso scale is expressed in the kinetic law of damage evolution where the rate of the plastic multiplier λ is proportional to the rate of the effective accumulated plastic strain, \dot{p} .
- Plastic damage dissipation is associated to the micro-cavities growth that is a highly non linear process; thus, the damage dissipation potential has to depend on the effective accumulated plastic strain that plays the role of an indicator of type of microvoids growth that is dominating the growth process.
- Damage processes are localized in the material micro-scale and their effects remain confined until the complete failure of several elementary volume elements, with the consequent appearance of a macroscopic crack, occurs;
- the same set of constitutive equations for the virgin material can be used to describe the damaged material replacing only the stresses with the effective ones and assigning a state equation for D .

This last statement does not answer to the question of what form should have the damage dissipation potential, from which the kinetic law of evolution for the damage variable is derived. Bonora (1997) proposed the following expression,

$$f_D = \left[\frac{1}{2} \left(-\frac{Y}{S_0} \right)^2 \cdot \frac{S_0}{1-D} \right] \cdot \frac{(D_{cr} - D)^{\frac{\alpha-1}{\alpha}}}{p^{\frac{2+n}{n}}} \quad (3.4)$$

where D_{cr} is the critical value of the damage variable for which ductile failure occurs. S_0 is a material constant and n is the Ramberg-Osgood material hardening exponent. α is the damage exponent: it determines the shape of the damage evolution curve and is related to the nature of the bound between brittle inclusions and the ductile matrix.

Equation (3.4) is a modified expression of the quadratic potential form initially proposed by Lemaître (1985), still recognizable in the square bracketed term. The modification is motivated by the consideration that the non-linearity of damage accumulation with plastic strain, experimentally verified for a large class of metals, has to result in a different dissipation if microvoids are mainly nucleating, either they are under steady growing or are coalescing with other voids. Even if experiments show that is extremely difficult to establish when, for a given plastic strain level, each microvoid growing phase either starts or ends, some attempts to incorporate these information in a model have been done. For instance, Tvergaard and Needleman (1984) modified the Gurson's model proposing a two-slopes porosity function in order to simulate a steeper decrease in the material stiffness as a consequence of voids coalescence. The potential given in Equation (3.4) states that dissipation due to damage process depends on the plastic strain level reached in the RVE. It is the damage exponent α that phenomenologically says which micro/mesoscopic effects are resulting from the three-phases (i.e., nucleation, growth and coalescence) void growth process together with plastic deformation.

Thus, the complete set of constitutive equation for a plastically deformed damaged material can be derived. Here the set is summarized for an isotropic hardening material (no kinetic hardening):

- *strain decomposition*

$$\dot{\varepsilon}_{ij}^T = \dot{\varepsilon}_{ij}^e + \dot{\varepsilon}_{ij}^p \quad (3.5)$$

- *elastic strain rate*

$$\dot{\varepsilon}_{ij}^e = \frac{1+\nu}{E} \frac{\dot{\sigma}_{ij}}{1-D} - \frac{\nu}{E} \frac{\dot{\sigma}_{kk}}{1-D} \delta_{ij} \quad (3.6)$$

- *plastic strain rate*

$$\dot{\varepsilon}_{ij}^p = \dot{\lambda} \frac{\partial f_p}{\partial \sigma_{ij}} = \dot{\lambda} \frac{3}{2} \frac{\dot{s}_{ij}}{1-D} \frac{1}{\sigma_{eq}} \quad (3.7)$$

- *plastic multiplier*

$$\dot{r} = -\dot{\lambda} \frac{\partial f_p}{\partial R} = \dot{\lambda} = \dot{p}(1-D) \quad (3.8)$$

- *kinetic law of damage evolution*

$$\dot{D} = -\dot{\lambda} \frac{\partial f_D}{\partial Y} = \alpha \cdot \frac{(D_{cr} - D_0)^{\frac{1}{\alpha}}}{\ln(\varepsilon_f / \varepsilon_{th})} \cdot f\left(\frac{\sigma_H}{\sigma_{eq}}\right) \cdot (D_{cr} - D)^{\frac{\alpha-1}{\alpha}} \cdot \frac{\dot{p}}{p} \quad (3.9)$$

more detailed description on the derivation of these Equations can be found elsewhere, (Bonora, 1997, Bonora and Newaz, 1997).

In Equation (9) the effect of stress triaxiality is taken into account by the function $f(\sigma_H/\sigma_{eq})$ given by,

$$f\left(\frac{\sigma_H}{\sigma_{eq}}\right) = \frac{2}{3}(1+\nu) + 3 \cdot (1-2\nu) \cdot \left(\frac{\sigma_H}{\sigma_{eq}}\right)^2 \quad (3.10)$$

that derives from the assumption that ductile damage mechanism is governed by the total elastic strain energy, (Lemaître and Chaboche, 1984) were σ_H is the mean hydrostatic stress..

The model needs five material parameters in order to be applied: the strain threshold (in uniaxial monotonic loading) ε_{th} , at which damage processes are activated. The theoretical failure strain, under complete uniaxial state of stress conditions, ε_f at which ductile failure occurs. The initial amount of damage present in the material, D_0 . The critical damage, D_{cr} , at which failure occurs and the damage exponent, α , that control the shape of damage evolution with plastic strain. Since, for the virgin material D_0 can be assumed equal to 0, the parameters can be reduced to four.

The experimental assessment of these parameters is given in detail in the following sections. The kinetic law of damage evolution needs the actual value of the function $f(\sigma_H/\sigma_{eq})$ for the current increment of total strain. However, it can be directly integrated in the simple case of uniaxial loading, for which $f(\sigma_H/\sigma_{eq})=1.0$, or in the case of proportional loading where $f(\sigma_H/\sigma_{eq})$ is constant. The solution for the uniaxial loading ,

$$D = D_0 + (D_{cr} - D_0) \cdot \left\{ 1 - \left[1 - \frac{\ln(\varepsilon / \varepsilon_{th})}{\ln(\varepsilon_f / \varepsilon_{th})} \right]^\alpha \right\} \quad (3.11)$$

is the simplest and allows a first general verification of the model. In Figure 3.2.1, the capability of the model to predict dissimilar damage evolutions as a function of the plastic strain, for different metals is shown. On the other hand, proportional loading

$$D = D_0 + (D_{cr} - D_0) \cdot \left\{ 1 - \left[1 - \frac{\ln(p / p_{th})}{\ln(\varepsilon_f / \varepsilon_{th})} \cdot f\left(\frac{\sigma_H}{\sigma_{eq}}\right) \right]^\alpha \right\} \quad (3.12)$$

is the simplest case to verify the capability of the model, using only information identified in the uniaxial case, to predict damage evolution under different stress triaxiality conditions. This is the case of geometries such as round notch tensile bar (RNB(T)) where stress triaxiality distributions remains constant along the minimum section independently of the applied load.

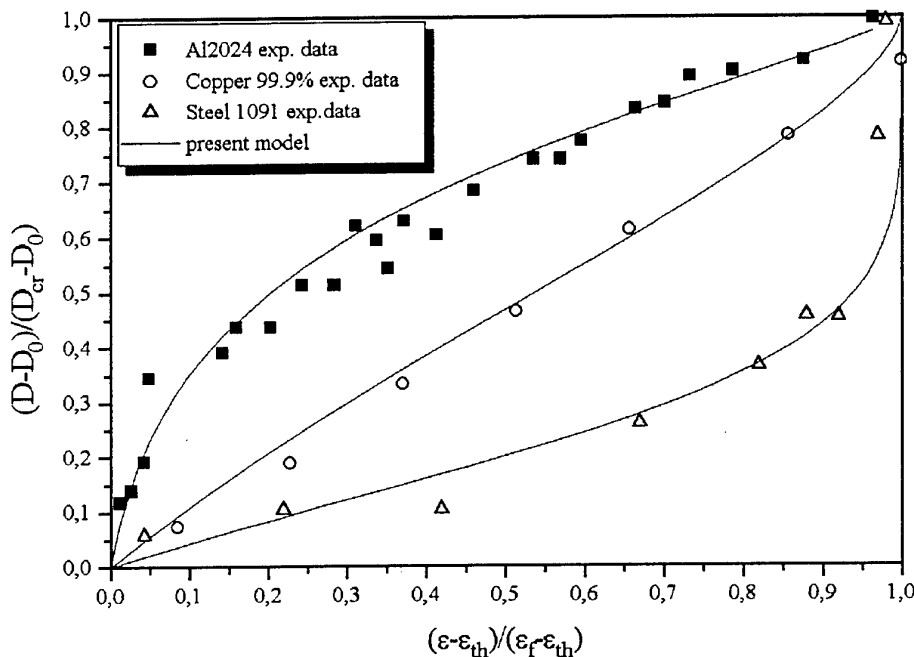


Figure 3.2.1 — The three basic damage evolutions with plastic strain characteristic of for aluminum, copper and steel

3.3 Stress Triaxiality, Damage Evolution and Parameters

It is well known that positive stress triaxiality reduces the material capability to plastically deform. Hancock and Mackenzie (1976) investigated this behavior in HY130 steels looking at the different modification in the void growth process due to stress triaxiality. Manjoine (1984) proposed an experimentally based expression that works fine for low alloy steels.

This feature in metal behavior is critical for those applications, such as metal forming and stamping, where the maximum reachable deformation is a design parameter. A damage model should be capable to predict this behavior without the need of additional hypothesis or parameter modification. Hancock and Mackenzie (1986) observed in HY130 steel that the strain at which microvoids start to grow, i.e. damage as previously defined starts to accumulate, is not dependent on the stress triaxiality even though the measure of this strain value can show a large scatter in the low triaxiality range. Starting from this observation, Bonora (1997) obtained from the non-linear damage model the evolution of the strain at failure, i.e. the material ductility, as a function of the stress triaxiality, as follows:

$$p = \varepsilon_{th} \left(\frac{\varepsilon_f}{\varepsilon_{th}} \right)^{1/f(\sigma_m/\sigma_{eq})} \quad (3.13)$$

This expression states that the reduction of the material ductility with the increase of stress triaxiality is specific for the material under investigation and depends on the value of the threshold and failure strain in the pure uniaxial state of stress. Bonora (1997) demonstrated for a large number of metals the validity of this expression showing how the prediction made with the Lemaître linear damage model, Rice and Tracy solution and the solution proposed by Manjoine, poorly approximate the effective experimental behavior.

As it will come out clear in the next section, it is important to spend few words on the role and meaning of ε_f . As stated before, ε_f is the theoretical strain to failure under uniaxial state of stress conditions. Unfortunately, this value does not correspond to the failure strain that can be measured from a simple uniaxial tensile test, using for instance a round bar. In fact, the occurrence of the necking process, well prior final failure, introduces a triaxial state of stress in the necking section, which can be of the order of 1.2-1.5, according to the hardening exponent of the material. This stress triaxiality reduces the nominal ductility that the material could eventually show if stress triaxiality would remain equal to 0.3333. Thus, the effective value of ε_f can be evaluated using Equation (3.13) with the requirement of the exact knowledge of the stress triaxiality under which failure occurs.

In the same way, to measure damage evolution with plastic strain, under pure uniaxial state of stress condition, is not so easy as it looks. Specimen geometries, where stiffness losses can be easily monitored using small strain gauges, usually show stress triaxiality fields that are not constant during the entire deformation process. On the other hand, in proportional loading specimen, such as round notch bar in tension, RNB(T), the location where failure occurs and damage accumulates most is the inner center of the minimum section where there is no chance for a direct measurement.

For these reasons, finite element analyses are required to evaluate the exact triaxial state of stress condition for a correct determination of damage parameters. Thus, if the damage model is capable to predict the reduction of material ductility with increasing triaxiality state of stress conditions, the value of the critical damage at which final rupture occurs has to be the same independently of stress triaxiality. In figure 3.3.1, on the log-plot where damage exponent is usually identified, the comparison between simulated damage measurements, under uniaxial ($TF=0.333$) and multi-axial state of stress conditions ($TF=0.666$), is given. Here, it is shown how the measure of the α exponent should lead to the same results if the appropriate strain to failure value is used (appropriate here means the right value of strain to failure that correspond to the TF value under investigation).

If the value of the critical damage should change with the increasing stress triaxiality the damage measurements should appear as given in figure 3.3.2 where the value of the $D_{cr}=0.8$ has been used to reduce the simulated data point instead of 0.75. In the same way, if the uniaxial strain to failure ε_f is used to reduce damage measurements obtained with geometries where stress triaxiality is not equal to 0.3333, the distribution of the experimental measurements in the log-plot should appear as given by the open symbols curve of figure 3.3.2.

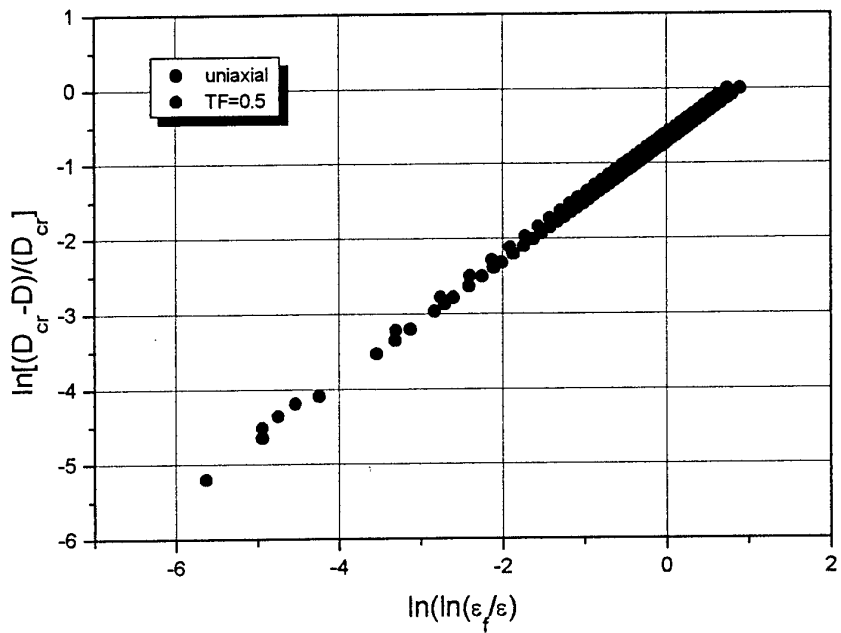


Figure 3.3.1 – Simulated damage measurement under different triaxial state of stress conditions reduced with respect to the same D_{cr} value and to the proper p_f and ε_f

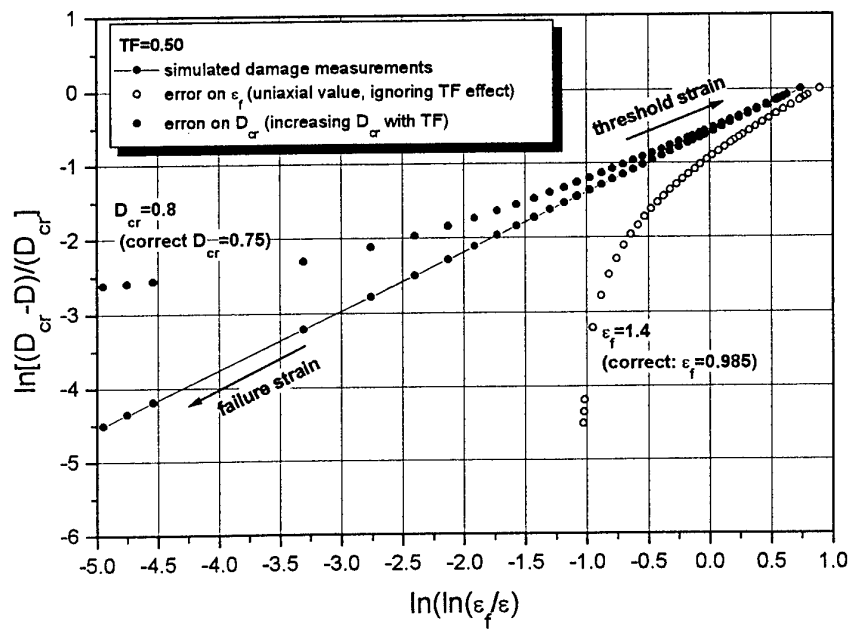


Figure 3.3.2 – Possible effect of D_{cr} and ε_f on the determination of α .

The damage threshold strain is the last parameter that needs to be identified. Bonora (1998) discussed in details the difficulties to directly measure this value from uniaxial tensile tests using for instance HG(T) specimen. This parameter can be measured either using Equation (3.13) in the high triaxiality regime or extrapolating uniaxial damage data recalling that from Equation (3.11) we can write:

$$\ln\left(\frac{D_{cr} - D}{D_{cr}}\right) = \alpha \ln\left[\ln\left(\frac{\varepsilon_f}{\varepsilon}\right)\right] - \alpha \ln\left[\ln\left(\frac{\varepsilon_f}{\varepsilon_{th}}\right)\right] \quad (3.14)$$

where the last right term is the intersection of a linear fit in the log-plane. Thus, named with C the value of this intersection, it follows that ε_{th} can be evaluated as,

$$\varepsilon_{th} = \varepsilon_f \exp\left[-\exp\left(\frac{C}{\alpha}\right)\right] \quad (3.15)$$

3.4 Quasi-Static Damage Measurements

Damage evolution in two similar low alloy steels, namely A533B and SA 537 Class 1 aluminum killed, has been investigated. The chemical compositions are given in Table VI.I and Table III.I, respectively.

C	Mn	Si	P	S	V	Nb	Al	N
0.19	1.45	0.38	0.013	0.005	0.05	0.033	0.025	0.012
0.20	1.43	0.37	0.011	0.008	0.06	0.032	0.022	0.014

Table III.I- SA 537 steel chemical composition

Since, the determination of damage parameters will require FEM simulation in order to verify the exact stress triaxiality condition under which damage has been measured, the plastic flow law (true stress-true strain) needs also to be measured.

The elastic-plastic material behavior was determined using for the A533B steel a flat rectangular tensile specimen, FRB(T), 12mm wide and 5.0mm thick and measuring strain with a clip-gauge with 25.4 mm reference length, as given in figure 3.4.1. Alternatively, for the SA 537 steel, small round bar in tension, RB(T), with a measure length of 36 mm was used. In figure 3.4.2 the geometry dimensions and a picture of the specimen are given. Several specimens have been tested in order to verify the quality of the measurements and its repeatability.

Figure 3.4.3 and 3.4.4 show the experimental plastic flow data measured up to necking localization for the A533B and SA 537, respectively. The plastic flow curve was fitted using a square polynomial in the $\ln(\sigma)$ - $\ln(\varepsilon_p)$ plot as given in Figure 3.4.5 where the fitting constants are also given. The Young modulus of the materials was assumed equal to 190.000 MPa with a yield stress σ_y of 360 MPa (SA 537) and 400 MPa (A533B).

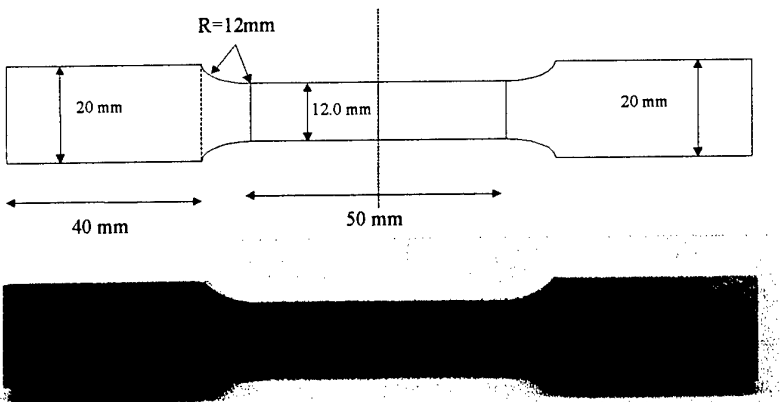


Figure 3.4.1 – FRB(*T*) specimen dimensions

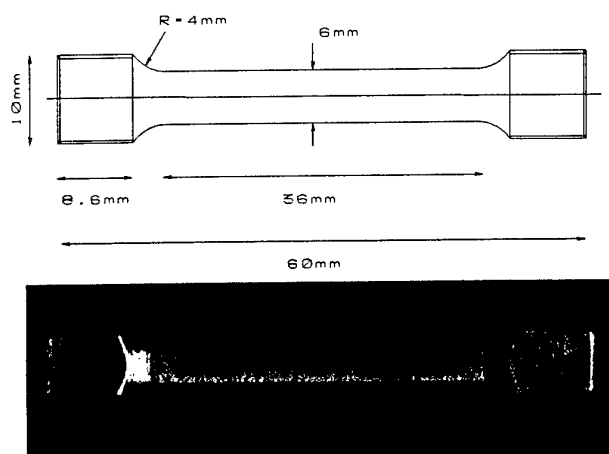


Figure 3.4.2 – RB(*T*) specimen dimensions

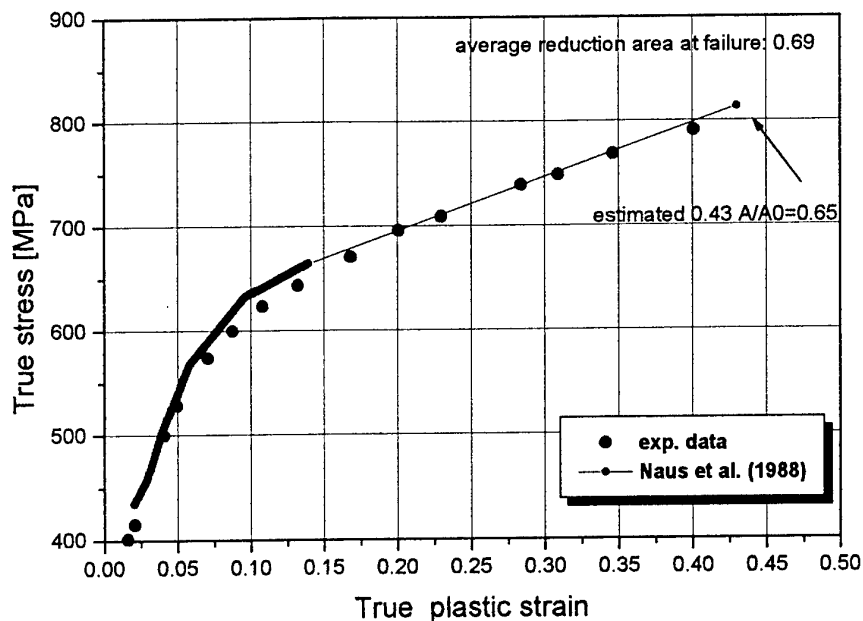


Figure 3.4.3 – Evolution of true stress with true plastic strain for A533B steel. Dots are actual experimental measurements, line indicates interpolated values obtained by Naus et al. (1988) on same material.

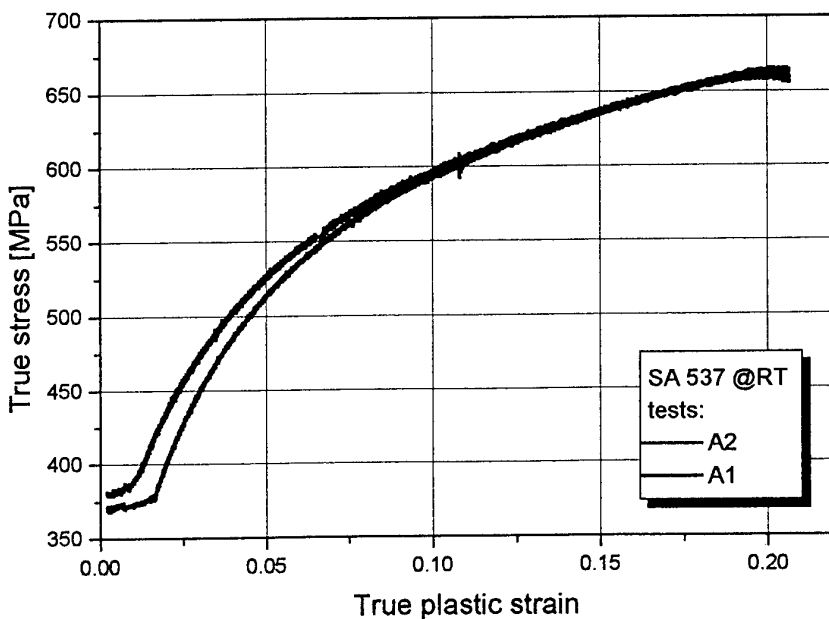


Figure 3.4.4 – Evolution of true stress with true plastic strain for SA537 steel.

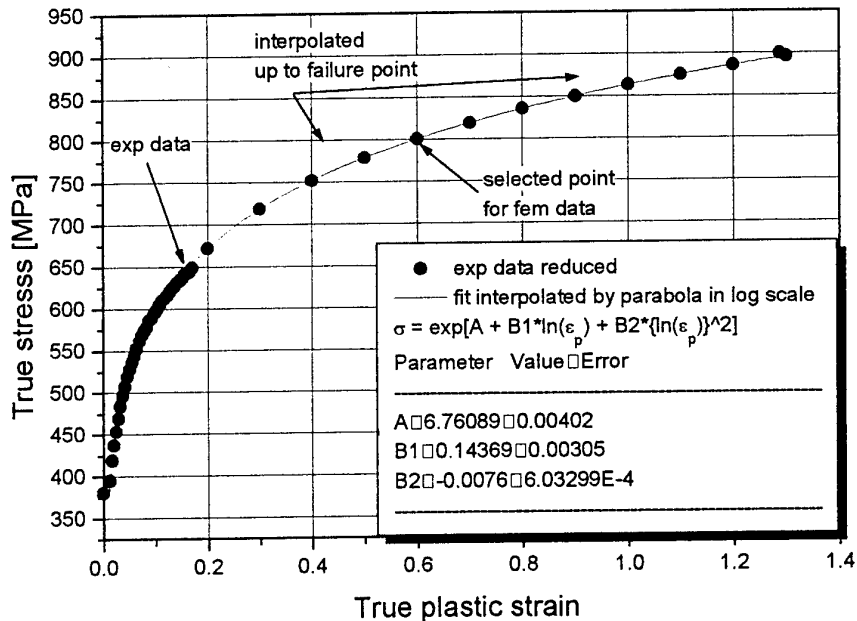


Figure 3.4.5 – Hardening law fitting for SA537 steel.

The evolution of ductile damage variable under quasi-uniaxial state of stress conditions was measured using HG(T) specimen, given in figure 3.4.6.

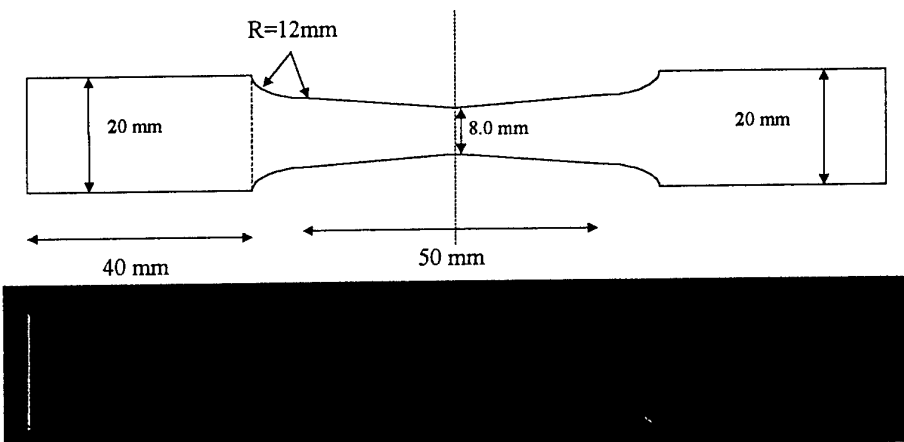


Figure 3.4.6 – HG(T) specimen geometry and dimensions for damage measurement

The experimental procedure is organized in the following steps:

- specimen surface at the minimum section, where failure will occur by localization of plastic deformation, was cleaned and a strain gauge (3×6.2 mm) was positioned

with the long side aligned with the axial direction using a two components epoxy glue. The strain gauge deformation limit was $\pm 20.0\% @120\Omega$.

- b) specimen was mounted on a MTS 100 KN hydrodynamic testing machine and a first loading ramp, imposing a remote displacement, was performed in order to recover machine and grip gaps;
- c) a sequence of loading and unloading were performed progressively increasing the maximum strain. During this phase the applied load, together with the strain gauge deformation, were continuously monitored. In addition, a clip-gauge, with a reference length of 25.4 mm, positioned along the thickness and across the minimum section, was used to have a double-check measurement of the strain in the minimum section and information on the damage localization. Each unloading was used to verify the loss of stiffness due to damage. Since the specimen has not a constant section, the true stress in the minimum section is unknown. However, the knowledge of the actual stress is not needed for the damage evaluation since from Equation 2 the stiffness reduction is the only datum necessary. Thus, geometric stiffness given as the applied load by the actual strain can be used for a direct measure of damage. The loading-unloading process is repeated until the maximum strain allowable for the strain gauge is applied.
- d) When the limit strain is reached, the strain gauge needs to be removed. Thus, the specimen was unloaded and a new strain gauge was positioned.
- e) Before running new damage measurements, a loading ramp, below the previously reached maximum strain, was performed in order to verify eventual positioning errors.
- f) Thus, the process, starting at the point b), can be repeated theoretically until complete failure of the specimen would occur. However, above a given strain level, as a result of the necking process that takes place in the minimum section, the positioning and balance of new strain gauges becomes impracticable.

This procedure, even if conceptually simple, is time consuming, since for a given loading rate the time required by any ramp becomes longer and longer. Attention must be paid since the entire measurement chain can be lost if the strain gauge deformation limit is accidentally exceeded. In addition, the replacement of the each strain gauge required a curing cycle of 3 hours at 50°C. The glue itself can be a limit to the number of unloading ramps that can be performed since glues, that can sustain high deformations, usually show poor fatigue performance. Here, the maximum true strain reached monitoring the deformation process with strain gauges was of the order of 40% and the number of the measurements performed was good enough to fully identify the damage parameters. Later, all specimens were loaded up to failure in order to provide the last damage data point through the measure of the effective resisting area at rupture.

In figure 3.4.7 and 3.4.9 the damage measurements obtained for SA 537 and A533B steels are given respectively, together with the damage exponent fitting plots, (figure 3.4.8 and 3.4.10).

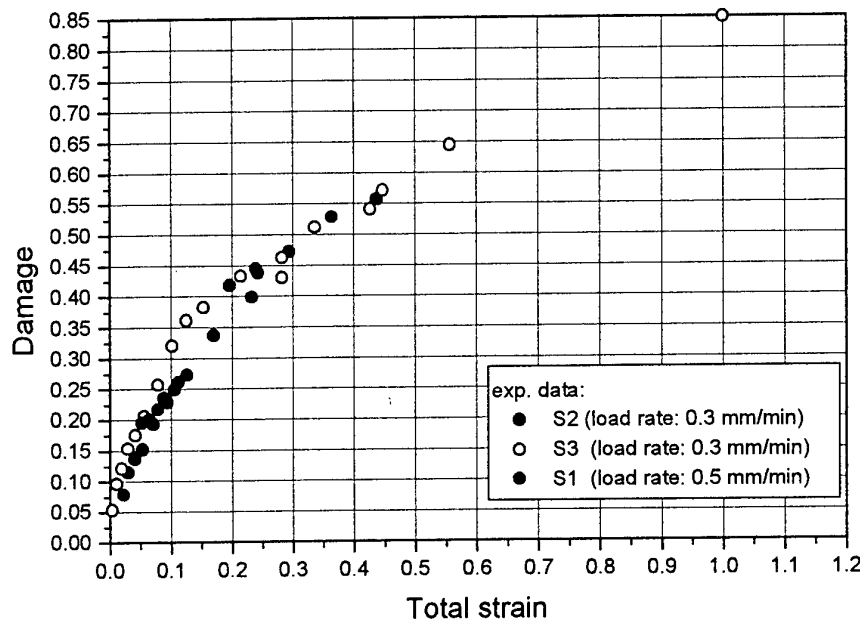


Figure 3.4.7 – Damage measurement for SA537 steel (low strain rate).

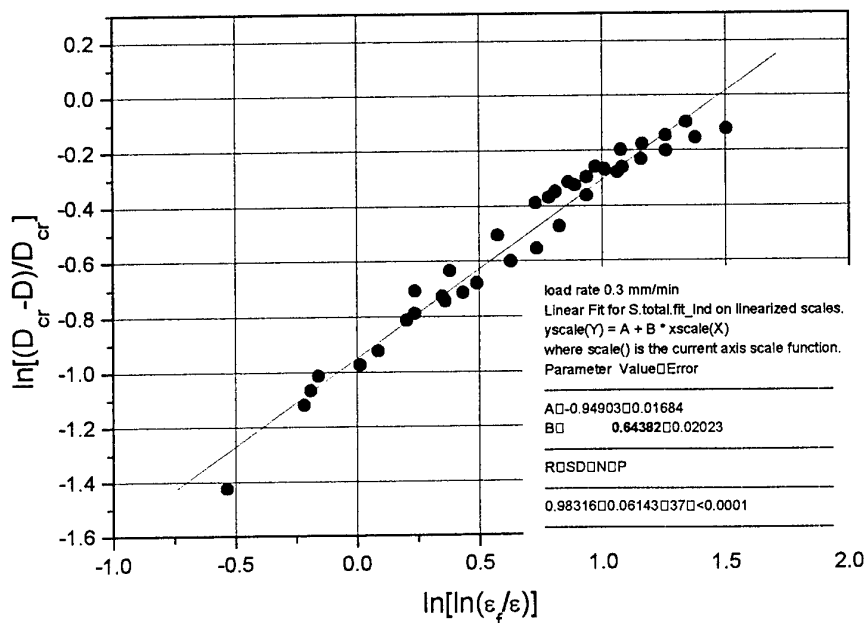


Figure 3.4.8 – Damage exponent fit for SA537 steel.

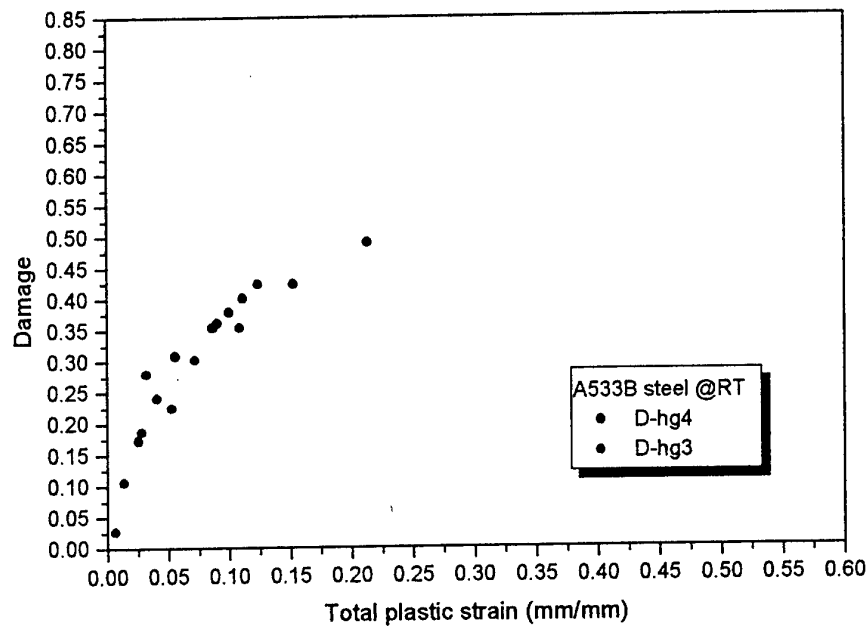


Figure 3.4.9 – Damage evolution with plastic strain in A533 steel

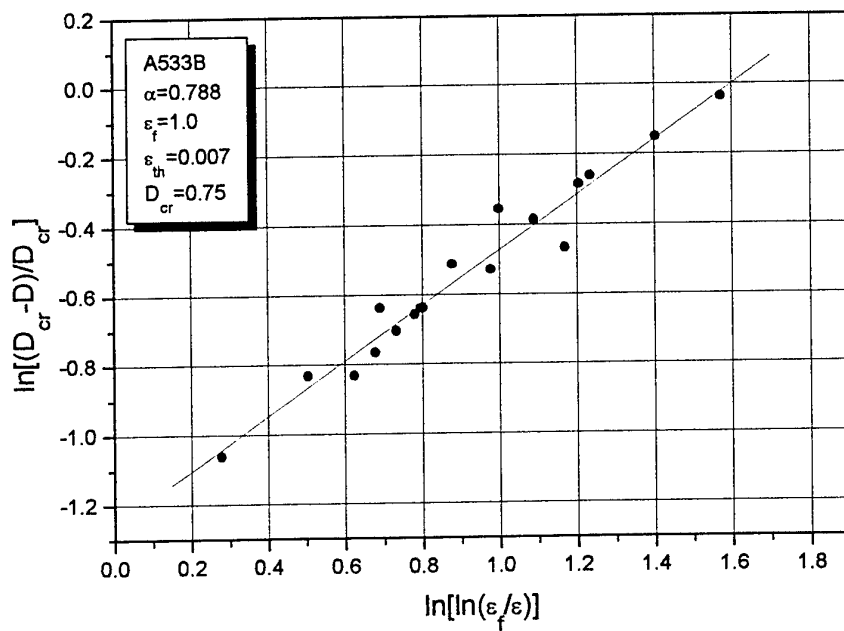


Figure 3.4.10 – Damage exponent fit for A533B steel.

3.5 Dynamic Damage Measurements

Possible dynamic effect on damage evolution has been investigated repeating the procedure for quasi-static damage under different controlled load rates. The material tested is the SA537 steel. All the tests have been conducted at room temperature.

Firstly, the dynamic effect on the plastic flow response of the material under investigation has been measured running a number of traction tests using round bar specimen geometry as depicted in figure 3.4.2.

Tensile tests have been performed using a 20KN Instron servo-hydraulic tensile machine. Three reference load rates have been selected. Each test has been repeated twice in order to verify the repeatability of the response and the experimental scatter. In table 3.5.1 the specimen matrix is given.

Table 3.5.1 – Test matrix for dynamic plastic flow response

Specimen	Load rate [mm/min]	Sampling rate [point/sec]	Nominal train rate [sec ⁻¹]
1A	0.01	1.0	4.63×10E-06
2A	0.01	1.0	4.63×10E-06
3A	10.0	50.0	4.63×10E-03
4A	10.0	50.0	4.63×10E-03
5A	100.0	50.0	4.63×10E-02
6A	100.0	50.0	4.63×10E-02

In all specimen tested failure occurred in the gauge length. The experimental scatter is limited and even though the selected strain rates are in the low range regime, an effect on the first yield strength has been clearly observed and quantified. In figure 3.5.1 and 3.5.2 the comparison of the global load vs elongation response under different strain rates is given.

From these measurements the true stress vs true strain curve have been derived, figure 3.5.2. Here, measurements up to the initiation of the necking process have been used to identify the hardening exponent. Bridgman solution has been used to estimate the true strain at fracture. Similarly, Bridgman correction has been used to update stress calculation after necking. In table 3.5.2 measures at fracture are summarized.

Table 3.5.2 – Experimental measurement at failure

Failure Strain [mm/mm]	Diameter at fracture [mm]	P [N]	Specimen Label	Nominal true stress at fracture [MPa]	Bridgman corrected stress [MPa]	Necking radius R [mm]
1.26976	3.180	9822	A1	1236	1161	5.84
1.32718	3.090	10045	A2	1339	1261	6.00
1.31042	3.116	9962	A3	1306	1219	5.20
1.34342	3.065	10155	A4	1376	1291	5.60
1.26599	3.186	10033	A5	1258	1153	4.13
1.25722	3.200	9799	A6	1218	1120	4.30

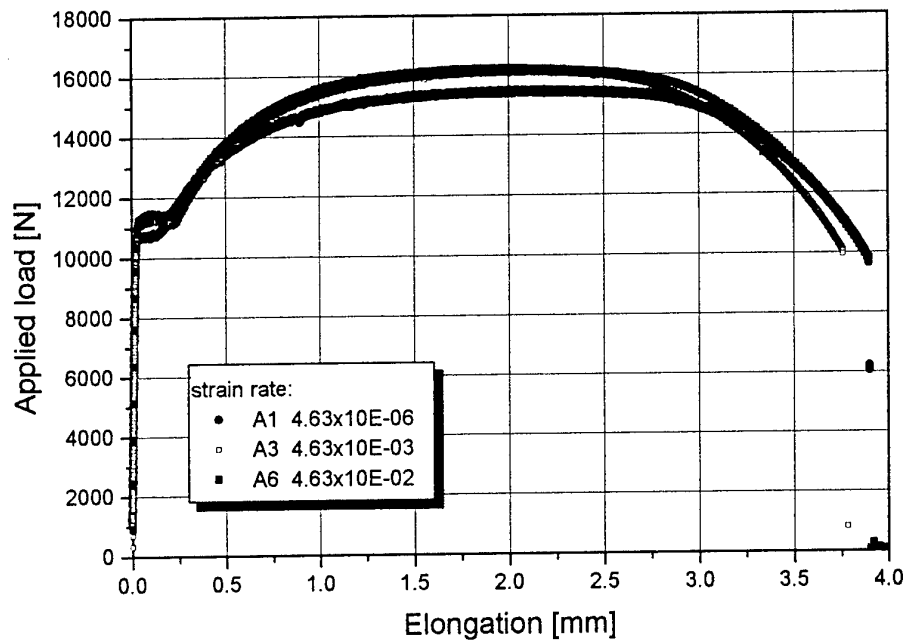


Figure 3.5.1 – SA537 load vs elongation response under different load rates

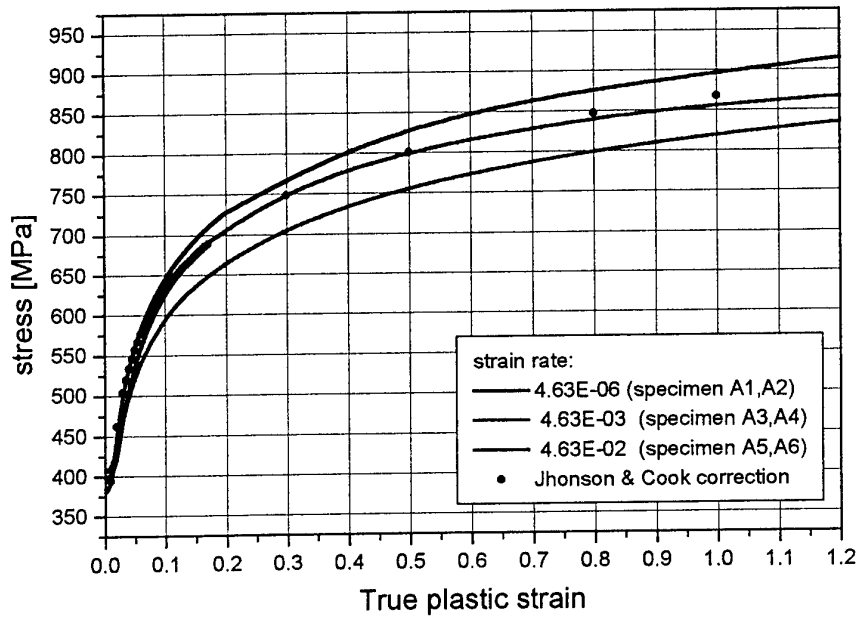


Figure 3.5.2 – Strain rate effect on flow curve in Sa537 steel

In order to give an accurate description of the plastic flow curve all over the entire true strain range up to failure a 2 order power law fit has been used. It has been verified that a Johnson and Cook correction for the strain rate effect allow to describe the evolution of the plastic flow under dynamic condition fairly well. Thus, the plastic flow curve has been given as:

$$\sigma = f(\varepsilon_p) \left[1 + C \cdot \ln \left(\frac{\dot{\varepsilon}}{\dot{\varepsilon}_0} \right) \right] \quad (3.5.1)$$

where

$$f(\sqrt{\varepsilon_p}) = \left[\exp 6.7088 + 0.10534 \cdot \ln (\sqrt{\varepsilon_p}) - 0.01425 \cdot \ln (\sqrt{\varepsilon_p}) \cdot \ln (\sqrt{\varepsilon_p}) \right] \quad (3.5.2)$$

with an initial yield strength of 380 MPa, a reference strain rate of 4.63E-06sec⁻¹ and C=0.0085.

The procedure followed to measure ductile damage evolution under quasi-static loading condition has been repeated increasing the load rate. In order to have a direct correlation with the uniaxial dynamic flow curves, the same load rates have been selected for the dynamic damage measurements. In table 3.5.3 the load rate matrix, together with the specimen id, is given.

Table 3.5.3 – HG(T) specimen id and load rate used for dynamic damage measurement

specimen	Load rate mm/min
S1	0.5
S2	0.3
S3	0.3
M1	10.0
M2	10.0
F1	100.0
F2	100.0

It has to be anticipated here that the corresponding strain rates are slightly different from the values indicated in table 3.5.1 due to the non uniform section of the HG specimen.

In figure, 3.5.3 and 3.5.4, the damage measurements at different load rate are plotted as a function of the total accumulated plastic strain. From the comparison with the quasi-static damage measurement, no significant differences that can be ascribed to the load rate effect arise.

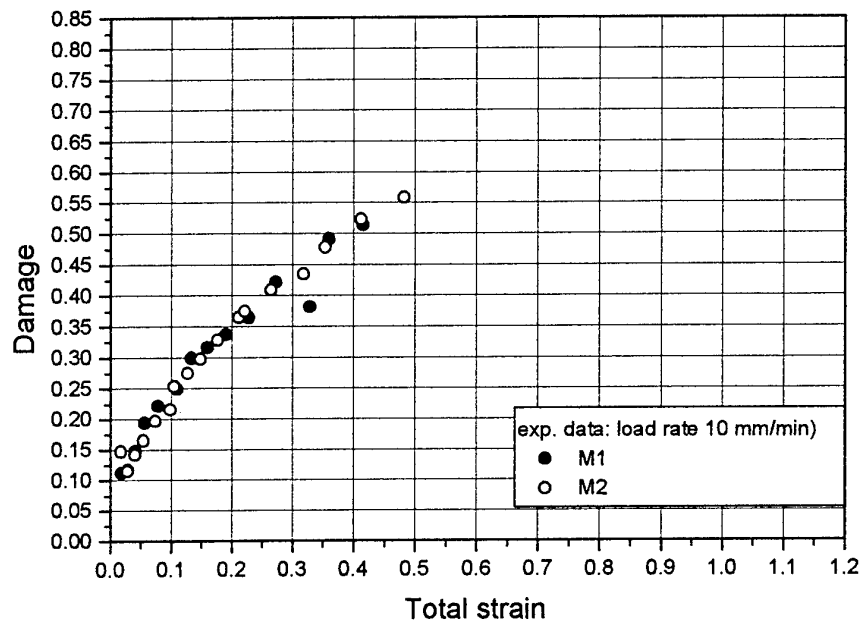


Figura 3.5.3– Damage measurement in HG specimen at load rate 10 mm/min

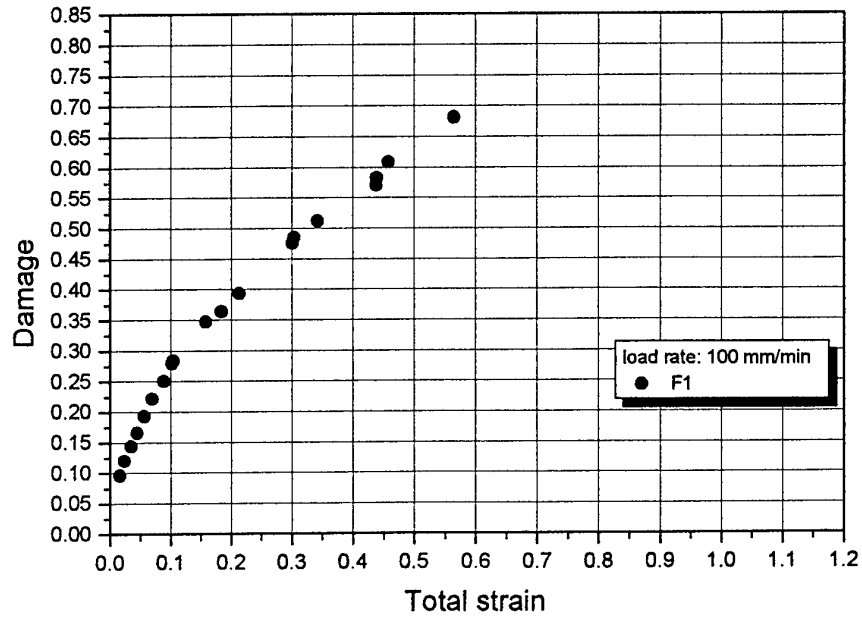


Figura 3.5.4– Damage measurement in HG specimen at load rate 100 mm/min

A clear dynamic effect is lacking on all damage parameters. A possible effect on the damage exponent has been verified plotting all the damage measurement relative to the

different specimens tested at the same load rate on the $\ln[(D_{cr} - D)/D_{cr}] - \ln[\ln(\varepsilon_f / \varepsilon)]$ plot. The comparison, reported in figure 3.5.5, 3.5.6 and 3.5.7, shows a α value of 0.64, 0.55 and 0.57 respectively.

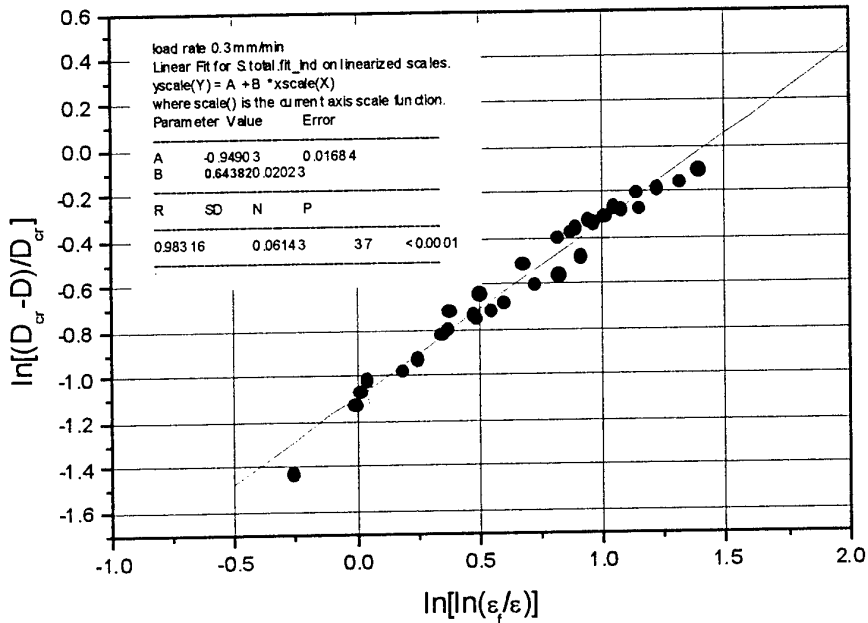


Figure 3.5.5 – Damage exponent ($\varepsilon_f=1$) (specimen S1, S2, S3)

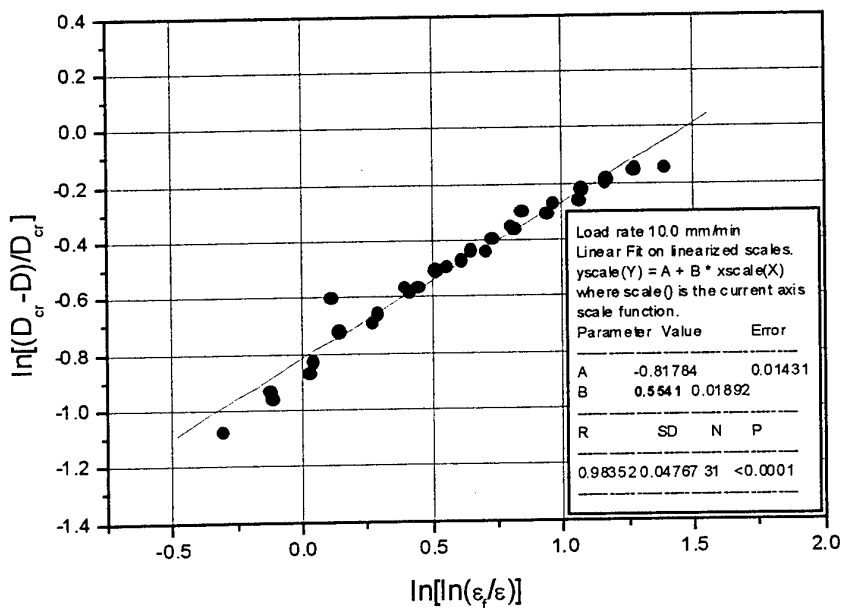


Figure 3.5.6 – Damage exponent ($\varepsilon_f=1$) (specimen M1, M2)

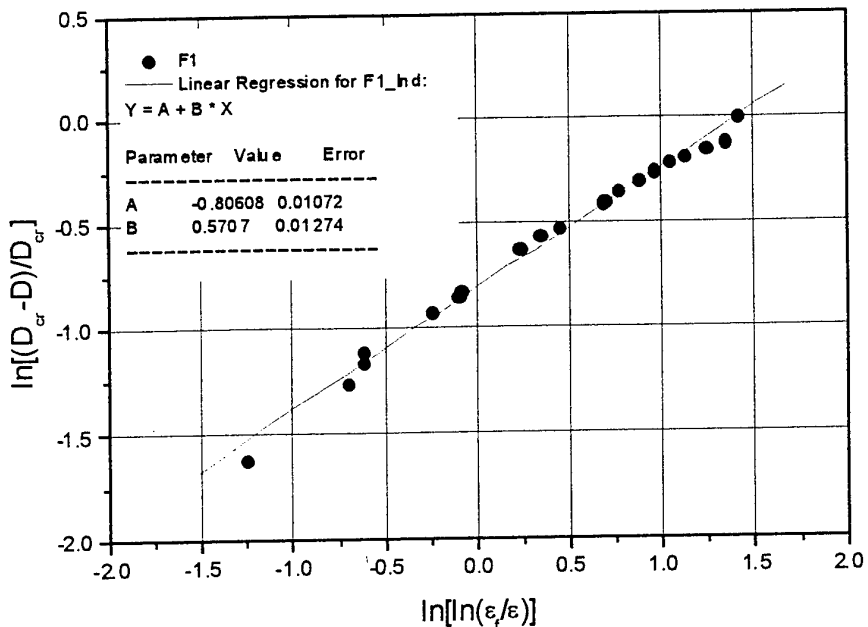


Figure 3.5.6 – Damage exponent ($\varepsilon_f = 1$) (specimen F1)

Since damage measurements can be performed over a limited strain range, as a result of the necking process that makes impossible the correct positioning of new strain gauges in the measurement chain, strain to failure and critical damage have been derived from direct measurements onto the fracture surfaces, as summarized in table 3.5.4.

Table 3.5.4 – Fracture surface measurement on HG specimens

A_{ext} [mm ²]	A_{in} [mm ²]	Label	Load.rate	D_{cr}	ε_f [mm/mm]
14.96	6.58	F1	100	0.835	0.9835
15.58	6.07	F2	100	0.848	0.94289
14.94	6.33	M1	10	0.841	0.98484
15.80	5.32	M2	10	0.867	0.92887
15.43	6.79	S2	0.3	0.830	0.95257
14.69	6.43	S3	0.3	0.839	1.00171

Each fracture surface shows a morphology in which two zones can be clearly identified. The inner zone is darker and shows clear ductile failure by void growth. The outer zone is lighter and non planar with respect to the mean section, showing clear evidence of severe ductile shear failure as reported for example in figure 3.5.7 and 3.5.8



Figure 3.5.7 – Fracture surface morphology for HG specimens

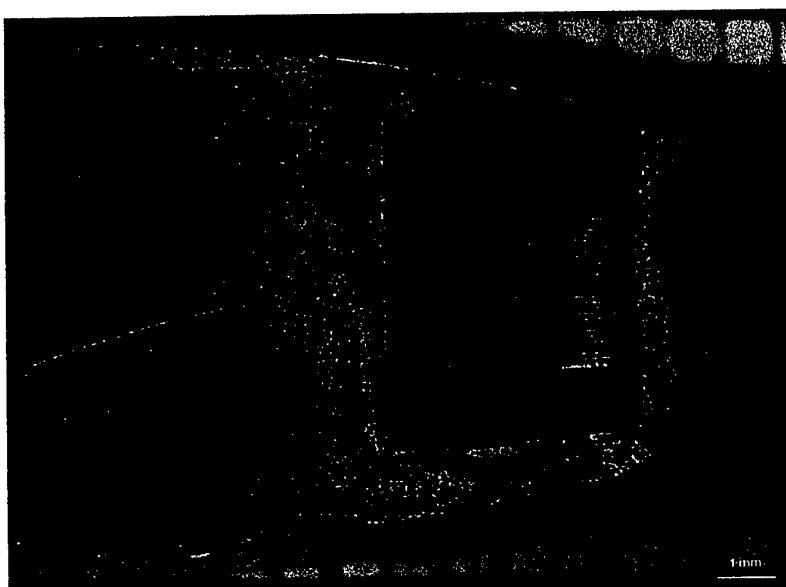


Figure 3.5.8 – Fracture surface morphology for HG specimens (side view)

The inner zone is the area where damage processes are localized as a consequence of higher stress triaxiality. Thus, it can be assumed that ductile tearing due to void growth and coalescence can occur until the section is capable to sustain the redistributed excess of load. When instability is reached, the remaining part of the section instantaneously fails by shear. Thus, the inner zone can be used to measure the critical damage at failure where the reference surface is the initial value (40 mm^2 in this case).

Different consideration should be made for the estimation of the strain to failure. In fact, even though the inner part of the section is where damage processes are activated most, the entire section deforms under the current applied load. Thus, strain to failure can be estimated as:

$$\varepsilon_f = \ln\left(\frac{A_{ext}}{A_{in}}\right)$$

It is important to observe that both strain to failure and damage measurements confirm a clear lacking of any dynamic effect on these parameters. Thus, in table 3.5.5, damage parameter for SA537 steel are summarized.

Table 3.5.5 – Damage Parameters for SA537 steel

ε_{th}	ε_f	D_{cr}	α
0.0195	1.54	0.85	0.64

3.6 Triaxiality effect on material ductility

Stress triaxiality plays a heavier role on material behavior, even more than strain rate and temperature, (Johnson and Cook, 1987). It is well known that positive stress triaxiality dramatically reduces the material capability to deform reducing the effective strain to failure. Bonora (1997) pointed out that a continuum damage model should be able to predict this behavior without the need of additional hypothesis or theoretical adjustment. Bonora (1998), verified the capability of eqn. 3.14 to predict the effective reduction of ductility with stress triaxiality for several classes of metals. In figure 3.6.1 a comparison of the prediction obtained using eqn. 3.14 is given for Q1 steel as investigated by Hancock and Meckenzie (1976) together with other model predictions. It is worth to note here that the damage model prediction is very close to the one proposed by Manjoine that was obtained using a phenomenological fitting equation. Here, the CDM model predicted behavior has the support of a physical and theoretical framework.

Since eqn. 3.14 is directly derived from the proposed damage framework, the stress triaxiality vs ductility diagram represents an additional verification for the model effective capability under multiaxial state of stress conditions.

In addition, a possible dynamic effect on material ductility reduction due to stress triaxiality has not been yet explicitly addressed in the literature, as far as the authors are aware of. Thus, in this phase of the work an extensive experimental study has been performed testing round notched bar specimen, with different notch radii, under different load rates.

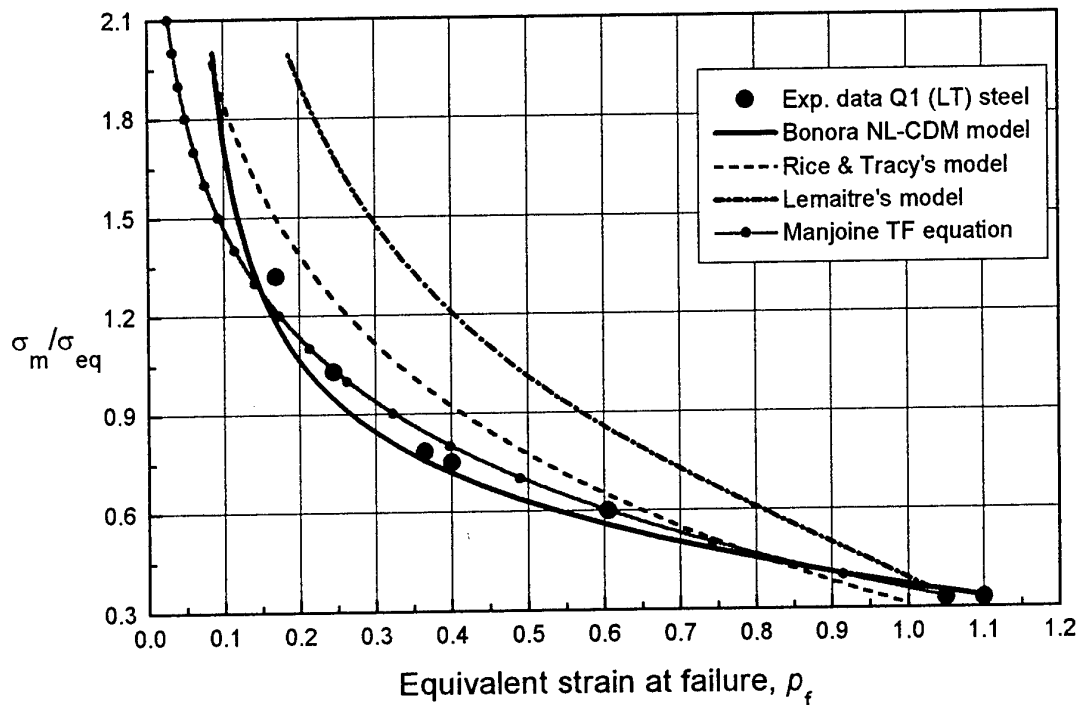


Figure 3.6.1 – Reduction of material ductility with increasing stress triaxiality: comparison for a Q1 steel (after Hancock and Meckenzie, 1976) of different models.

Round notch tensile bar, RNB(T), is a very peculiar specimen geometry characterized by the following important properties:

Firstly, this is proportional loading geometry, i.e. stress components along the minimum section increase of the same rate when the remote applied load increases. This means that the triaxiality factor given as the ratio between the first invariant of the stress tensor divided by the effective equivalent stress (that is the second invariant):

$$TF = \frac{\sigma_x + \sigma_y + \sigma_z}{\sigma_{eq}} \frac{1}{3}$$

has a distribution along the minimum section that is independent of the applied load. This statement is true both when the section is in the elastic range and when it is fully in the plastic range. For those situations in which the section is partially plasticized the statement does not hold, but it has to be said that transition to fully plasticization of the minimum section usually occurs quickly in the loading process.

The second important feature is the axial symmetry. This property allows easy and accurate 2D finite element simulation without the influence of any thickness effect. Here, the state of stress for any section is fully plane strain.

Finally, in this geometry it is possible to have a direct measurement of the plastic deformation along the minimum section monitoring only the diameter reduction. In fact, if the notch radius is not too small, plastic strain distribution along the minimum section is almost uniform. A direct measure of strain can be obtained using the well known Bridgman formula:

$$\varepsilon = 2 \ln \left(\frac{\Phi_0}{\Phi} \right)$$

where Φ_0 and Φ are the initial diameter and the actual one, respectively. Stress triaxiality depends of the notch radius only and it is independent of the ratio between the minimum and the remote diameter.

In this research, a number of RNB(T) specimens with the notch radius of 1.25, 2, 4 and 10 mm respectively, have been obtained from the same block of material from which HG(T) and RB(T) specimen were previously machined. In figure 3.6.2, a picture of the different notched geometries is given.

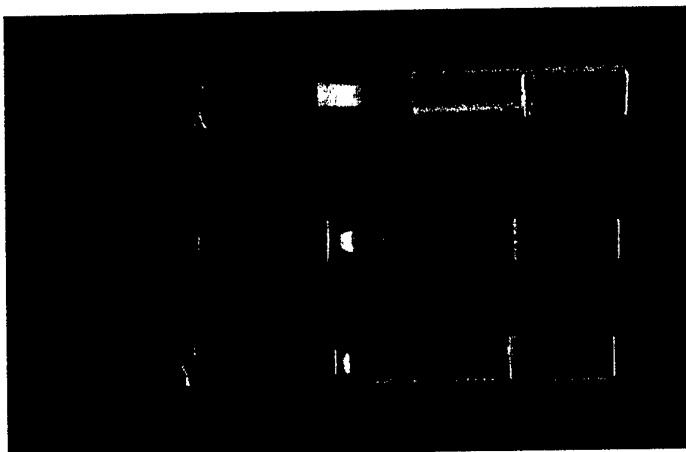


Figure 3.6.2 – RNB(T) specimen for SA537 steel.

Here, the minimum section is constant and equal to 5 mm for all notch radii and the remote diameter is 10 mm. These specimens have been tested at different load rates, as for the other specimen geometries. In table 3.6.1 the load rates and specimen id and geometry are summarized.

During each test, the reduction of the minimum diameter as a function of the applied load has been monitored continuously. The diameter reduction has been measured using a traditional clip gauge and an appropriate pinch gauge designed and built for the purpose and depicted in figure 3.6.3.

Table 3.6.1 – Summary of the results and testing parameters for RNB(T) specimens

$\Delta\Phi$ [mm]	Label	Notch Radius [mm]	Load Rate [mm/min]	Fracture Area [mm ²]	TF	ϵ_f
1.0695	R125A	1.25	0.1	12.13313	1.329	0.48134
1.054	R125F	1.25	100	12.22901	1.35	0.47347
1.1823	R125D	1.25	1	11.44671	-	0.53958
1.1823	R125C	1.25	1	11.44671	-	0.53958
0.9424	R125B	1.25	0.1	12.93051	1.33	0.41769
1.1455	R125E	1.25	10	11.66845	1.346	0.52039
1.14	R125I	1.25	100	11.70177	1.35	0.51754
1.11	R125H	1.25	10	11.88437	1.346	0.50206
1.188	R125G	1.25	0.1	11.41255	1.331	0.54257
1.255	R2F	2	10	11.0149	-	0.57803
1.346	R2E	2	10	10.4861	-	0.62723
1.433	R2A	2	0.1	9.99271	1.175	0.67543
1.1931	R2B	2	0.1	11.38204	1.162	0.54525
1.351	R2C	2	1	10.45743	-	0.62997
1.48	R2H	2	100	9.73111	1.183	0.70195
1.2092	R2D	2	1	11.28597	-	0.55372
1.35	R2G	2	100	10.46316	1.183	0.62942
1.258	R4H	4	100	10.99726	1.001	0.57964
1.2586	R4G	4	100	10.99374	1.001	0.57996
1.758	R4C	4	1	8.25473	-	0.86649
1.7247	R4F	4	10	8.42518	-	0.84606
1.6359	R4D	4	1	8.88822	-	0.79255
1.4145	R4B	4	0.1	10.09663	1.032	0.66508
1.525	R4A	4	0.1	9.48389	1.04	0.72769
1.1864	R4E	4	10	11.42214	-	0.54173
1.806	R10C	10	1	8.01211	-	0.89633
1.82	R10D	10	1	7.94203	-	0.90511
1.911	R10E	10	10	7.49399	-	0.96318
1.752	R10G	10	100	8.28532	0.9554	0.8628
1.8102	R10H	10	100	7.99105	0.9722	0.89896
1.886	R10A	10	0.1	7.61578	0.9438	0.94706
1.8198	R10F	10	10	7.94303	-	0.90499
	R10B	10	0.1		0.95	0.748

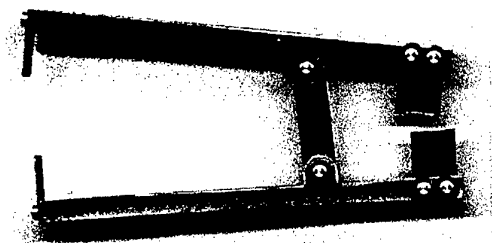


Figure 3.6.3 – Pinch-gauge for diameter reduction measurement in RNB(T) specimen

During each test, the global response, applied load vs diameter reduction, has been monitored continuously. In figure 3.6.4-3.6.7 the comparison of is given for the different notch radii at constant load rate.

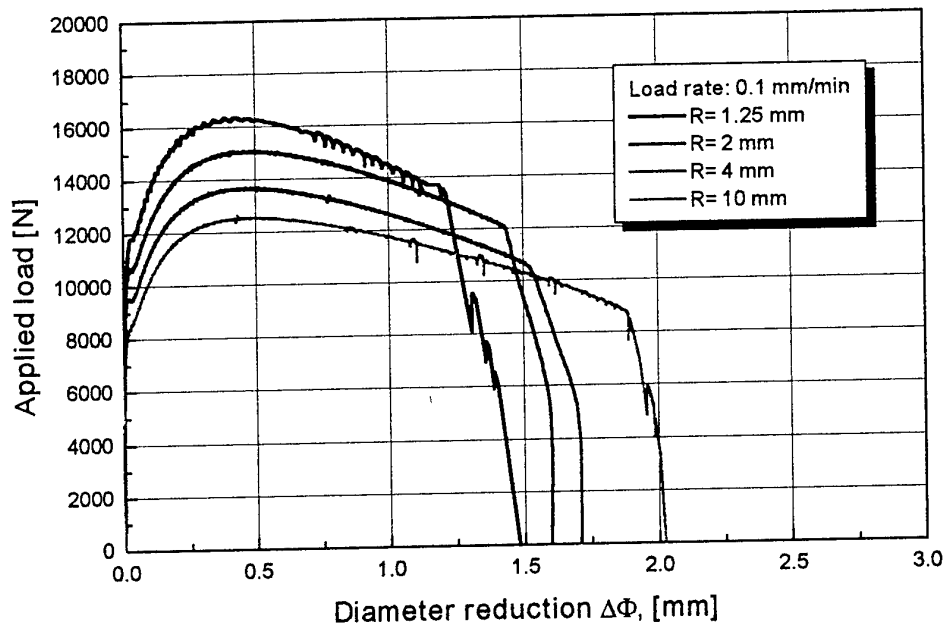


Figure 3.6.4 – Comparison of the P - $\Delta\Phi$ response at 0.1 mm/min

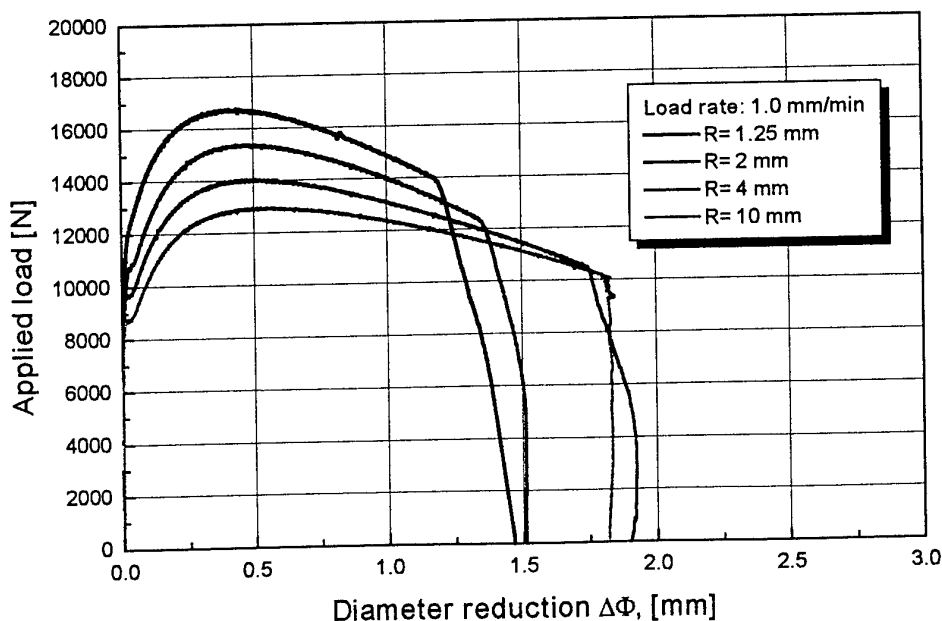


Figure 3.6.5 – Comparison of the P - $\Delta\Phi$ response at 1.0 mm/min

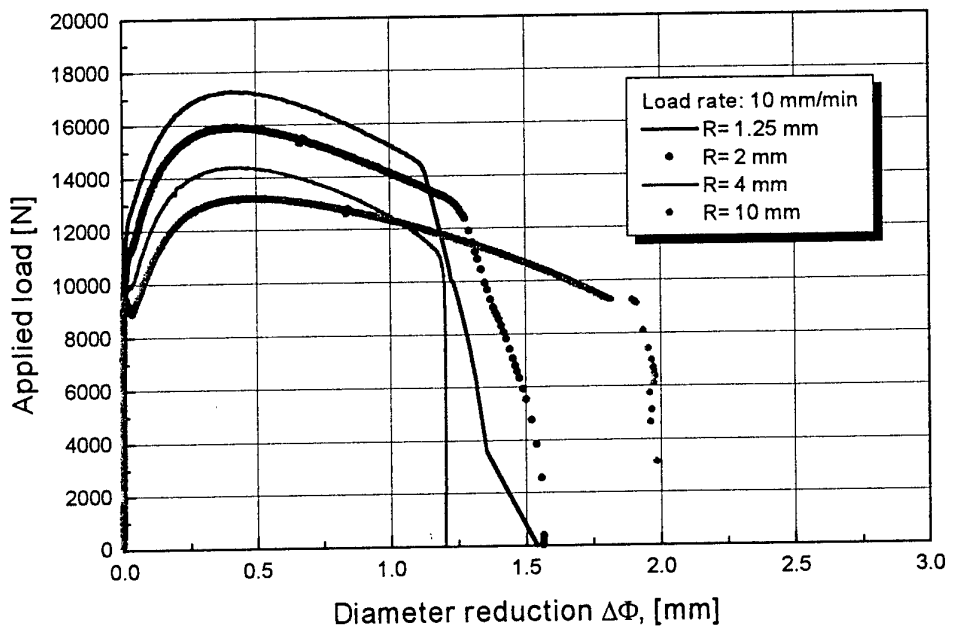


Figure 3.6.6 – Comparison of the P - $\Delta\Phi$ response at 10 mm/min

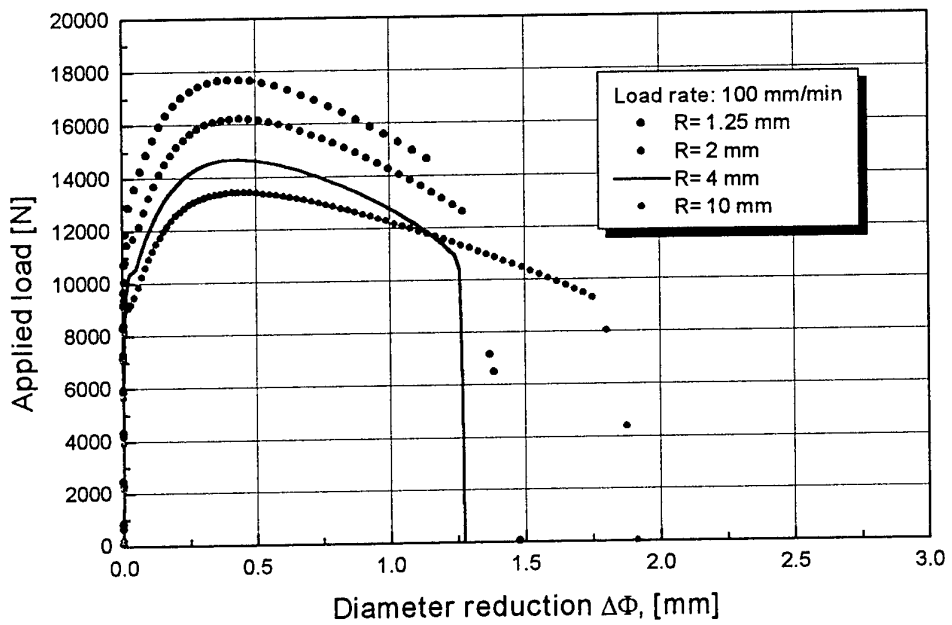


Figure 3.6.7 – Comparison of the P - $\Delta\Phi$ response at 100 mm/min

Since, higher notch radius corresponds to higher maximum applied load and a smaller diameter reduction, these comparisons show that the load rate increases the value of the maximum load, as given for instance in figure 3.6.8 where the different curves obtained at different load rates for $R=2$ are given.

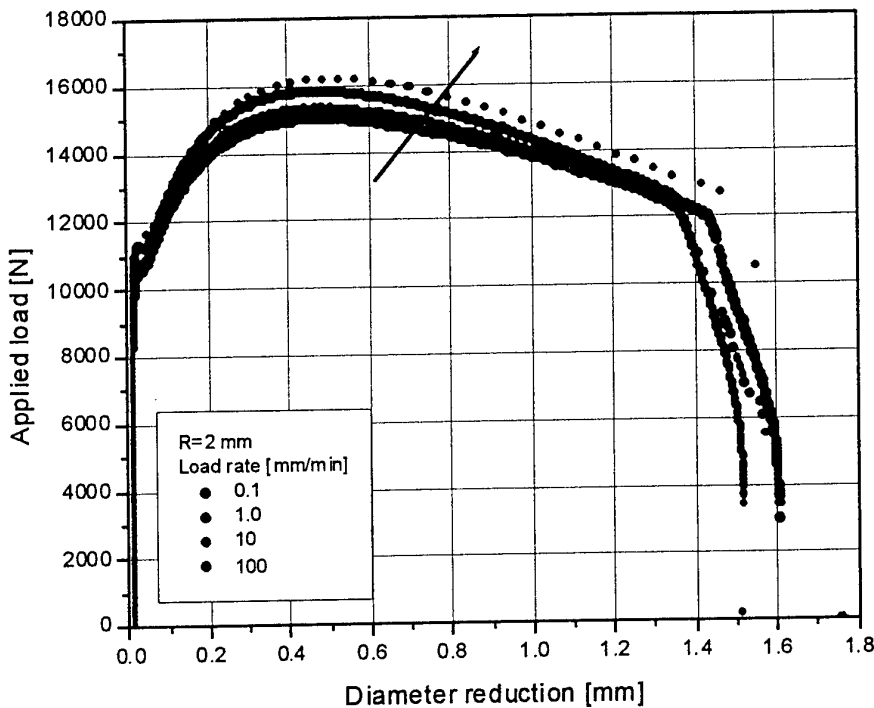


Figure 3.6.8 – Load rate effect on RNB(T) $R = 2\text{mm}$ global response

The analysis of the strain to failure measurements, obtained using the Bridgman formula, confirms, again, the absence of any effect that can be imputed to the load rate. Even for specimens tested at 100 mm/min the variation of minimum diameter at fracture is very limited and in the range of the material experimental scatter.

This result is very important since it confirms that strain to failure, at least in the low strain rate range, is scarcely affected by the deformation velocity even under multi-axial state of stress conditions. In addition, this result implies that at least two of four of damage parameters are load rate insensitive opening the question if a ductile damage model, as proposed, should or should not depend explicitly on the strain rate. The experimental results obtained on both HG(T), RB(T) and RNB(T) seems to indicate that strain rate effect should be incorporated in the material plastic flow curve while damage evolution should not include a strain rate term. These preliminary considerations are supported by the work performed by Johnson and Cook (1987) who came to similar conclusions.

3.7 Microscopy Analysis of Fracture Surfaces

Each RNB(T) specimen fracture surface has been analyzed using scanning electron microscope (SEM) in order to obtain physical evidences of the failure process. In figure 3.7.1- 3.7.4 the comparison for RNB(T) with $R=1.25$ and $R=10$ at two different load rates, 0.1 and 100 mm/min respectively, is given.

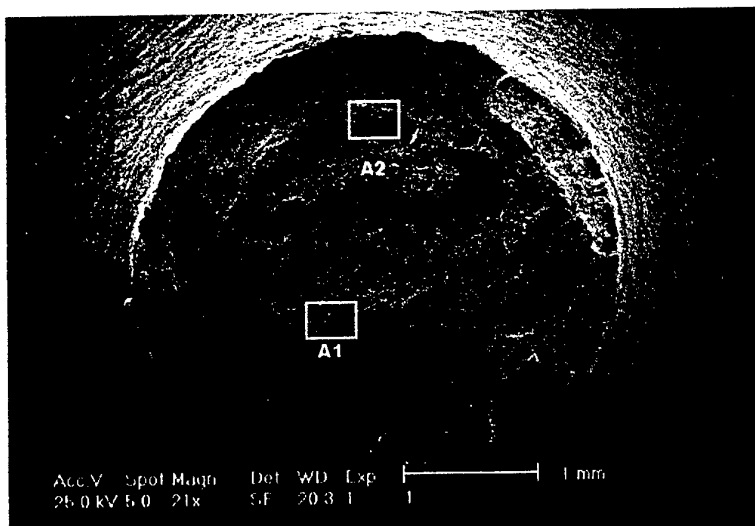


Figure 3.7.1 – Fracture surface specimen R125A, load rate 0.1 mm/min (21X)

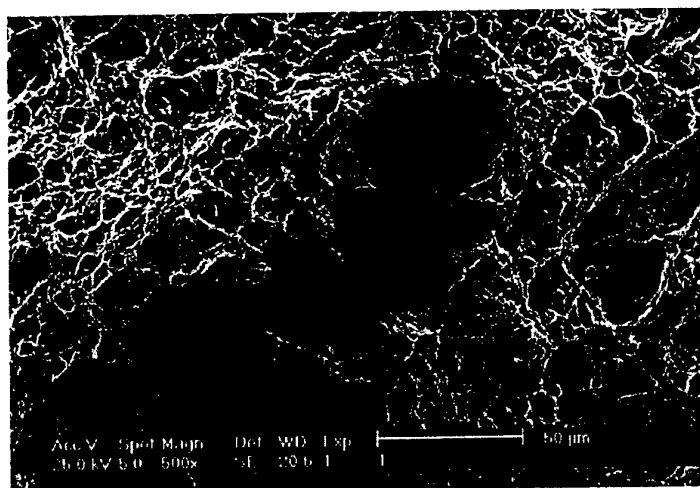


Figure 3.7.1a - Detail A1- microvoids coalescence (500X) in the inner region

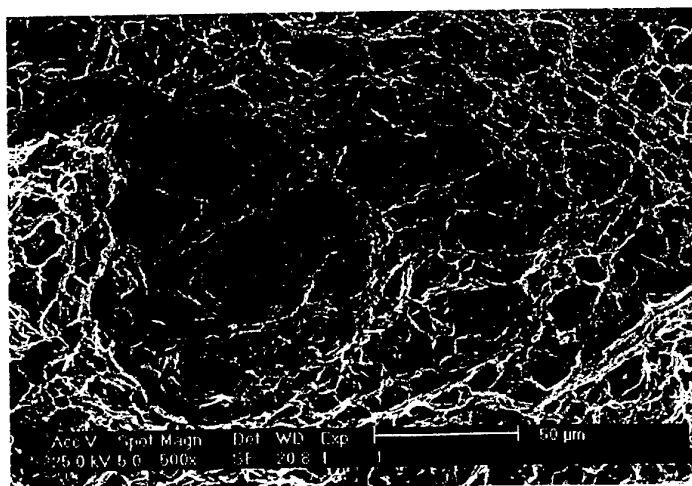


Figure 3.7.1b - Detail A2- smaller nucleated microvoids in the outer region, same scale as above picture (500X)

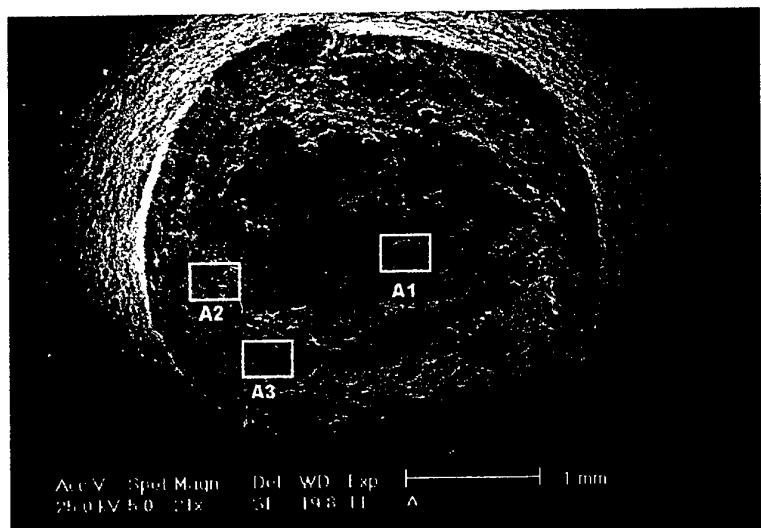


Figure 3.7.2 – Fracture surface specimen R125F, load rate 100 mm/min (21X)

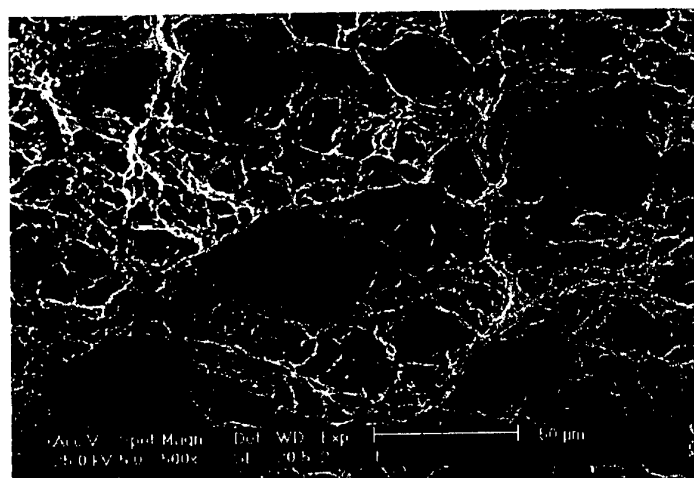


Figure 3.7.2a - Detail A1- microvoids coalescence (500X)in the inner region

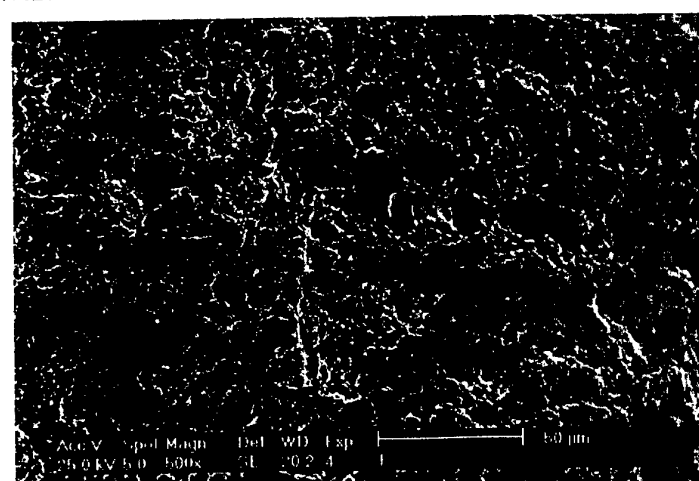


Figure 3.7.2b - Detail A3- smaller nucleated microvoids in the outer region, same scale as above picture (500X)

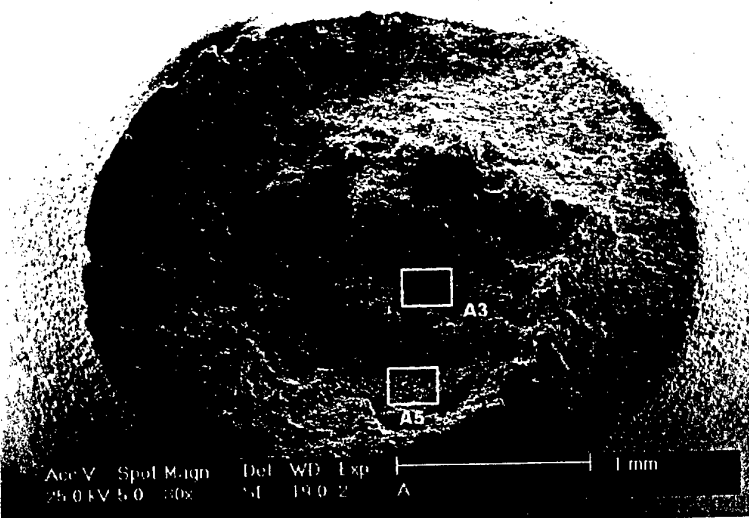


Figure 3.7.3- Fracture surface specimen R10A, load rate 0.1 mm/min (30X)

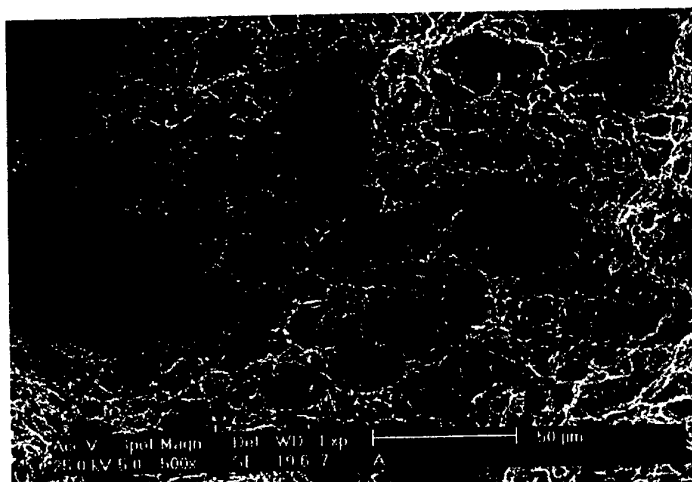


Figure 3.7.3a - Detail A3- microvoids coalescence (500X) in the inner region

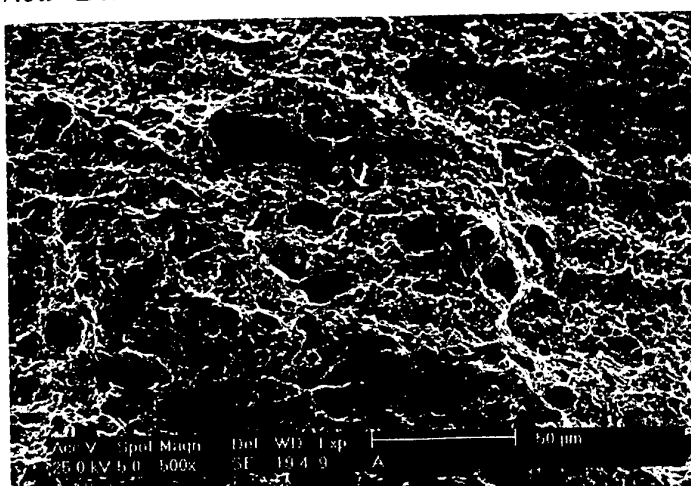


Figure 3.7.3b - Detail A5- smaller nucleated microvoids in the outer region, same scale as above picture (500X)

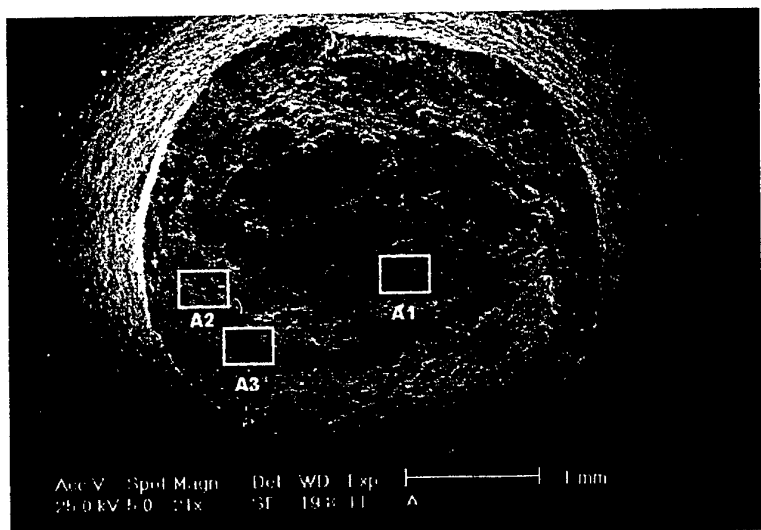


Figure 3.7.4- Fracture surface specimen R125F, load rate 100 mm/min (21X)

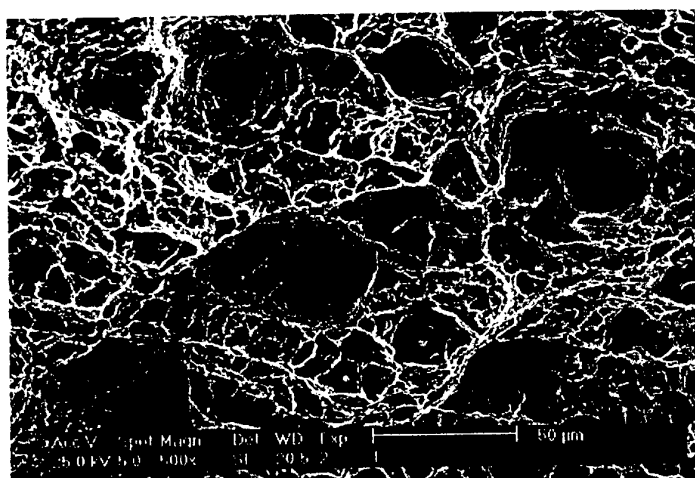


Figure 3.7.4a - Detail A1- microvoids coalescence (500X) in the inner region

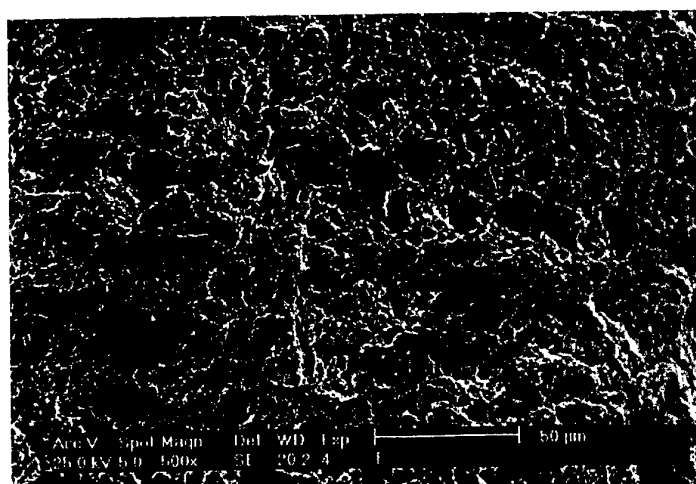


Figure 3.7.4b - Detail A2- smaller nucleated microvoids in the outer region, same scale as above picture (500X)

The analysis of fracture surfaces reveals that microvoid growth process is the key mechanism of failure. The comparison for the same notched geometry tested at different load rates does not reveal large differences in the average microvoid size both in the inner and outer region of the minimum section. Here, microcavities have a large size and higher density in the inner region where failure starts. Going out from the center of the specimen the average population of microvoids decrease in size and density. Few isolated large voids nucleated at larger inclusions can still be found close to the border that separates the shear failure area from the inner one.

On the contrary, the comparison of different notched geometry shows different microvoid sizes and densities. For $R=1.25$ mm, i.e. high stress triaxiality localized in the very inner region of the section, few governing voids of huge size are found. Here, the density of void population is not very dense. Specimens with larger notch and weaker stress triaxiality at the center show a larger number of microcavities of smaller size but more densely packed. This confirms the critical role played by stress triaxiality in the ductile failure mechanism with respect to the strain rate.

The effective stress triaxiality that is generated in the minimum section, due to a circumferential notch, can be estimated using the Bridgman solution. However, Bonora *et al.* (1998) proved that the Bridgman solution, that is derived under the assumption of perfectly plastic material, can largely differ from the effective stress triaxiality. Detailed finite element simulations proved a dependence of stress triaxiality on the hardening exponent, i.e. a material influence. In figure 3.7.5 the stress triaxiality profile along the minimum section for the four notches investigated here is given together with the reference Bridgman solution.

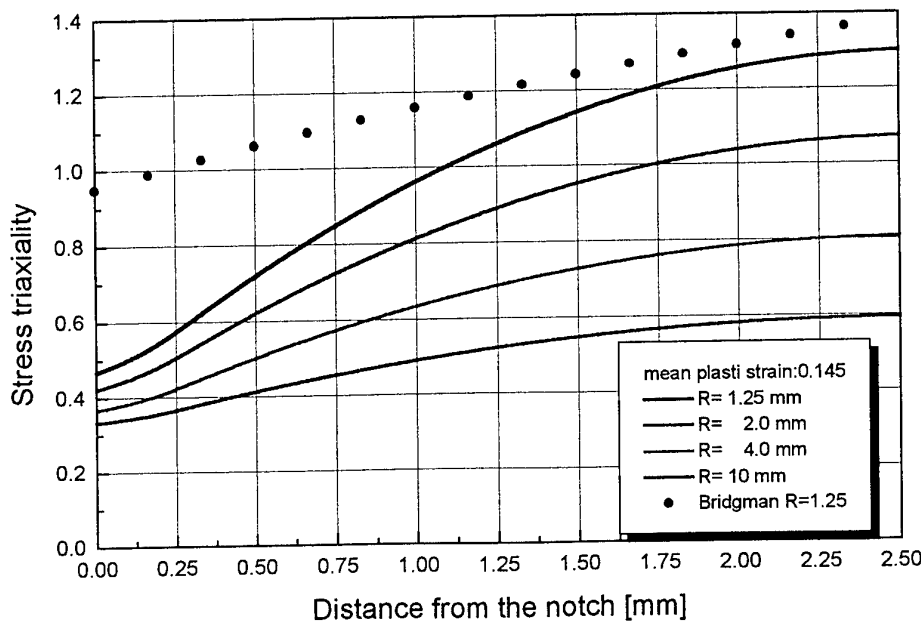


Figure 3.7.5 – Stress triaxiality along the minimum section in RNB(T): finite element results and Bridgman solution

Here finite element simulations have been performed using axialsymmetric elements, finite plasticity and updated lagrangian approach together with a plastic flow curve as experimentally identified in the previous experiments on RB(T).

Each fem model has been calibrated comparing the applied load vs diameter reduction response with the experimental data available. Strain rate effect has been also incorporated in order to predict specimen response under different load rate conditions. To this purpose, a generalized Johnson and Cook curve modified plastic flow curve has been used as indicated in section 3.5.

Once, the models have been calibrated, they have been used to determine the stress triaxiality at fracture and the corresponding equivalent strain at the center of the specimen entering in the curves with the measure of the diameter reduction at fracture. It is worth to underline that in this case, even though for the R=1.25 mm, the measure of the strain to failure is pretty close to the one obtained with the Bridgman solution. Thus, it has been possible to build the stress triaxiality versus ductility diagram, as reported in figure 3.7.6. Here, the CDM-model prediction is also given showing a very good agreement with the experimental data.

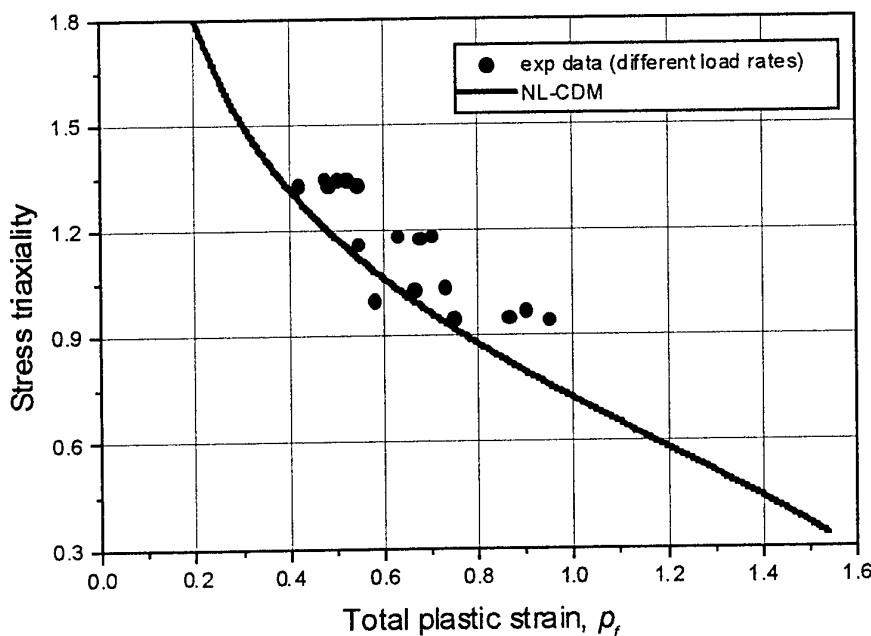


Figure 3.7.6 – Triaxiality-ductility diagram for SA537 steel.

4.0 SOLID STATE EQUATION

4.1 Background

It is now well recognized that metals with a body-centered cubic (BCC) lattice, like α -iron, ferritic steels, niobium, tantalum etc., have a mechanical behavior strongly dependent on the temperature T and the strain rate $\dot{\varepsilon}$.

This, in general, is not observed in metals having a face-centered cubic (FCC) structure, like austenitic steels, aluminum, copper, silver, etc., in particular as far as temperature is concerned, which does not seem to have the same pronounced effect on the yield strength, at least below the creep regime.

Between the two, there are metals with a closely-packed hexagonal lattice (HCP), like titanium and zinc, that show a dependence of the yield strength on temperature and strain rate, but less pronounced than in BCC materials.

It is rather difficult to describe the plastic behavior of all metals through a generalized process that leads to a unified theory. Many attempts have been made in the past to establish what is known as the mechanical equation of the solid state that, like the gas state where pressure and volume are linked with temperature, relates the yield strength σ_y to the temperature T and the strain rate $\dot{\varepsilon}$:

$$\sigma_y = f(\varepsilon, \dot{\varepsilon}, T) \quad (4.1)$$

Zener and Hollomon (1944), Manjoine (1944), Cottrell (1948, '49, '53, '57 and '58), Hollomon (1947), Yokobori (1953), Orowan (1954), Seeger (1954 and 1955), Campbell (1953, 1959), Conrad (1960, 1961), Conrad et al. (1962), Petch (1953, 1957 and 1964) and others, have tried to derive that equation through an empirical or physical approach, based on experiments, or a theoretical one based on either the activation energy concept or dislocation models.

More recently, Johnson and Cook (1983), Johnson et al. (1983), Klopp et al. (1985), Hoge and Mukherjee (1977), Zerilli-Armstrong (1987, 1990 and 1992), Follansbee (1986), Follansbee and Kocks (1988) and Nemat-Nasser et al. (1998a, 1996, 1998b) have addressed the issue and developed empirical or physically-based constitutive equations. Often, the solid state or constitutive equations proposed were not consistent at all, but in general, it has been found an exponential dependence of the yield strength σ_y on temperature and an equivalence between temperature and strain rate. This latter aspect, in particular, is well shown by the Zener and Hollomon equation:

$$\sigma_y = f(\dot{\varepsilon} \cdot e^{Q/RT}) \quad (4.2)$$

where Q is the so-called activation energy and R the universal gas constant.

The purpose of this part of the research is to present a new mechanical equation of the solid state (Milella 1998) that describes by a single equation the plastic behavior of materials as a function of strain rate and temperature. Its thermal component is based on dislocations behavior and, in particular, on the concept of Cottrell's atmosphere that surrounds each dislocation, supported by the granite solidity of experimental evidences obtained on a wide variety of steels and metals having different microstructure and strengths. Its strain rate component, instead, is derived from the characteristic trend of the material response at constant $\dot{\epsilon}$ and variable temperature, observed for the first time by Milella.

4.2 The Effect of Temperature

It must be explicitly said that the temperature field considered in this analysis is that below the creep range. To deform a metal beyond the elastic limit or yield strength σ_y , means to activate and move its dislocations through the crystal. Dislocations encounter obstacles as they move through the lattice. Some of these, also called long-range obstacles, are due to the structure of the material and cannot be overcome introducing thermal energy into the crystal. Therefore they contribute to the yield strength with a component that is non-thermally activated. Others, on the contrary, can be overcome by thermal energy.

These last are normally called short-range barriers. We can, therefore, consider the yield strength of a material σ_y as been made of two components, one athermal σ_{lr} (long-range component) and the other σ_{sr} (short-range component) thermally activated:

$$\sigma_y = \sigma_{lr}(\text{structure}) + \sigma_{sr}(T, \dot{\epsilon}) \quad (4.3)$$

It is worth noting that the thermal component σ_{sr} in eq. (3) has been written as a function of both temperature T and strain rate $\dot{\epsilon}$, since, as it will be described later, the strain rate has a direct effect on the yield strength and it can reduce the actual capability of temperature to provide thermal energy to overcome short range barriers.

The most important short-range obstacle is the so-called Peierls-Nabarro barrier. Effectively, Zerilli and Armstrong (1987, 1992) observing the different behavior with temperature shown by BCC and FCC metals, where the BCC structure has a much higher sensitivity to temperature, concluded that overcoming the Peierls-Nabarro barriers was the main thermal activation mechanism for BCC metals. Figure 4.2.1 is a simple sketch of a Peierls-Nabarro barrier.

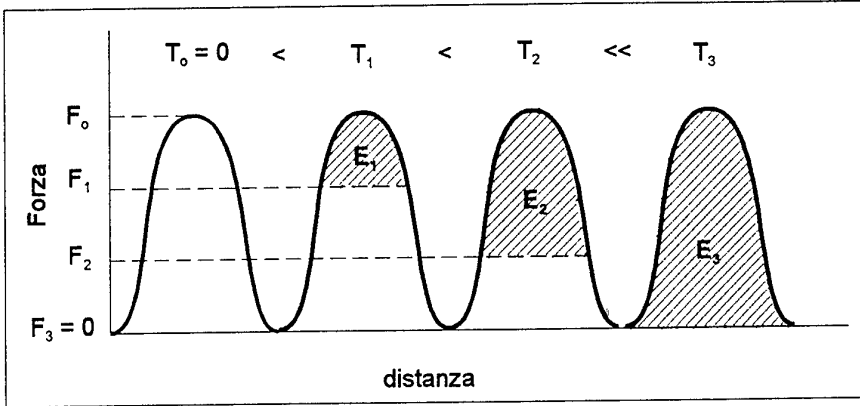


Figure 4.2.1 – Schematic of a Peierls-Nabarro barrier and the relative force F_i that must be applied at different temperatures T_i to move dislocations.

The effect of temperature is also shown in Figure 4.2.1. By increasing the temperature, $T_3 \gg T_2 > T_1$, we introduce into the system more and more thermal energy, $E_3 \gg E_2 > E_1$, that fills the barrier, whose effective height is reduced and, therefore, the relative force F_i to overcome the barrier and move dislocations is also reduced. Using a statistical mechanics approach, we can say that at equilibrium the probability P to get a thermal fluctuation whose amplitude is greater than E is given by:

$$P = \exp\left(-\frac{E}{kT}\right) \quad (4.4)$$

where k is the Boltzmann's constant. Eq. (4.4) leads to a yield strength, σ_{sr} , exponential dependence on temperature, as described by eq. (4.2). Though interesting, the approach does not provide any physical interpretation of the barrier, whose nature remains generic. We shall, than, follow a different approach.

The starting point will be the difference in mechanical behavior shown by BCC metals and alloys with respect to FCC ones. As already said, BCC materials present a yield strength that has a component thermally activated, while FCC ones do not. This difference can be ascribed to the size of dislocations, i.e., to the distance over which the additional plane of atoms deforms the lattice in which it is inserted like a wedge. In this distorted area of the crystal, interstitial atoms, always present in solid solution, like carbon, nitrogen and oxygen, migrate under the wedging pressure exerted by the dislocation.

In particular, these atoms will move from the compression side, directly above the dislocation line where the crystal shrinks, to the traction one below the edge, where the lattice is expanded and the tensile stress *attracts* them, creating what is known as the *Cottrell's atmosphere*. Wide dislocations have diluted atmospheres, since the specific distortion (distortion per unit length) of the lattice is negligible, with weak strain and stress fields attracting interstitial atoms.

On the contrary, narrow dislocations, where the *disturb* to the lattice is very localized and the stress field is intense, are characterized by atmospheres of high concentration, well over that of the solid solution that surrounds them, especially at lower temperatures. To plastically deform a metal, i.e., to pass its yield point, dislocations must be displaced across the lattice and by doing so, also their atmosphere of interstitial atoms shall be moved. This cloud of atoms, that has to follow each dislocation, will not move freely. As a result, a drag-force is generated that opposes the motion.

We can say that the higher the concentration of the Cottrell's atmosphere, with respect to that of the lattice in which it has to move, the greater this force and, therefore, the larger the component of the yield strength produced by that effect. We can envisage a variation of the concentration of the Cottrell's atmosphere with the size of the dislocations that characterize a particular metal or alloy. The drag force will change accordingly, and therefore also its effect on the yield strength. FCC metals have wide dislocations and their atmospheres are, therefore, diluted with a marginal effect on the yield stress. At variance, BCC crystals have narrow dislocations with concentrated atmospheres that oppose their motion, resulting in a sharp yield point. Figure 4.2.2 is a schematic of narrow and large dislocation, respectively. An increase of temperature will introduce new energy into the system that will allow a certain migration of interstitial atoms from the atmosphere, where they are kept together, towards the lattice. This will determine a dilution of its concentration.

At the same time, some precipitates, in particular carbides, will release their non-metal atoms that will enter into solid solution, since temperature enhances solubility of interstitial atoms, so that the lattice concentration will increase. The overall effect will be a net reduction in the unbalance between the Cottrell's atmosphere and the solid solution concentration. This will result in a reduction of the drag-stress that will favor the displacement of dislocations under the action of shear stresses and, therefore, will produce a decrease of the yield strength. By further increasing the temperature the two concentrations come closer and closer, lowering more and more the thermally activated component of the yield strength and, eventually, at a sufficiently high temperature, they will become almost equal.

At this time, we can say that dislocation atmospheres no longer exist. Now, dislocations will not distinguish any more between atoms internal and external to the atmosphere, and will move in the lattice exchanging continuously their interstitial atoms with those of the lattice. At this point, the thermal component σ_s of the yield strength is vanished. Now, moving dislocations will encounter only long range barriers due to the structure of the material, that cannot be overcome by thermal energy and represent the non-thermally activated component of the yield strength.

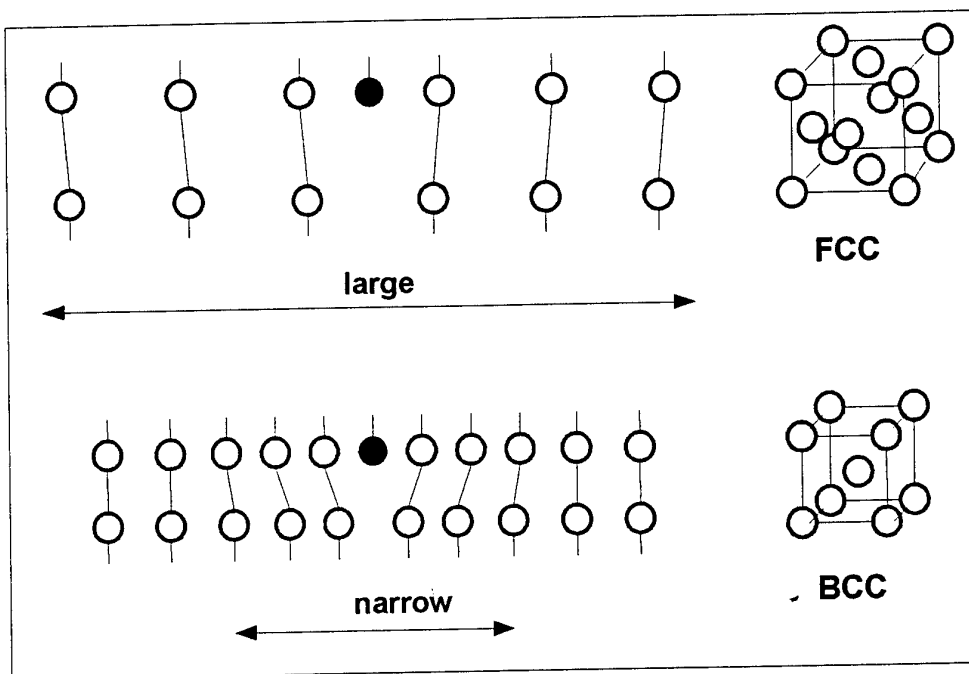


Figure 4.2.2 – Schematic of a large dislocation, typical of BCC lattice, and a narrow one, typical of FCC crystals.

The opposite will happen if temperature is reduced. In this case, there will be a massive precipitation of interstitial atoms, again mainly in the form of carbides, that will abandon the lattice diluting the solid solution. Some of them will also re-flourish the atmospheres that may not suffer any loss of atoms, since these are *frozen* in their position.

This process will enhance the difference between the two concentrations and, therefore, will augment both the force anchoring dislocations and the yield strength. This component of the yield strength that is thermally activated is not present, as experience shows, in FCC structures probably because, as said, the Cottrell's atmosphere is already diluted at any temperature at a value that approaches that of the solid solution.

We can say that, in general, the more those two concentrations differ the higher the resulting drag stress and, therefore, the component σ_{sr} . To visualize the effect of temperature just mentioned, it can be useful to look at the carbon solubility in the lattice. Carbon certainly provides the most abundant source of foreign atoms that enter into solid solution and is characterized by a great mobility. Carbon solubility in ferrite can be expressed by the following relation (Wert, 1950):

$$C(\%) = 2.55 \cdot e^{-9700/RT} \quad (4.5)$$

where $C(\%)$ is the concentration in percent in weight of carbon, R the universal gas constant, equal to 2 cal/mole K, and T the temperature, in degree Kelvin.

At the eutectoid temperature, ~ 723 °C, the carbon concentration resulting from eq. (5) is about 0.02 %. Already at ambient temperature (RT) it becomes $2 \cdot 10^{-7}$. This means that by lowering the temperature of about 700 °C, from 723 °C to RT , the Cottrell's atmosphere will face an environment where the concentration of interstitial carbon atoms declined by a factor 10^5 .

This is a tremendous reduction that will be felt by the material through a sharp increase of the yield strength. Because of the exponential nature of eq. (4.5), a further decrease of temperature, this time of only 125 °C, from RT to -100 °C, will result in an even greater reduction of concentration by a factor 10^6 , approximately.

In this second temperature drop, we shall then expect an even larger increase of the yield strength, as experience is actually indicating. We will associate, then, the variation, $d\sigma_y$, of the yield strength from its current value σ_y , to the corresponding variation $d\lambda$ of the ratio of the concentration of the Cottrell's atmosphere n_c , to that n_s of the solid solution, relative to its current value $\lambda(T)=n_c/n_s$:

$$\frac{d\sigma_y}{\sigma_y} = \frac{d\lambda}{\lambda(T)} \quad (4.6)$$

We can express the global concentration n_s of all foreign atoms, carbon, nitrogen, oxygen etc., in solid solution in a form like that of eq. (5), relative only to carbon:

$$n_s = a \cdot e^{-\frac{b}{RT}} \quad (4.7)$$

where a and b are material characteristics. Also the concentration $n_c > n_s$ of the Cottrell's atmosphere will be expressed in the same fashion:

$$n_c = c \cdot e^{\frac{d}{RT}} \quad (4.8)$$

with c and d material characteristics. This time, the exponent is positive, since it is supposed, at the moment, that the concentration of the Cottrell's atmosphere decreases with temperature. The ratio $\lambda(n)$ will then become:

$$\lambda(T) = \frac{n_c}{n_s} = f \cdot e^{\frac{g}{RT}} \quad (4.9)$$

with $f=c/a$ and $g=b+d$. Integrating eq. (4.6) between a reference temperatures T_0 and T :

$$\int_{T_0}^T \frac{d\sigma_y}{\sigma_y} = \int_{T_0}^T \frac{d\lambda}{\lambda} \quad (4.10)$$

yields:

$$\begin{aligned}
 \ln \sigma_y(T_0) - \ln \sigma_y(T) &= \ln \lambda(T_0) - \ln \lambda(T); \\
 \ln \sigma_y(T_0) - \ln \sigma_y(T) &= \frac{g}{RT_0} - \frac{g}{RT}; \\
 \ln \sigma_y(T) &= \frac{g}{RT} + \ln \sigma_y(T_0) - \frac{g}{RT_0}
 \end{aligned} \tag{4.11}$$

The last of eqs. (11) can be written as:

$$\ln \sigma_y(T) = \frac{B}{T} + A \tag{4.12}$$

with A and B constants characteristic of the material:

$$A = \left[\ln \sigma_y(T_0) - \frac{g}{RT_0} \right]; \quad B = \frac{g}{R} \tag{4.13}$$

that, as we will see, can be easily determined experimentally. Eq. (4.12) provides the base for the definition of the mechanical equation of the solid state. In its explicit form it relates the yield strength to the temperature:

$$\sigma_y(T) = C \cdot e^{\frac{B}{T}} \tag{4.14}$$

where:

$$C = e^A = \sigma_y(T_0) \cdot e^{-\frac{g}{RT_0}} \tag{4.15}$$

It is worth noting the similarity between eq. (4.14) derived from a dislocation model and eq. (4.2) based on the activation energy.

4.3 Experimental Results

In a \ln versus $1/T$ space, eq. (4.12) represents a straight line, whose angular coefficient is B , and A the known term. Figure 4.3.1 shows the experimental results, open and closed points, of traction tests obtained on eleven steels, having different microstructure and yield strengths σ_y , tested at various temperatures.

The steels considered are: 18 Ni with σ_y equal to 1750 and 1260 MPa at RT, respectively, 10NiCrMo, HY 130 and 80, A 517, NiMoV, A 533 B, A 508 Cl3, A 302 B and SAE 1020. Also shown in the figure, solid lines, are the corresponding general trends that are non-linear with temperature. Figure 4.3.2 presents the same data of

Figure 4.3.1 plotted in a \ln versus $1/T$ space. Two peculiar features emerge from Figure 4.3.2.

First, the best fit experimental trend, solid lines, follows effectively the linear behavior predicted by eq. (4.12); second, the various steels can be grouped into three main *families* namely very high, medium-high and medium-low resistance.

Each *family* shows a characteristic slope B , higher for low strength steels and lower for the high strength ones. In a medium-low resistance steel, like A 533 B, there is a larger dependence of the yield strength σ_y on temperature than in a high strength one, like 18 Ni steel.

Decreasing the temperature, mild steels become more and more resistant. Eventually, at very low temperature, around or below -200 °C, mild steels can reach the same strength of martensitic and even maraging steels. The linear dependence of σ_y on $1/T$, in a \ln versus $1/T$ space, means that the constants C and B in eq. (14), that are material characteristics, can be determined graphically. Constant A is simply the intersection with the y axis of the linear fit of the experimental results, while B is, as said, the slope of the line.

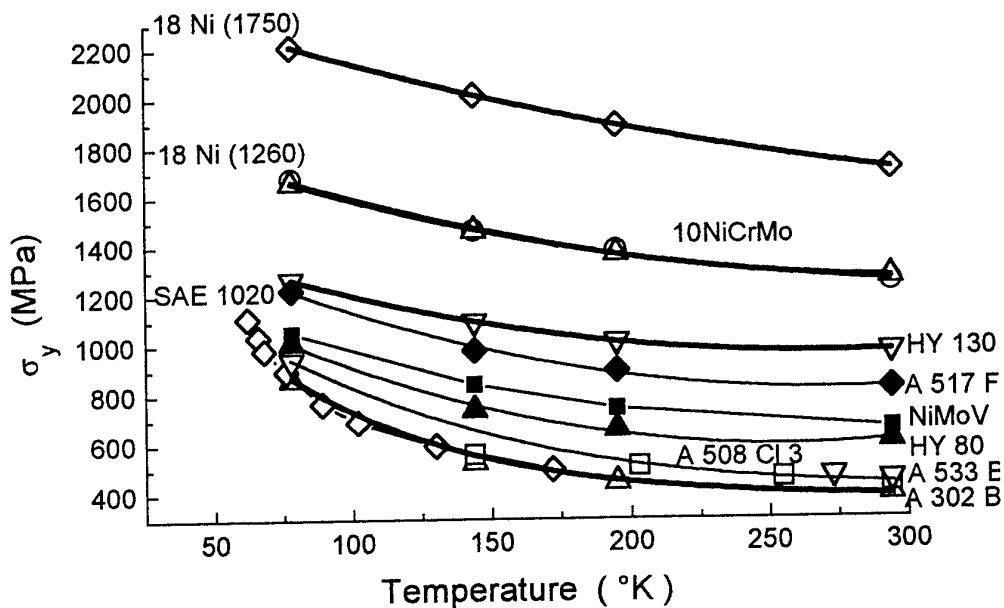


Figure 4.3.1 - Experimental results, solid and open symbols, of the yield strength σ_y for eleven different steels and their trend, solid lines, with temperature T .

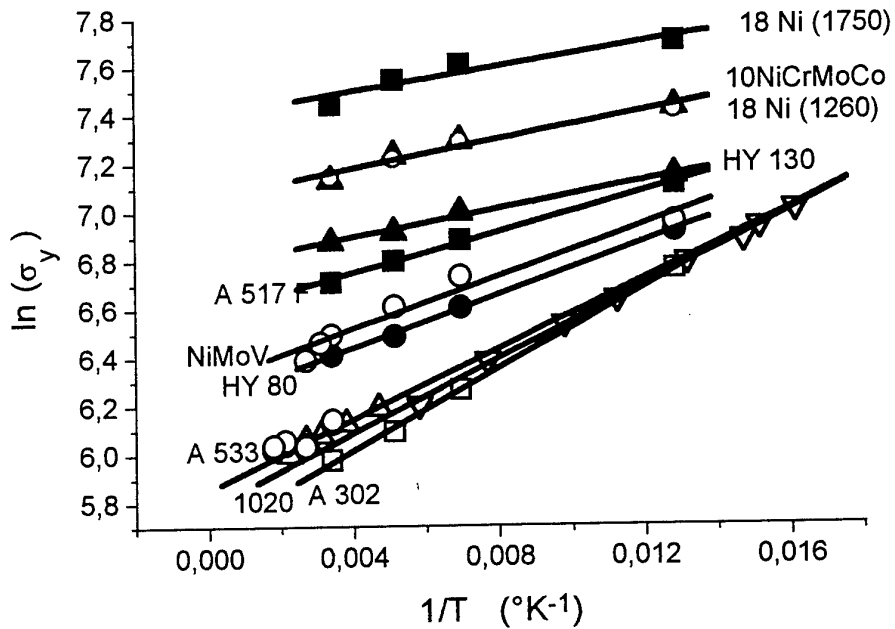


Figure 4.3.2 - Experimental results of σ_y , solid and open points, and their trend, solid lines, in a \ln vs $1/T$ dyagram for the steels considered in figure 4.3.1.

4.4 Low Strain Rate Behavior

Once the fundamental relation between yield strength and temperature is established, eq. (4.12) and eq. (4.14), we shall try to asses the effect of the strain rate $\dot{\varepsilon}$ on the response of the material and how this effect depends on temperature.

We start to analyze the low strain rate range, i.e., $\dot{\varepsilon} \leq 10^3 \text{ s}^{-1}$. To this purpose, we will consider, as first, a particular steel: A 533 B, used in the nuclear industry for pressure vessels, having a BCC lattice. Its chemical composition is listed in table I.

The trend of the yield strength with temperature is shown in figure 4.3.1. The mechanical properties of this steel have long been measured at different temperatures and strain rates making it be one of the most suitable for strain rate effects investigations. The present study is based on data obtained by Kanninen et al. (1987).

Table I Chemical composition (% in weight) of carbon steel A 533 B

C	Mn	P	S	Si	Ni	Mo
0.19	1.28	0.012	0.013	0.21	0.64	0.55

Five temperatures were selected, namely -60, -10, 50, 100 and 175 °C, and at each of them four different strain rates were applied, namely 10^{-3} , 0.1, 1.0 and 530-570 s^{-1} . Table II lists the experimental results.

*Table II Yield strength σ_y measured on A 533 B steel
at various temperatures and strain rates*

Temp. (°C)	Strain rate (s^{-1})	Yield (MPa)	Temp. (°C)	Strain rate (s^{-1})	Yield (MPa)
-60	0.001	486	100	0.001	429
-60	0.1	542	100	0.1	444
-60	1.0	590	100	1.0	455
-60	531	689	100	556	483
-10	0.001	459	175	0.001	403
-10	0.1	490	175	0.1	420
-10	1.0	511	175	1.0	443
-10	537	569	175	574	455
50	0.001	438			
50	0.1	476			
50	1.0	484			
50	542	517			

For each strain rate $\dot{\varepsilon}$, the value of the corresponding yield strength σ_y , measured at each of the test temperature, has been plotted in a \ln versus $1/T$ diagram.

The results are presented in figure 4.4.1, solid points, together with the corresponding best fit lines. It can be seen that the linear trend predicted by eq. (4.12) and shown in Figure 4.3.2, is kept at all the strain rates considered, from the quasi-static application of the load, $\dot{\varepsilon}=10^{-3} s^{-1}$, to the dynamic ones.

Even more interesting is the finding that the slope of the various lines, though varying with $\dot{\varepsilon}$, is such that all of them point back to the same intersection with the y axis that, as said, provides the value of the constant A .

Then, A is an invariant, i.e., independent of the strain rate $\dot{\varepsilon}$, and can be considered as a characteristic of the material. For the steel considered, the A 533 B, this intersection yields 5.9 and, therefore, the value of the constant C in eq. (4.15) is:

$$C = e^A = 365 \text{ MPa} \quad (4.16)$$

This finding, that all lines merge to the same point, means that the effect of strain rate is less and less pronounced as the temperature increases.

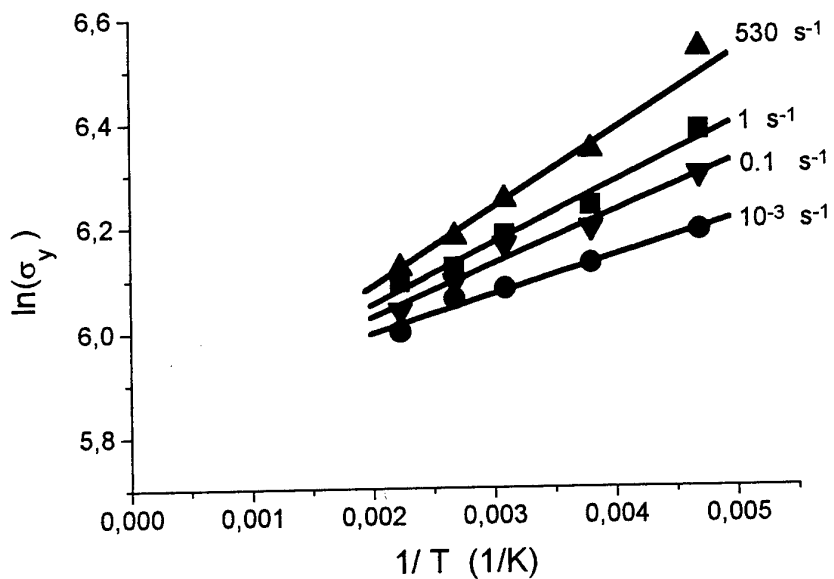


Figure 4.4.1 – Trend of $\ln\sigma_y$ versus $1/T$ in A 533 B steel, for four different strain rates $\dot{\varepsilon}$.

While at low temperatures there is a remarkable difference in the material response at various strain rates $\dot{\varepsilon}$, at the higher ones this difference shrinks, as if temperature would wash out the strain rate effect.

This finding poses a serious question on the long asserted equivalence between temperature and strain rate. It must be noted that the actual point of convergence of all the straight lines, that yields the value of the constant A , is not precisely at the intersection with the y axis, i.e., $1/T = 0$, but is located at a very low temperature, $T \sim 910^\circ\text{C}$ or $1/T \sim 8.4 \cdot 10^{-4}$.

This finding, as we shall see, is of great importance, besides that it alleviates the sufferance of dealing with an infinite value of temperature. A new testing program was run on a second steel: A508BC13. This is quite similar to A533B, besides it is used for forging applications. Two strain rate were selected, namely 0.0001 s^{-1} , representative of a quasi-static condition, and 600 s^{-1} . The results are shown in figure 4.4.2.

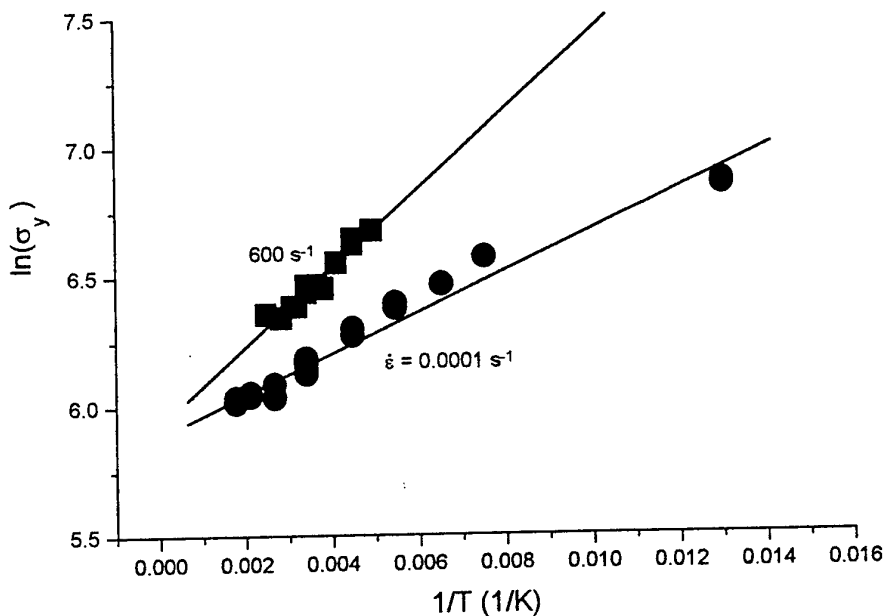


Figure 4.4.2 – Trend of $\ln(\sigma_y)$ vs $1/T$ for carbon steel type A508BCI3 at two different strain rates.

Again, it can be seen the linear trend at both strain rates and the merging toward a common point at $\ln(\sigma_y) \approx 5.9$. The same trend has been seen on a completely different BCC metal: niobium. The metal was tested at -73°C , -23°C and room temperature at three different, very low strain rates: 0.00016 s^{-1} , 0.0016 s^{-1} and 0.008 s^{-1} , respectively. The results are shown in figure 4.4.3.

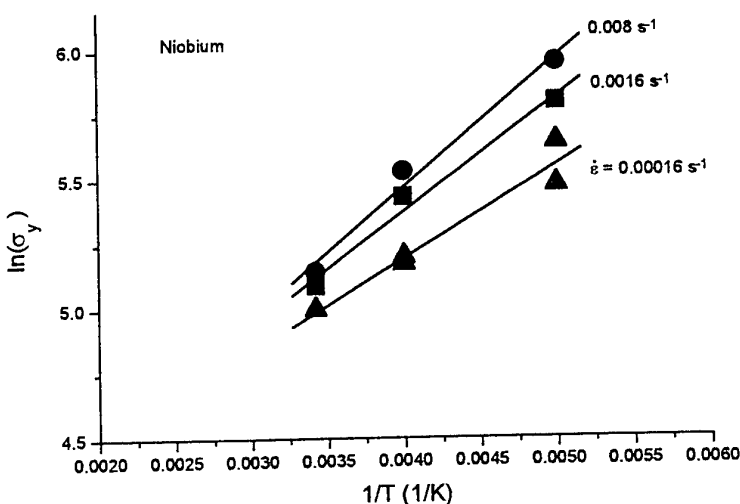


Figure 4.4.3 - Trend of $\ln(\sigma_y)$ vs $1/T$ for niobium tested at three different strain rates.

4.5 The Mechanical Equation of Solid State

The linear nature of the $\ln\sigma_y$ versus $1/T$ at all the strain rate $\dot{\varepsilon}$ considered, leads to another important consideration. Let's plot the slopes B of the four straight lines of Figure 4.4.1 versus the natural logarithm of the strain rate, $\ln\dot{\varepsilon}$, which they refer to. This can be seen in figure 4.5.1. The surprising result is another straight line whose equation is:

$$B = 119 + 7.2 \cdot \ln\dot{\varepsilon} \quad (4.17)$$

This means that the parameter B in eq. (4.12) is not a constant, but depends on the strain rate $\dot{\varepsilon}$ in a linear fashion with respect to its natural logarithm, $\ln\dot{\varepsilon}$, expressed by eq. (4.17). We can, then, substitute in eq. (4.12) the parameter B with its expression given by eq. (4.17) and get:

$$\sigma_y = 365 \cdot (e^{119/T} \cdot \dot{\varepsilon}^{7.2/T}) \quad (4.18)$$

in which the constant C was given the previously found value of 365 MPa, see eq. (4.16). Eq. (4.18) represents the mechanical equation of the solid state for the steel considered: A 533 B.

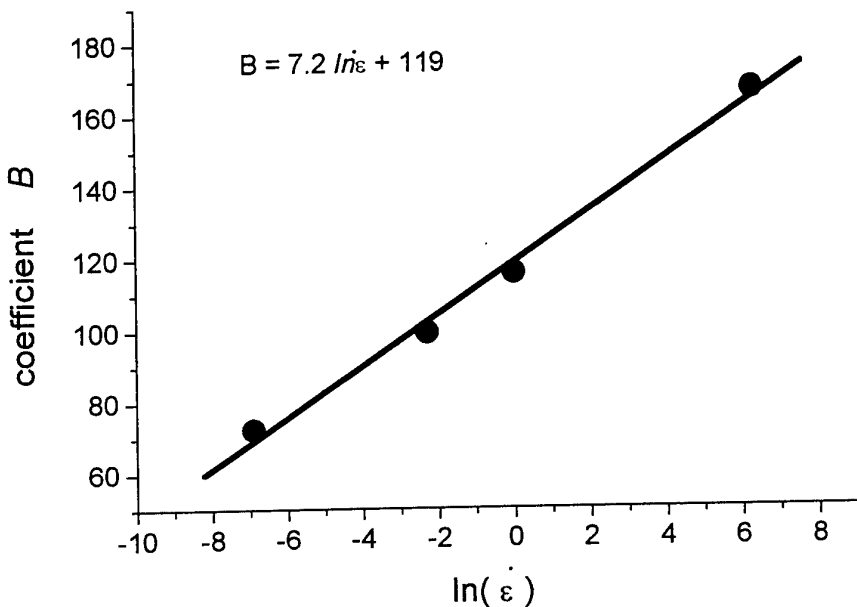


Figure 4.5.1 – Trend of the slopes B of the four straight lines of Figure 4.2.5 versus $\ln\dot{\varepsilon}$.

The same linear trend can be observed on niobium, as shown in figure 4.5.2 whose equation is:

$$B = 38.66 \cdot \ln(\dot{\varepsilon}) + 688.58 \quad (4.19)$$

Therefore the mechanical equation of the solid state for niobium is:

$$\sigma_y = 37 \cdot \left(e^{689/T} \cdot \dot{\varepsilon}^{39/T} \right) \quad (4.20)$$

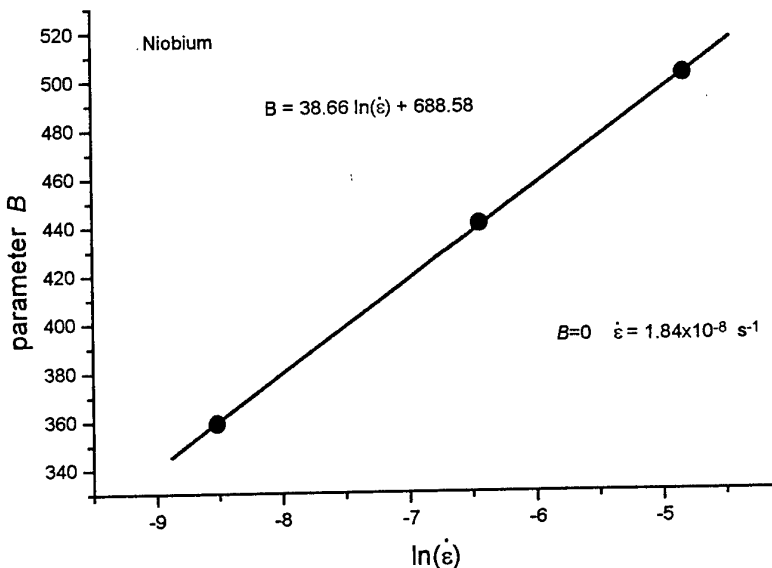


Figure 4.5.2 – Trend of the slopes B of the three straight lines of Figure 4.2.7 versus $\ln \dot{\varepsilon}$.

For a generic BCC metal, for which the parameter B will take the most general form:

$$B = D + E \cdot \ln \dot{\varepsilon} \quad (4.21)$$

eq. 4.18 will be written as:

$$\sigma_y = C \cdot \left(e^{D/T} \cdot \dot{\varepsilon}^{E/T} \right) \quad (4.22)$$

with C, D and E to be determined experimentally with the same procedure.

4.6 The Drag-Stress of Atmospheres on Moving Dislocations

The constant C in eq. (4.22) has the dimensions of a stress. For the steel considered in this study, A 533 B, its value is about 365 MPa (see eq. 4.18). The value of this stress,

that we'll call *reference stress*, derives from the intersection with the y axis (or close to it) shared by all the straight lines shown in Figure 4.4.1, whose slope is related to the strain rate $\dot{\varepsilon}$. This means that the same intersection must pertain also to the line with zero slope, i.e., the horizontal one that refers to the case where the yield strength σ_y is independent of temperature. Therefore, the constant C physically represents the component of the yield strength that is not thermally activated, σ_{tr} in eq. 4.3. This finding does not come unexpected.

The thermal component of the yield strength, based as said on the drag-stress exerted by the Cottrell's atmosphere, is in fact a function of the dislocation velocity (Cottrell and Jaswon 1949). At very, very low velocities the associated drag-stress has to be very, very small, almost negligible, because it is given enough time to interstitial atoms to realign and follow the dislocation motion.

This means that at a sufficiently small strain rate, which results in a very slow dislocation velocity, the thermally activated stress component shall disappear. Let's try to infer the value of this limiting strain rate at which the yield strength will lose its dependence on temperature. If we express all the experimental results, σ_y , obtained at all temperatures and strain rates, listed in Table II, as function of the parameter in brackets in eq. (4.18), that we will call P :

$$P = e^{119/T} \cdot \dot{\varepsilon}^{7.2/T} \quad (4.23)$$

we get the plot of figure 4.6.1. The data are well aligned along a straight line whose equation is:

$$\sigma_y = 266 \cdot P + 98 \quad (4.24)$$

The cited reference stress, $\sigma_y=365$ MPa, corresponds to $P=1$. When P is equal to one, its value becomes independent of temperature and the corresponding strain rate is: $\dot{\varepsilon}=6.6 \cdot 10^{-8} \text{ s}^{-1}$. A strain rate $\dot{\varepsilon}$ equal to $\sim 7 \cdot 10^{-8} \text{ s}^{-1}$ can be effectively considered very, very small, since at that rate it will require about eight hours just to initiate a macroscopic plastic deformation ($\varepsilon \sim 0.002$).

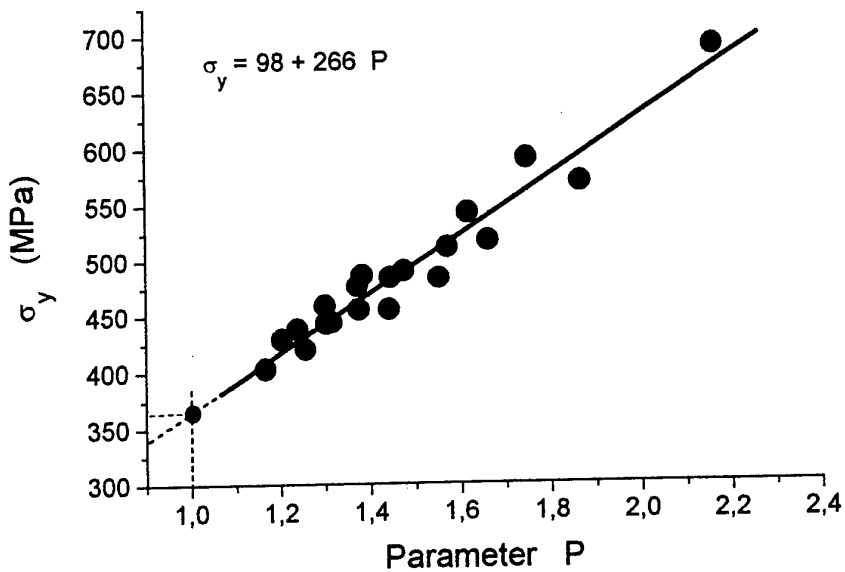


Figure 4.6.1 – Trend of experimental yield strength σ_y of A 533 B steel vs the parameter P .

In a plot $\ln \sigma_y$ versus $1/T$, like that of Figure 4.4.1, this temperature independent component will appear, as said, as a zero slope, flat line pointing towards the 5.9 value on the y axis, as shown in figure 4.6.2.

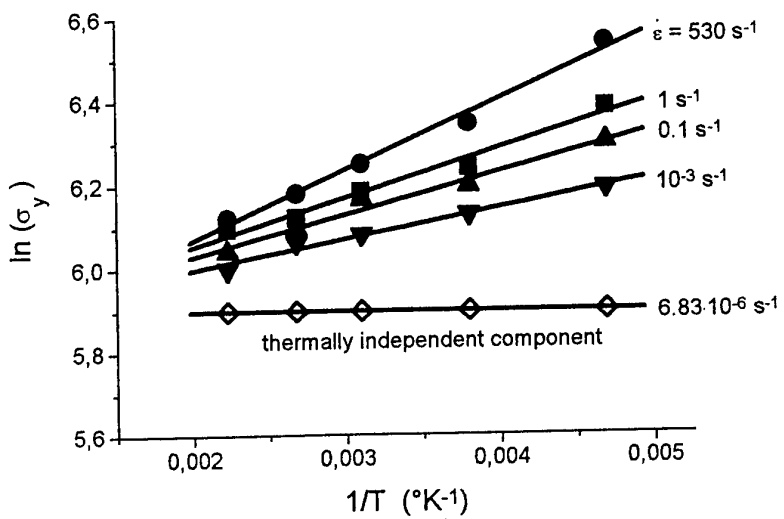


Figure 4.6.2 – Visualization of the thermally independent component of the yield stress.

This zero slope, $B=0$, is a point of the line shown in Figure 4.5.2. From its equation we can also derive that the strain rate $\dot{\varepsilon}_0$ at which $B=0$, is precisely $6.6 \cdot 10^{-8} \text{ s}^{-1}$. Looking at niobium, Figure 4.4.3, we derive that this limiting strain rate at which the yield strength is independent of temperature, $B = 0$, is $\dot{\varepsilon}_0 = 1.8 \cdot 10^{-8} \text{ s}^{-1}$, i.e., the same order of magnitude as for A533B steel.

4.7 EXPERIMENTAL PROGRAM

In order to further verify and support the findings previously outlined that have led to the formulation of the mechanical equation of the solid state (MESS), an experimental program has been performed on A 537 Cl1, aluminum killed steel. Table 4.7.1 shows the chemical composition of the steel used.

Table 4.7.1 Chemical composition of A 537 Cl1 steel

C	Mn	Si	P	S	V	Nb	Al	N
0.19	1.45	0.38	0.013	0.005	0.05	0.033	0.025	0.012

Twelve tests have been run at three different temperatures and four strain rates. The temperatures selected were 300°C , RT and -100°C , respectively. The four strain rates ranged from 10^{-3} s^{-1} to 10^3 s^{-1} . In the low strain rate range, the testing was run using a load cell of 20 KN and small specimens of 3 mm diameter, shown in figure 4.7.1. For the medium range it has been used a hydro-pneumatic device shown in figure 4.7.2. It consists of a pressure cylinder divided in two sections by a piston free to move. The piston acts as a load cell. The upper section is filled by water, the lower by gas, initially at the same pressure. By opening an electro-valve the pressure in the water chambre drops to zero while the opposite chambre is connected to a high pressure gas tank. This force the piston to move at high speed under the driving force exerted by the pressure difference. The machine capacity is 50 KN, the maximum stroke is 10 mm. The strain rate achievable ranges from 10^{-1} to 50 s^{-1} . A typical test record is shown in figure 4.7.3. Finally, a Hopkinson bar has been used to run the tests at 10^3 s^{-1} . The test apparatus is schematically shown in figure 4.7.4. A typical test record obtained with the Hopkinson bar is presented in figure 4.7.5. Figures 4.7.6 to 4.7.8 summarize the test results obtained on A 537 Cl1 at 300 , 20 and -100°C and 10^{-3} , 25 - 30 , 400 and 10^3 s^{-1} , respectively. The values of the lower yield stresses measured in the experimental test program have been analyzed according to the procedures outlined in section 4.4. Figure 4.7.9 shows the results obtained. As it can be seen, the trend of $\ln \sigma_y$ vs $1/T$ is always linear at all the strain rates considered and all the best fit lines merge towards a common value that is ~ 5.5 . This means that the value of the constant C in eq. 4.22 is 245. This, as previously explained, is the value of the athermal component of the yield strength, σ_{yr} . The slope of the four straight lines of fig. 4.7.9 have been plotted versus $\ln \dot{\varepsilon}$. The result is shown in figure 4.7.8. The equation of the line of fig. 4.7.10 is:

$$B = 153.23 + 8.33 \cdot \ln \dot{\varepsilon} \quad (4.25)$$

and provides the values of the parameters D and E in eq. 4.21. Therefore, the solid state equation for A 537 Cl1 is:

$$\sigma_y = 245 \cdot (e^{153/T} \cdot \dot{\varepsilon}^{8.33/T}) \quad (4.26)$$

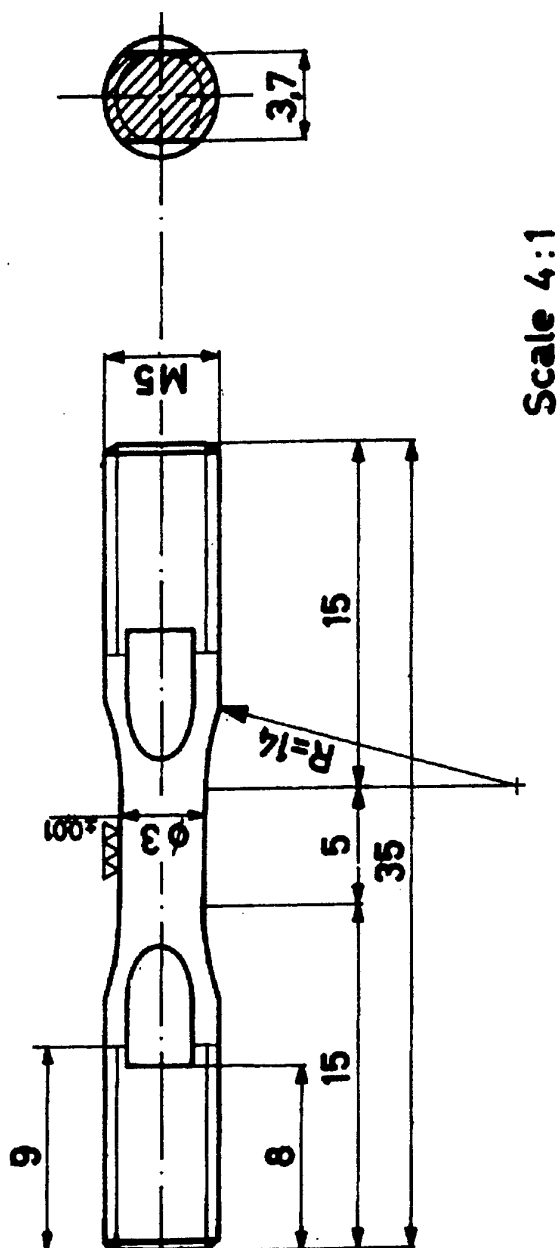


Fig. 4.7.1 – Specimen used in the dynamic test program

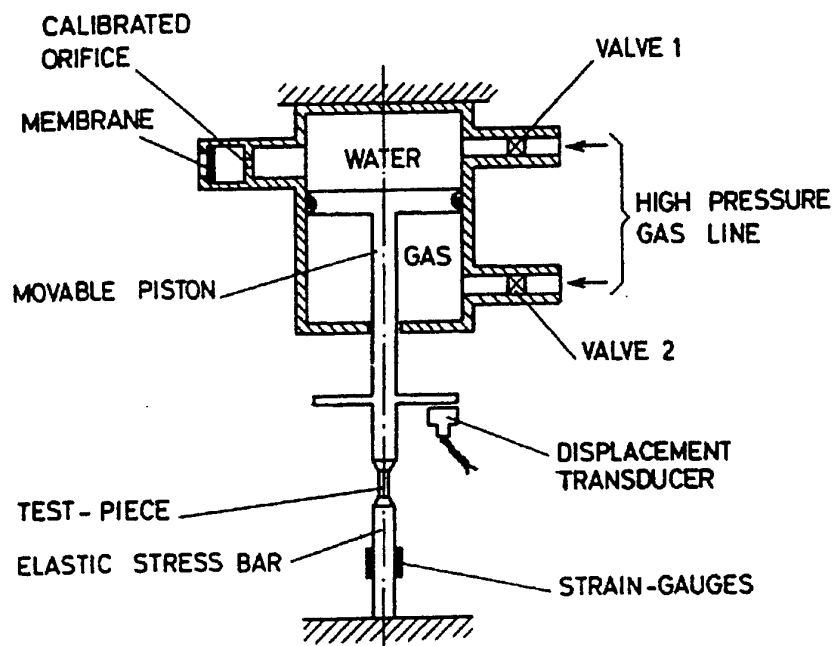


Fig. 4.7.2 – Schematic of the hydro-pneumatic test device for medium range strain rate testing.

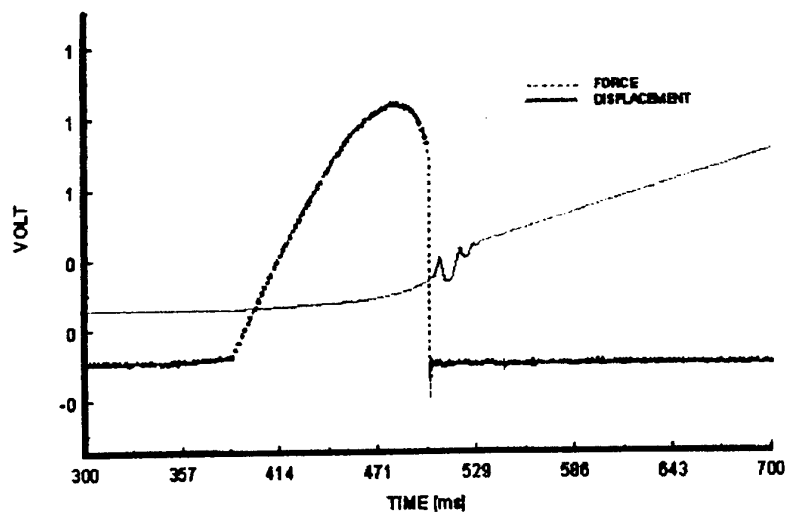


Fig. 4.7.3 – Typical test record obtained with a hydro-pneumatic test machine.

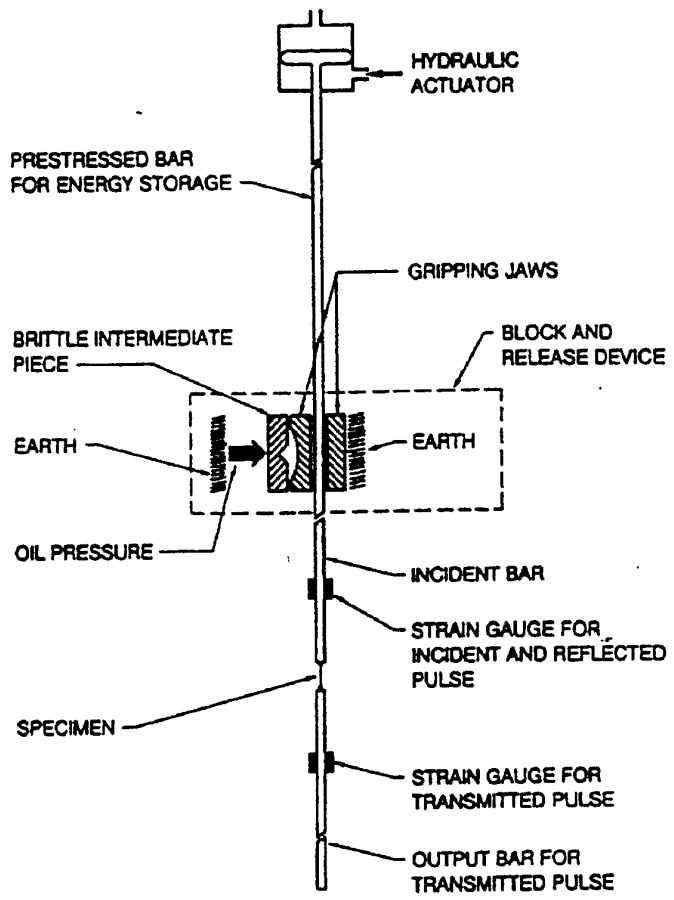


Fig. 4.7.4 – Schematic of a Hopkinson bar for high strain rate test s.

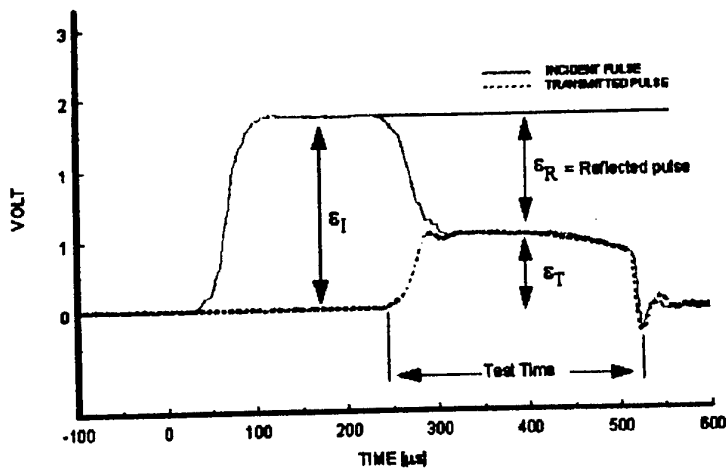


Fig. 4.7.5 – Typical test record obtained with a Hopkinson bar device.

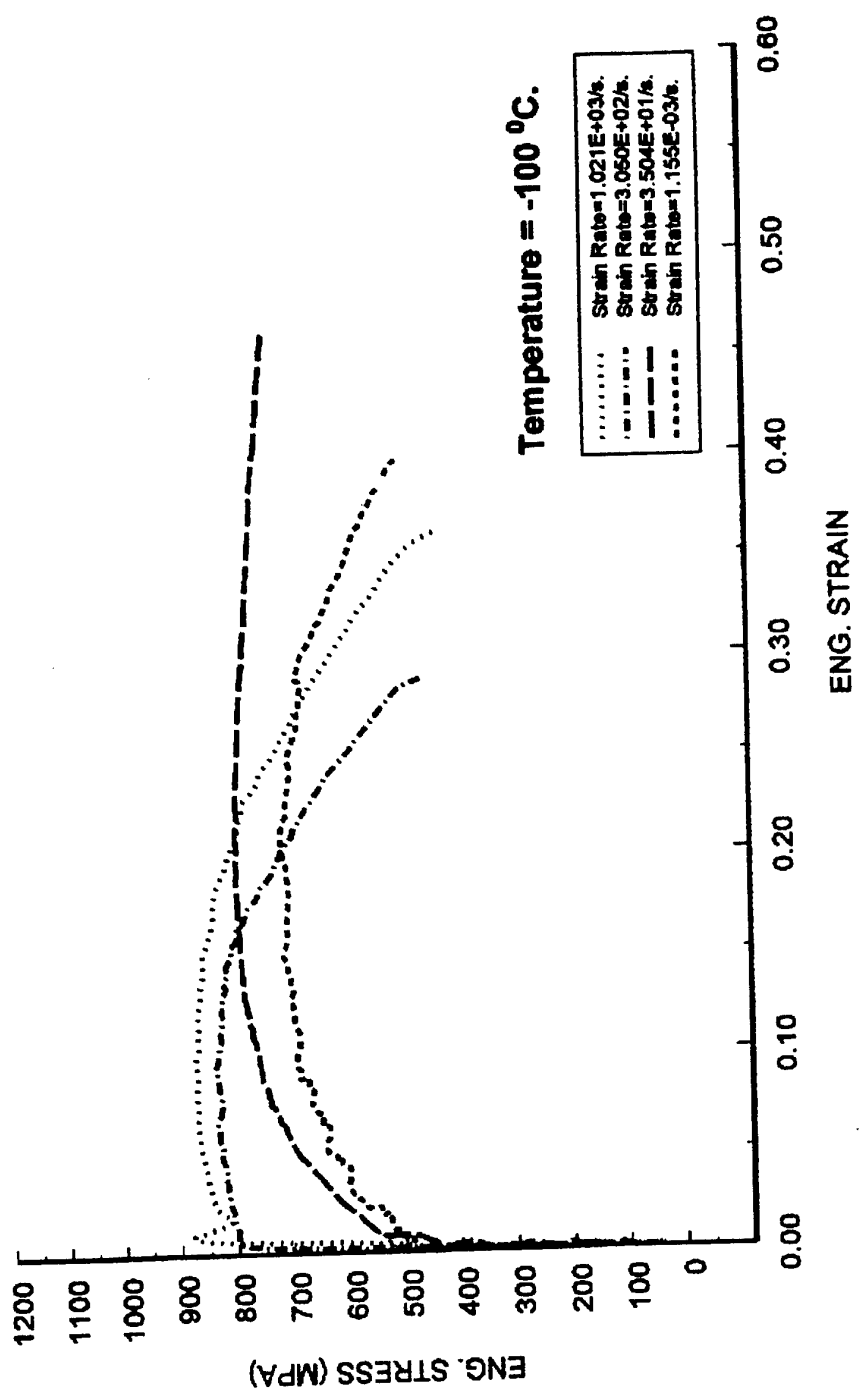


Fig. 4.7.6 – Test results at -100°C .

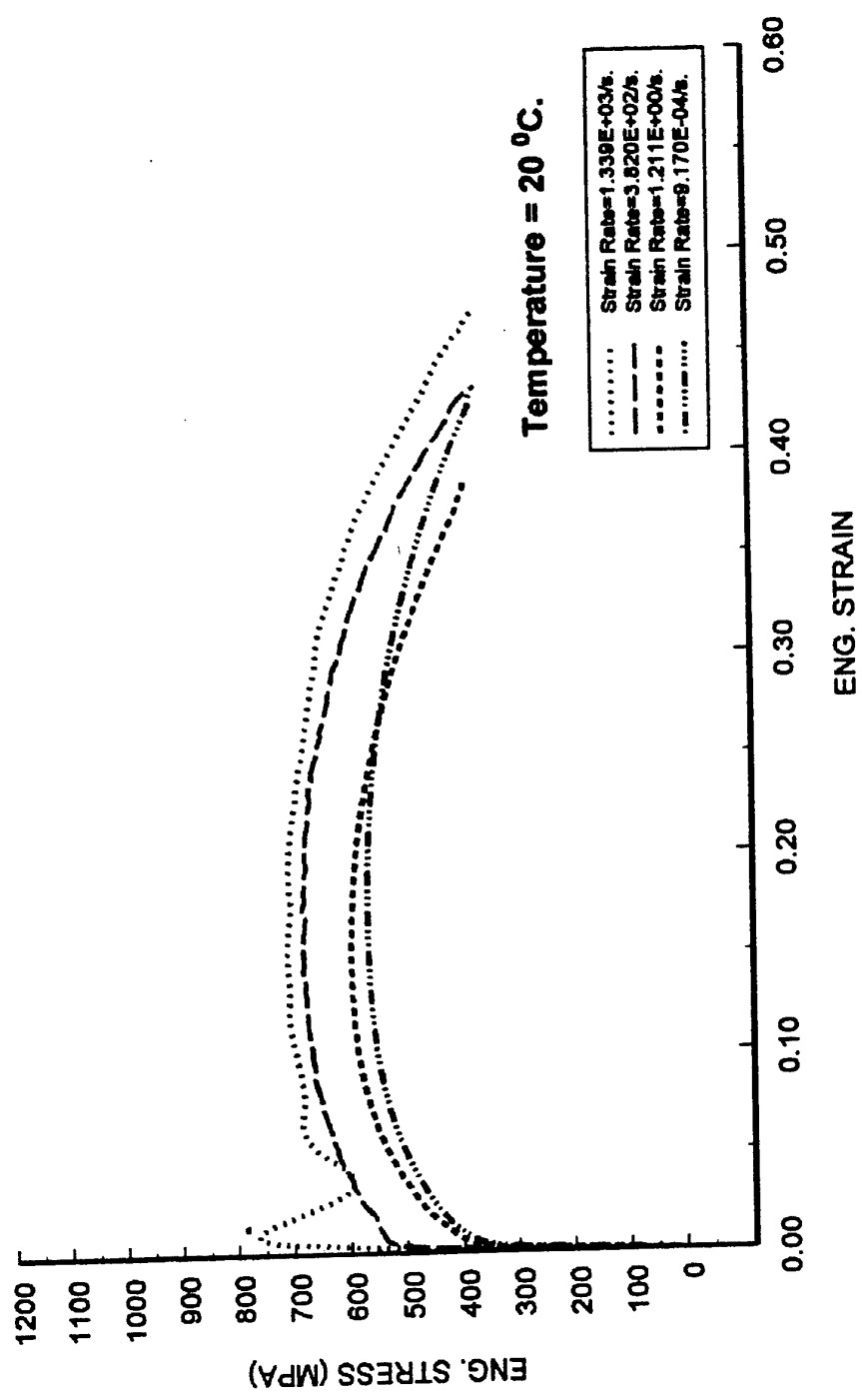


Fig. 4.7.7 – Test results at room temperature.

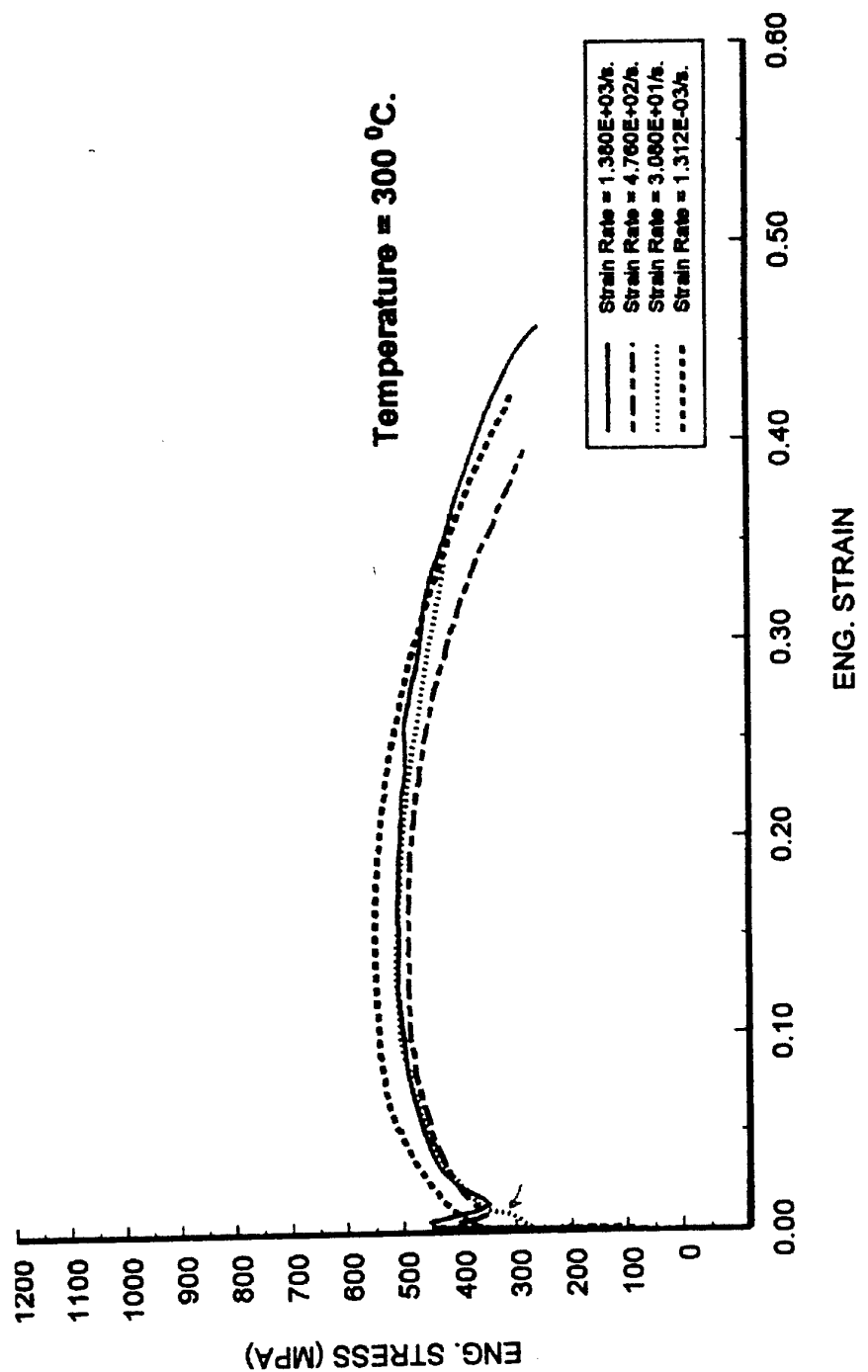


Fig. 4.7.8 – Test results at 300 °C.

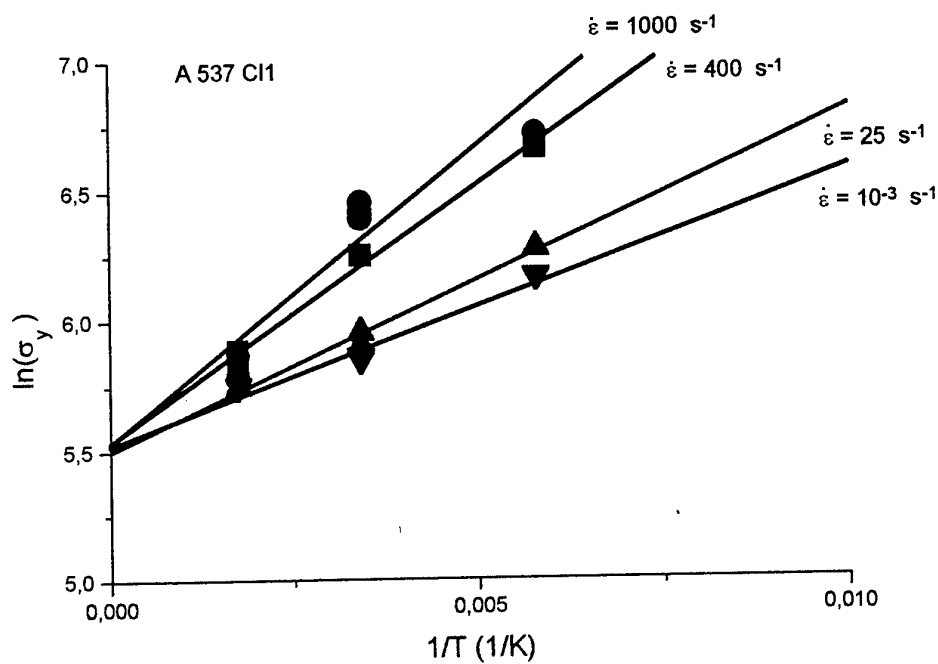


Fig. 4.7.9 – Trend of $\ln\sigma_y$ versus $1/T$ in A 537 Cl1 steel, for four different strain rates $\dot{\varepsilon}$.

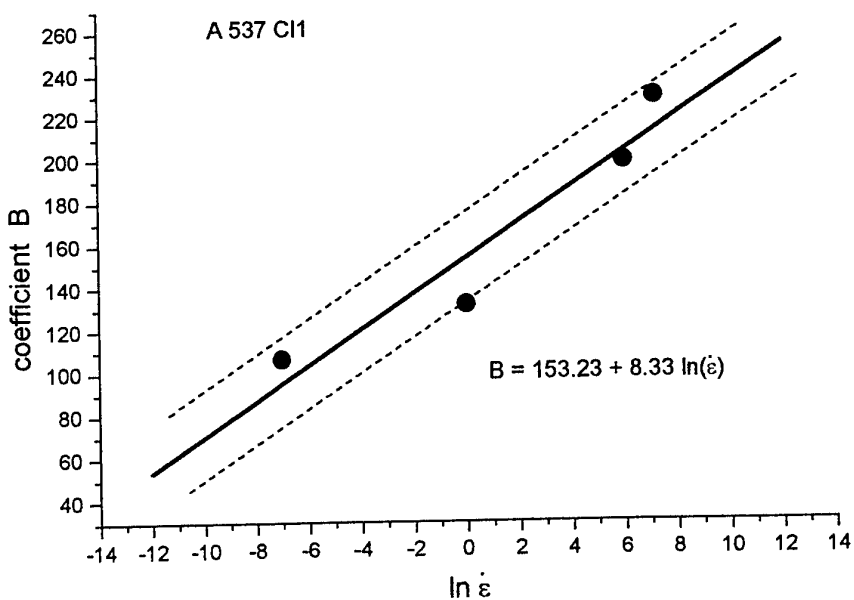


Fig. 4.7.10 – Trend of the slopes B of the four straight lines of fig. 4.7.9 versus $\ln\dot{\varepsilon}$.

4.8 High Strain Rate Behavior

The previous considerations, though interesting, yet leave elements of uncertainty. At both very low and very high dislocation velocities, the drag-stress exerted by its atmosphere has to be very small.

At extremely high velocities an atmosphere of solute atoms should not exist any more, eliminating the drag force that is temperature dependent. Moreover, it can be shown, by simple considerations, that the thermal energy fluctuation E used to overcome an obstacle (see eq. 4.4) is no longer available, no matter what the temperature is, at extremely high dislocation velocities.

These facts, lead to the conclusion that at very, very high strain rates, resulting in very high dislocation velocity, only a thermal independent component of the yield strength must exist that appears as a flat, horizontal line in a $\ln(\sigma_y)$ versus $1/T$ space, like the bottom horizontal line of Figure 4.6.2, but at the top of the diagram, corresponding to a very high stress level.

At the same time, by increasing the strain rate beyond a certain value, the trend shown in figures 4.4.1, 4.4.2 and 4.4.3 must reverse. Now the lines, if they still remain straight, must converge toward a common upper value that represents precisely that upper athermal component of the yield strength, as schematically shown in figure 4.8.1. There will be a transition strain rate value $\dot{\varepsilon}_{tr}$ between the two behavior, that will result in a transition line pointing at the same time toward the lower and upper merging point (points A and B of Figure 4.8.1). To verify this fact, new strain rate ranges $\dot{\varepsilon}$ were investigated for the steels considered in this analysis, namely A533B and A508BCI3. Twelve specimens of A508BCI3 were prepared

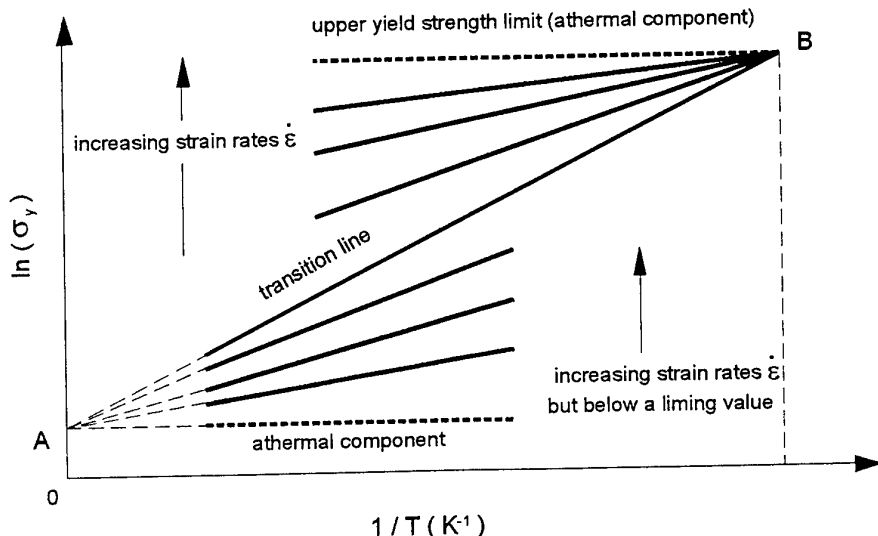


Figure 4.8.1 – By increasing the strain rate $\dot{\varepsilon}$ over a certain value, the slope of the lines does not increase any longer, but starts to decrease. A new upper merging point B appears which corresponds to the upper athermal component of the yield strength.

and tested at $\sim 1800 \text{ s}^{-1}$ at ten different temperatures, namely $-70, -50, -30, -10, 0, 20, 40, 50, 80$ and 130°C . The results are shown in figure 4.8.2, together with the previously found ones obtained at 0.0001 and 600 s^{-1} , already shown in Figure 4.4.2.

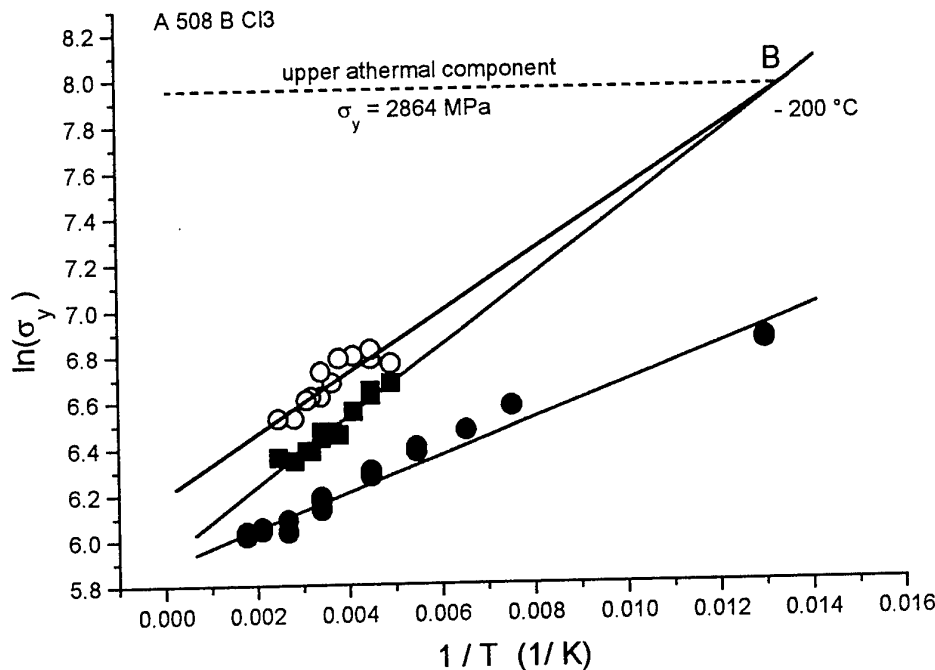


Figure 4.8.2 – By increasing the strain rate at $\sim 1800 \text{ s}^{-1}$ the trend remains linear, but the slope decreases and a new point of convergence B is reached at about -200°C . Effectively, the trend remains linear and the slope decreases. A new point of convergence B is reached at about -200°C .

According to the considerations previously done, this point shall represent the upper limit of the yield strength that is thermally independent. Its value is about 2860 MPa. Same results were found for the A 533BC13 steel, that was tested at 5000 and 900 s^{-1} . The results are shown in figure 4.8.3.

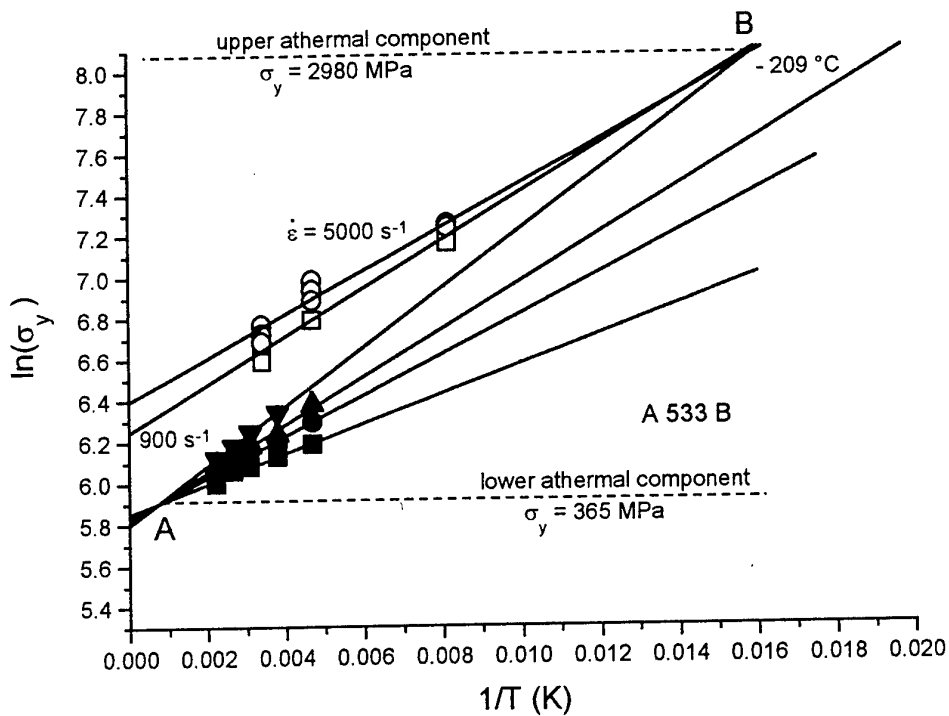


Figure 4.8.3 – Experimental results obtained on A 533 B steel tested at 5000 and 900 s^{-1} .

In this upper part of the diagram, i.e., for strain rates $\geq 900 s^{-1}$, a new equation of the solid state can be written:

$$\sigma_y = C_1 \left(e^{b/T} \cdot \frac{\dot{\varepsilon}^{a/T}}{\dot{\varepsilon}^{a/T_{max}}} \right) \quad (4.27)$$

where C_1 , a and b are material characteristics and T_{max} is the temperature at which the lines converge (point B). The factor C_1 represent, in practice, the upper limit of the yield strength, i.e., the upper athermal component (see Figure 4.8.3).

The finding that at high strain rates, above $10^3 s^{-1}$, the trend of the experimental results changes, when plotted in a $\ln(\sigma_y)$ versus $1/T$ diagram, as schematized in fig. 4.8.1 and shown in figures 4.8.2 and 4.8.3, merging towards a new common point B makes we think that the deformation mechanism may no longer be based on the dislocation motion, but on a different one such as, for instance, twinning. If this is the case, than a HPC metal, in which twinning is the dominant mechanism of deformation, shall experience this different behavior already at low strain rates. To this purpose, a titanium alloy has been considered. The testing temperatures and strain rates are listed in table 4.8.1. The results are shown in figure 4.8.4.

Table 4.8.1 Temperature T and strain rates $\dot{\epsilon}$ for the titanium alloy

Strain rate $\dot{\epsilon}$ (s^{-1})	Temperature (°C)				
	400	200	20	-98	-196
10^{-4}	400	200	20	-98	-196
10^{-2}	400	200	20	-98	-196
1.5	400	200	20	-98	-196
45	400	200	20	-98	-196

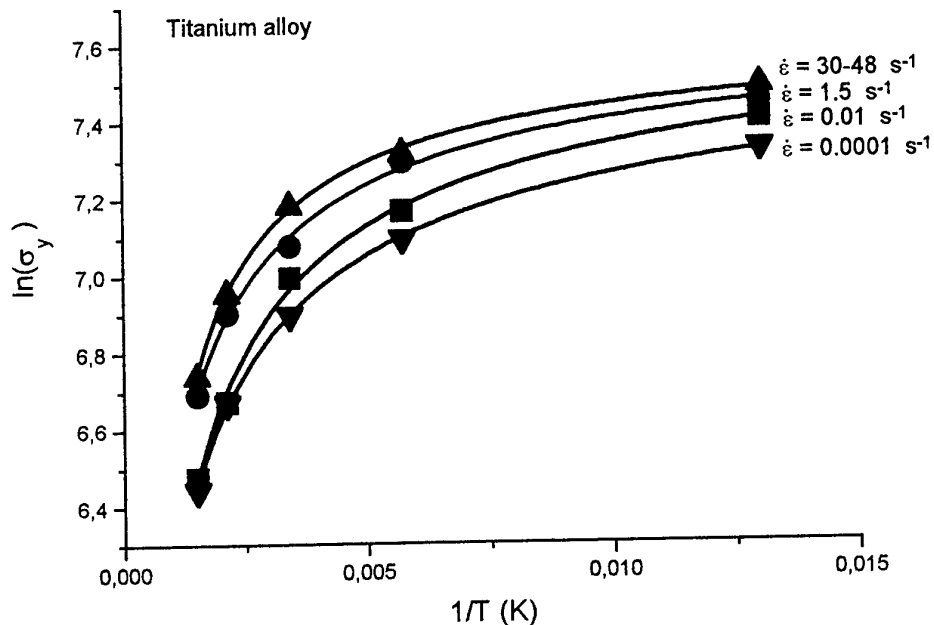


Fig. 4.8.4 – Trend of $\ln\sigma_y$ vs $1/T$ for a titanium alloy at different strain rates $\dot{\epsilon}$.

It is clear that the linear trend is lost and that the material behavior at constant strain rate seems to converge towards a common upper point at very low temperature (~ -250 °C) for all strain rates. This finding may confirm that the solid state equation previously found is typical of BCC lattice materials. The results shown in fig. 4.8.4 are of great importance. They evidence the missing ring of fig. 4.8.1 and 4.8.2 where both high and low strain rate trends appear to start from a common point (points A and B) and continue to run without any end. This seems not to be possible since at very high temperature (very low $1/T$ values) any high strain rate behavior must show a sudden drop toward zero, as shown in fig. 4.8.4 for the titanium alloy. We shall also expect that a similar trend be seen at low strain rates and very low temperatures, but this time the merging point will be the upper limit represented by point B. Therefore we shall expect that the actual strain rate profiles, also for BCC lattice materials, are of the type depicted in figure 4.8.5.

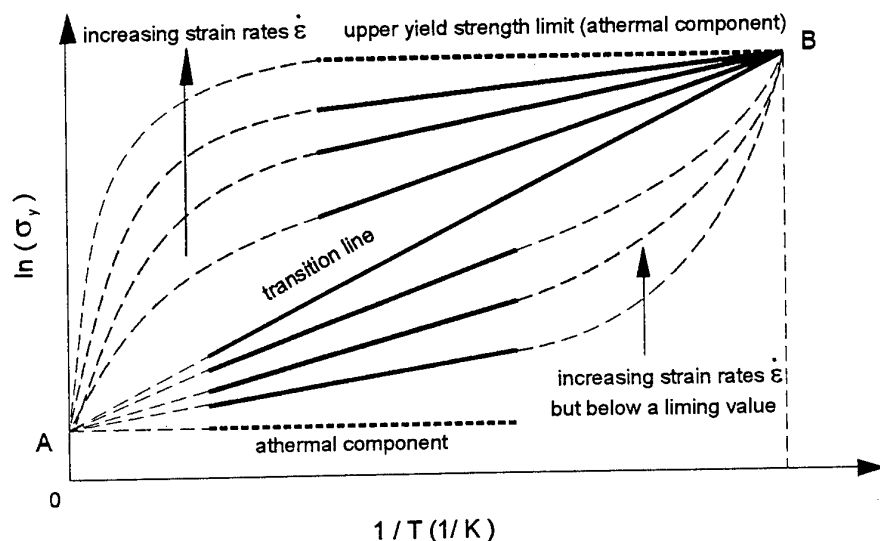


Fig. 4.8.5 – Expected behavior of BCC materials at very high and very low temperatures (dashed lines).

If this is the case, then eq. 4.22 and 4.27 are still valid, but will describe the material behavior in the domain represented by the solid lines in fig. 4.8.5, respectively.

5.0 UNIFIED MODEL

The two models summarized in the previous sections take into account of strain rate, temperature and ductile damage, separately. Since they both resulted successful in predicting the evolution of the yield strength and damage for a wide class of metals and loading conditions, can be used in a unified framework.

The model proposed by Milella gives the evolution of the yield strength as a function of the strain rate and temperature, pointing out for the first time a dependence of the strain rate effects on the temperature itself. The modification of the entire plastic flow curve is not addressed in the model. However, it is possible to assume that the entire plastic flow curve is scaled with respect to the actual yield strength value similarly to the Johnson and Cook (1983) model. Thus, assuming a Ramberg-Osgood power law plastic behavior, it is possible to write:

$$\sigma(\varepsilon_p, T, \dot{\varepsilon}) = \sigma_y(T, \dot{\varepsilon}) \left[1 + \frac{K}{\sigma_y(T, \dot{\varepsilon})} \varepsilon_p^n \right] \quad (5.1)$$

where n is the hardening exponent and K the hardening slope. If compared to the model proposed by Milella, strain rate effect predicted with the Johnson and Cook model leads to very close results as shown in Figure 5.1 where the yield strength predicted by the two models is given for a wide strain rate range. In Figure 5.2 the comparison between the predicted flow curves is given for a strain rate of 1000 sec⁻¹ and two temperature, 25°C and 200°C, respectively. In figure 6 the J&C parameters have been calibrated matching the yield strength at low strain rate (i.e., 10E-04 sec⁻¹ and RT) while the Milella parameters come from experimental data fit.

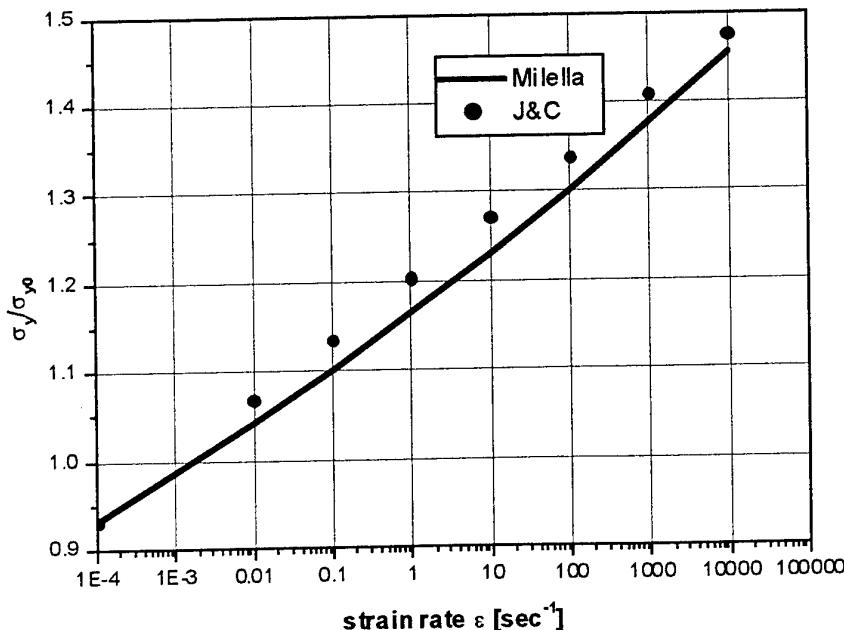


Figure 5 – Yield strength evolution for a A533B steel with strain rate: comparison between Milella and Johnson and Cook models.

CDM damage model, and porosity based damage models as well, do not incorporate effect related to strain rates or temperature. Ping (1994) theoretically analyzed the modification resulting from dynamic loading onto the growth rate of cavities in a ductile matrix including inertial effect, but without the support of experimental evidences.

Experimental observations confirm that under ductile failure conditions the micro-mechanism of failure is always given by the formation and growth of microcavities no matter what both the temperature and the strain rate are. This means that no additional damage dissipation processes are introduced as a result of strain rate or temperature effect, thus damage formulation should not explicitly depend on these variables. On the contrary, damage parameters, that represent material specific physical quantities, should show some variability in association with them.

In the model proposed by Bonora, four are the material damage parameters needed: ε_{th} , ε_f , D_{cr} and α . Since the threshold and failure strain are measure of the capability of the material to plastically deform, a variability with load rate and temperature is expected:

$$\begin{aligned}\varepsilon_{th} &= \varepsilon_{th}(\dot{\varepsilon}, T) \\ \varepsilon_f &= \varepsilon_f(\dot{\varepsilon}, T)\end{aligned}\quad (5.2)$$

Johnson et al. (1983) investigated the behavior of several classes of metals under severe load rates and temperature. They analyzed the dependence of strain to failure with $\dot{\varepsilon}$ and T. While it came out that the role played by temperature was considerable, strain rate effect resulted to be weak for all materials investigated. For instance, the increase of ductility for OFHC copper, caused by T was of the order of 112% at 50% of homologous temperature while only an increase of 20%, approximately, for a strain rate of 10000 sec^{-1} was found. The threshold strain is controlled by the nature of the bond between the included particles and the ductile matrix. Since the strain rates barely affect the strain to failure, it can be assumed that it has no effect on threshold strain as well. In steels, voids usually start after particle breaking. When temperature increases, the matrix softens and the stresses at the interface are expected to reduce resulting in an increase of the threshold strain.

The critical damage D_{cr} is related to the minimum net resisting section that can still sustain load in the reference volume element, prior failure. Once again, the experimental observations of Johnson and Cook confirm that the area at failure in specimen tested with Hopkinson bar, is scarcely sensitive to the strain rate while temperature has a higher effect. Measures on SA537 steel in the low strain rate range, as discussed in the previous sections, confirm a lacking of dynamic effect on damage parameters. From these considerations, it is possible to express the modification induced by strain rate and temperature onto damage parameters in the following form:

$$\begin{bmatrix} \tilde{\varepsilon}_{th} \\ \tilde{\varepsilon}_f \\ \tilde{D}_{cr} \end{bmatrix} = \begin{bmatrix} \varepsilon_{th} \\ \varepsilon_f \\ D_{cr} \end{bmatrix} \left(1 + \begin{bmatrix} A_0 \\ B_0 \\ C_0 \end{bmatrix} \ln \frac{\dot{\varepsilon}}{\dot{\varepsilon}_0} \right) \left(1 + \begin{bmatrix} A_1 \\ B_1 \\ C_1 \end{bmatrix} T^* \right) \quad (5.3)$$

where $A_0, A_1, B_0, B_1, C_0, C_1$ are material constants, T^* is the homologous temperature and $\dot{\varepsilon}_0$ is a reference strain rate. ε_{th} , ε_f and D_{cr} are the quasi static damage parameters at room temperature.

The constants in each set are expected to have values very close to each others (i.e, $A_0 \approx B_0 \approx C_0$). Here, the first set, that account for the strain rate effect, is globally much less than 1.0 (i.e. $A_0 \approx B_0 \approx C_0 \leq 0.002$) and in a first approximation can be neglected reducing the equation 5.4 to:

$$\begin{bmatrix} \tilde{\varepsilon}_{th} \\ \tilde{\varepsilon}_f \\ \tilde{D}_{cr} \end{bmatrix} = \begin{bmatrix} \varepsilon_{th} \\ \varepsilon_f \\ D_{cr} \end{bmatrix} (1 + \beta T^*) \quad (5.4)$$

The damage exponent α gives the shape of the damage accumulation process as a function of plastic strain. This value is identified from experimental damage measurements and possible effect resulting from strain rate and temperature should be experimentally investigated.

It has to be underlined that, at the moment, the possibility to perform damage measurements under severe strain rates is made very difficult by the necessity to run accurate strain controlled tests on which measure the progressive stiffness loss.

Finally, the model can be easily implemented in any commercial finite element code assigning a user defined plastic flow curve as a function of the two current variables T and strain rate. In theory, given $(\dot{\varepsilon}_i^t, \dot{\varepsilon}, T)$ for any gauss point of any element in the model, damage calculation requires to solve the set of equations in (5-9). Neglecting the elastic strain contribution with respect to the plastic one in both the micro and macro scale, the set of eqn. (5-9) is reduced to the integration of eqn. (9), only,

- Yield strength:**

$$\text{low strain rate range} \quad \sigma_y(\dot{\varepsilon}, T) = C \cdot (e^{D/T} \cdot \dot{\varepsilon}^{E/T}) \quad (5.5)$$

$$\text{high strain rate range } (> 10^3 \text{ sec}^{-1}) \quad \sigma_y(\dot{\varepsilon}, T) = C_1 \left(e^{b/T} \cdot \frac{\dot{\varepsilon}^{a/T}}{\dot{\varepsilon}^{a/T_{max}}} \right) \quad (5.6)$$

- Plastic flow curve:**

$$\sigma_{eq}(p, T, \dot{\varepsilon}) = \sigma_y(T, \dot{\varepsilon}) \left[1 + \frac{K}{\sigma_y(T, \dot{\varepsilon})} p^n \right] \quad (5.7)$$

- Damage law:**

$$\dot{D} = -\lambda \frac{\partial f_D}{\partial Y} = \alpha \cdot \frac{(D_{cr} - D_0)^{\frac{1}{\alpha}}}{\ln(\varepsilon_f / \varepsilon_{th})} \cdot f \left(\frac{\sigma_H}{\sigma_{eq}} \right) \cdot (D_{cr} - D)^{\frac{\alpha-1}{\alpha}} \cdot \frac{\dot{p}}{p} \quad (5.8)$$

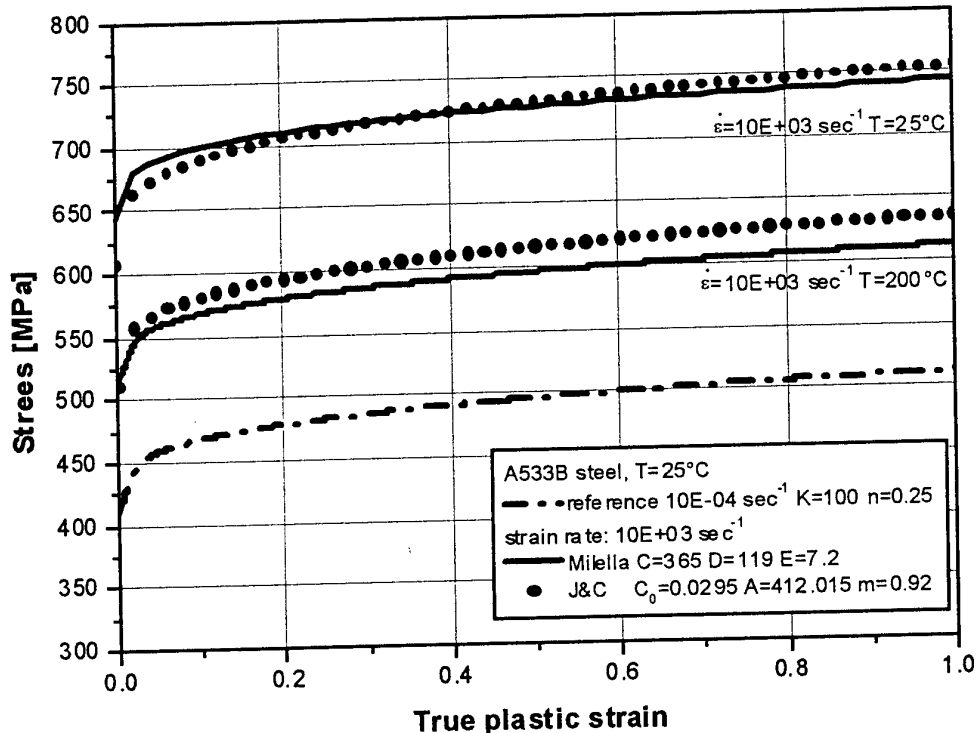


Figure 5.2 – Strain rate and temperature effect on plastic flow curve: comparison between Milella and Johnson and Cook models.

6.0 CONCLUSIONS AND RECOMMENDATION

The determination of damage parameters in the quasi-static strain range for two low alloy steels has been done. However, the integration of the experimental data with finite element simulation is needed to evaluate the influence of stress triaxiality on damage parameters. The validation of the damage model has been extended to the multi-axial state of stress conditions. Damage behavior has been monitored under dynamic conditions both in the uniaxial and multi-axial state of stress case. The major result of the experimental program confirms that, at least for the low strain rate range, the material response is sensitive to the load rate showing a clear effect on both the yield strength and the plastic flow curve. On the contrary, a similar effect is missing on damage parameters both in under uniaxial and multiaxial state of stress loading conditions.

The extensive scanning electron microscopy (SEM) of the specimens fracture surfaces confirm the key role played by the void dynamics in the ductile failure process. The comparison of the fracture surfaces for those specimens tested at low and high load rates, confirms the absence of a load rate effect on the evolution of microvoids. Both the population density and the size of the microvoids located at the center and in the

periphery of the failure surface for RNB(T) specimen are comparable for the low and high load rate case. Stress triaxiality has a more relevant effect on microvoids evolutions and this effect must be accurately accounted for in a damage model.

Based on the concept of Cottrell's *atmosphere* surrounding a dislocation and its interaction with interstitial atoms in solid solution, a mechanical equation of the solid state has been derived which relates the yield strength of a material to temperature T .

The equation is valid for BCC materials characterized by narrow dislocations having a concentration of the atmosphere well in excess with respect to that of the surrounding lattice. The dependence of σ_y on T is exponential through a constant C , see eq. 4.12, that represents the non-thermally activated component of the yield strength. The exponent B is a linear function of the natural logarithm of the applied strain rate $\dot{\varepsilon}$, see eq. 4.17.

Replacing B with its relationship we arrive to the final form of the mechanical equation of the solid state (MESS) given by eq. 4.18. At higher strain rates the trend apparently remains linear, but the slope starts to reverse it trend that becomes decreasing with $1/T$. A new equation of the solid state is derived for the higher strain rate behavior. Several considerations can be done. First of all, in the low strain rate range, temperature has a direct effect on strain rate response, making it become less and less effective as T is increased. Temperature is *washing out* the dynamic effect. In the higher strain rate range, the opposite is observed, with $\dot{\varepsilon}$ that *washes out* the temperature effect.

The change of behavior at higher strain rates can be ascribed to a new deformation mechanism, which is no longer based on dislocation motion, but rather on twinning. Twinning, in fact, prevails over dislocation movements as the strain rate $\dot{\varepsilon}$ increases or the temperature decreases. If the hypothesis on the deformation mechanism change is correct, then the trend observed in the lower part of the $\ln(\sigma_y)$ versus $1/T$ diagram (i.e., low strain rates) on steels shall disappear on HPC metals, since twinning is the dominant mechanism in HCP metals. For this reason, a titanium alloy has been considered. The study on titanium has confirmed the prediction. In fact, titanium is showing already at low and even very low strain rates the trend observed on steel only at very high strain rates. Moreover, the linear response to changing temperature disappears, yet all the curves obtained at different strain rates seems to converge towards a common upper point, as in steel. At variance with steel, in the higher temperature range they tend to merge at zero stress, indicating that titanium shall not present an athermal component of the yield strength. All these findings suggest that also for steel and all other metals the curves representing the trend of the yield strength as a function of temperature and strain rate shall have a common upper and lower point, as shown schematically in figure 4.8.5. If this is the case, then eq. 4.22 and 4.27 are still valid, but will describe the material behavior only in the domain represented by the solid lines in fig. 4.8.5, respectively. In other words, at very high strain rates and very low temperature, steel shall behave like titanium, though with different slopes, losing the linear trend characteristic of the intermediate range of both temperature and strain rate. These very important findings require further investigation on different materials, in particular those having a FCC lattice, since they represent a completely new class of materials. If the findings are confirmed, then a unified MESS can be derived for all kind of materials predicting the yield strength at any temperature and strain rate.

REFERENCES

- Bonora N., Gentile, D. e Newaz, G., "Misure di Danno Duttile Su Acciaio A533b In Differenti Regimi Di Triassialità", Atti del XIV Convegno Nazionale Gruppo Italiano Frattura – IGF14, Maggio 27-28, 1998 Trento, pp. 283-290
- Bonora, N. and Newaz, M.G., (1998) "Low Cycle Fatigue Life Estimation for Ductile Metals Using a Non-Linear Continuum Damage Mechanics Model", Int. J. Solid and Structures, **35**, pp. 1881-1894.
- Bonora, N., (1997) "A Non-Linear CDM Model for Ductile Failure", Engineering Fracture Mechanics, **58**, pp. 11-28.
- Bonora, N., (1998) "On the Effect of Triaxial State of Stress on Ductility Using Nonlinear CDM Model", Int. Journal. of Fracture, **88**, pp. 359-371.
- Bonora, N., (1999), "Ductile Damage Parameters Identification And Measuremen", submitted for publication in Int. of Strain Analysis.
- Bonora, N., Cavallini, M., Iacovello, F. and Marchetti, M., (1994), "Crack Initiation in Al-Li Alloy Using Continuum Damage Mechanics", in Localized Damage III Computer-Aided Assessment and Control, Eds. M.H. Aliabadi, A. Carpinteri, S. Kalisky and D.J. Cartwright, Computational Mechanics Publication, Southampton Boston, pp. 657-665.
- Campbell J.D., "Yield Delay Time of Mild Steel", Trans. ASM, **51**, p. 659, 1959
- Campbell J.D., "The Dynamic Yielding of Mild Steel", Acta Metall., **1**, p. 706, 1953
- Chandrakanth, S., and Pandey, P.C., (1993), "A New Ductile Damage Evolution Model", Int. J. of Fracture, **60**, R73-R76.
- Conrad H., "On the Mechanism of Yielding and Flow in Iron", Jour. Iron Steel Inst., **198**, p. 364, 1961
- Conrad H., Hayes W., "Correlation of the Thermal Component of the Yield Stress of the BCC Metals", Aerosp. Corp., 1962
- Conrad H., Wiedersich H., "Activation Energy for Deformation of Metals at Low Temperatures", Acta Metall., **8**, p. 128, 1960
- Cottrell A.H., "Effects of Solute Atoms on the Behaviour of Dislocations", Ph. Soc., p. 30, 1948
- Cottrell A.H., "Deformation of Solids at High rates of Strain", Conf. on Prop. of Mat. at High Rates of Strain, pp. 1-12, 1957
- Cottrell A.H., "Dislocations and Plastic Flow in Crystals", Oxford, 1953
- Cottrell A.H., Bilby B.A., "Dislocation Theory of Yielding and Strain Aging of Iron", Ph. Soc., **62**, p. 49, 1949
- Cottrell A.H., Theory of Brittle Fracture in Steels and Similar Metals", Trans. AIME, **212**, pp. 192-203, 1958
- Follansbee P.S., and Kocks U.F., Acta Metallurgica, Vol. 36, p. 81, 1988

Follansbee P.S., in Metallurgical Applications of Shock-Waves and High Strain Rate Phenomena, eds. L.E. Murr, K.P. Staudhammer, and M.A. Meyers, Dekker, New York, p.451, 1986

Gurson, A.L., (1977), "Continuum Theory of Ductile Rupture by Void Nucleation and Growth: Part I- Yield Criteria and Flow Rules for Porous Ductile Media", J. Engn. Mat. Tech., **99**, pp. 2-15

Hancock, J.W. and Meckenzie, A.C., "On the mechanisms of ductile failure in high strength steels subjected to multi-axial stress-states", J. Mech. Phys. Solids, 1976, **24**, pp. 147-169.

Hoge K.G., and Mukherjee A.K., Jou. Mater. Sci., Vol. 12, p. 1666, 1977

Hollomon J. H., "The Mechanical Equation of State", Trans. AIME, 171, pp. 535-545, 1947

Johnson G.R. and Cook W.H., Proc. 7th Inter. Symp. Ballistic, Am. Def. Prep. Org. (ADPA), Netherlands, 1983

Johnson G.R., Hoegfeldt J.M., Lindholm U.S., and Nagy A., ASME Jour. Eng. Mater. Tech., Vol. 105, p. 42, 1983

Kachanov, L.M., (1986), Introduction to continuum damage mechanics, 1986, Martinus,Nijhoff Publisher, Boston- Dordrecht, 90-247-3319-7

Kanninen M. F. et al., NUREG CR/4219, Vol. 4, No. 2, 1987

Klopp R.W., Clifton R.J., and Shawki T.G., Mech. Mater. , Vol 4, p. 633, 1985

Le Roy, G., Embury, J.D., Edward, G. and Ashby, M.F., (1981), "A Model of Ductile Fracture Based on the Nucleation and Growth of Voids", Acta Metallurgica, Vol. **29**, pp. 1509-1522.

Lemaitre J.,(1992), A course in damage mechanics, Springer Verlag, New York, pp. 44-46.

Lemaitre, J.,(1985), A continuous damage mechanics model for ductile fracture, J. of Engng. Mat. and Tech., **107**, pp. 83-89

Manjoine M.J., " Influence of Rate of Strain and Temperature on Yield Stress of Mild Steels", Jour. Appl. Mech., 11, 4, A211-218, 1984

McClintock, F.A., (1968),"A criterion for ductile fracture by the growth of holes", J. Appl. Mech., **35**, pp. 363-371

Milella P.P., "Effetto della Temperatura e del Rateo di Applicazione della Deformazione sulla Tensione di Snervamento dei Metalli a Struttura CCC", In Italian, Italian Group of Fracture, 13th Symposium, Cassino, pp.34-43, 1997.

Milella P.P., "Temperature and Strain Rate Dependence of Mechanical Behavior of Body-Centered Cubic Structure Materials", Paper presented at TMS Fall Meeting '98, Chicago, Illinois, 11-15 October 1998, to be published.

Milella P.P., "Temperature and Strain Rate Dependence of Mechanical Behavior of Body-Centered Cubic Structure Materials: further Developments", Invited Lecturer, Wayne State University, Detroit, Michigan, March 5, 1999.

- Nemat-Nasser S., and Li Y., *Acta Met. Mater.*, Vol. 46, No. 2, p. 565, 1998a
- Nemat-Nasser S., and Obata M., *Proc. Royal Society of London*, Vol. A407, p. 343, 1986
- Nemat-Nasser S., Okinaka T., and Ni L., *J. Mech. Solids*, Vol. 46, No 6, p. 1038, 1998b
- Orowan E., "Dislocations and Mechanical Properties", *Disl. in Metals*, AIME, 1954
- Pardoën, T., Delanny, F. and Doghri, I., (1988), "On the Use of the Lemaitre and Chaboche for the Prediction of Ductile Fracture by Void Coalescence", *Int. J. Fract.*, **88**, L71-L76
- Petch N.J., "The Cleavage Strength of Polycrystals", *Jour. Iron Steel Inst.*, 174, p.25, 1953
- Petch N.J., "The Fracture of Metals", *Progr. in Metal Phys.*, 5, p.1, 1964
- Petch N.J., Helsop J., "The Stress to move a Free Dislocation in Alpha Iron", *Phil. Magaz.*, 47, p.886, 1956
- Ping, Wang-Ze, (1994), Void growth and compaction relations for ductile porous materials under intense dynamic general loading conditions, *International Journal of Solids and Structures*, 31, no. 15, pp. 2139-2150.
- Rice, J.R. and Tracy, D.M., (1969), "On ductile enlargement of voids in triaxial stress fields", *J. Mech. Phys. Solids*, **17**, 1969, pp. 210-217
- Rice, J.R. and Tracy, D.M., On ductile enlargement of voids in triaxial stress fields, *J. Mech. Phys. Solids*, **17**, 1969, pp. 210-217
- Seeger A., "The Generation of Lattice Defects by Moving Dislocations and Its Applications to Temperature Dependence of the Flow Stress in FCC Crystals", *Phil. Magaz.*, 46, p. 1194, 1955
- Seeger A., "The Temperature Dependence of the Critical Shear Stress and of Work Hardening of Metal Crystals", *Phil. Magaz.*, 45, p. 771, 1954
- Tai, H.W. and Yang, B.X., (1986), "A new microvoid-damage model for ductile fracture", *Engng. Frac. Mech.*, **25**, n° 3, pp. 377-384
- Tai, H.W., (1990), "Plastic damage and ductile fracture in mild steels", *Engng. Frac. Mech.*, **36**, n° 4, pp. 853-880
- Wert C.A., *Trans. AIME*, 188, p.1242, 1950
- Yokobori T., "The Cottrell Bilby Theory of Yielding of Iron", *Ph. Rev.*, **88**, p. 1423, 1953
- Zener C., Hollomon J.H., "Effect of Strain Rate upon Plastic Flow", *Jou. Appl. Ph.*, 15, 22-32, 1944.
- Zerilli F. J., Armstrong R.W., *Acta Met. Mat.*, Vol. 40, p. 1803, 1992
- Zerilli F. J., Armstrong R.W., *Jour. Appl. Phys.*, Vol. 61, p. 1816, 1987
- Zerilli F. J., Armstrong R.W., *Jour. Appl. Phys.*, Vol. 68, p. 1580, 1990